

Investigation of 2D Photonic Crystals and Their Applications on Terahertz Quantum Cascade Lasers, Optical Trapping and Sensing

THÈSE N° 5745 (2013)

PRÉSENTÉE LE 1^{ER} MAI 2013

À LA FACULTÉ DES SCIENCES DE BASE
LABORATOIRE D'OPTOÉLECTRONIQUE QUANTIQUE
PROGRAMME DOCTORAL EN PHOTONIQUE

ÉCOLE POLYTECHNIQUE FÉDÉRALE DE LAUSANNE

POUR L'OBTENTION DU GRADE DE DOCTEUR ÈS SCIENCES

PAR

Zhaolu DIAO

acceptée sur proposition du jury:

Prof. N. Grandjean, président du jury
Prof. R. Houdré, directeur de thèse
Prof. J. Faist, rapporteur
Prof. N. Le Thomas, rapporteur
Prof. Ph. Renaud, rapporteur



ÉCOLE POLYTECHNIQUE
FÉDÉRALE DE LAUSANNE

Suisse
2013

理想不老 ——— For my four years of life in Switzerland

Contents

Abstract	III
Résumé	V
1 Basics of photonic crystals	1
1.1 EM wave propagation in dielectric medium · · · · ·	1
1.2 Scaling properties of the Maxwell equations · · · · ·	4
1.3 EM wave confinement in dielectric medium · · · · ·	6
1.4 Photonic crystals · · · · ·	9
1.4.1 One-dimensional Photonic crystals · · · · ·	10
1.4.2 Two-dimensional Photonic crystals · · · · ·	11
1.4.3 Three-dimensional Photonic crystals · · · · ·	14
1.5 Numerical modeling methods · · · · ·	17
2 Fabrication techniques of photonic crystal devices	19
2.1 Si based photonic crystal devices fabrication procedures · · · · ·	19
2.1.1 Electron-beam Lithography · · · · ·	22
2.1.2 Etching · · · · ·	24
2.1.3 Scanning-electron microscope · · · · ·	27
2.1.4 Atomic force microscope · · · · ·	29
2.2 GaAs/AlGaAs based photonic crystal devices fabrication procedures · · · · ·	30
2.2.1 Plasma Enhanced Chemical Vapor Deposition (PECVD) · · · · ·	33
2.2.2 Reactive Ion Etching (RIE) · · · · ·	34
2.2.3 BCB planarization · · · · ·	35
2.2.4 Ebeam evaporator · · · · ·	37
2.3 Special case and summary · · · · ·	38
3 Coupling light into photonic crystal device	43
3.1 Between the fiber and the facet · · · · ·	43
3.1.1 SiN anti-reflection coating · · · · ·	45
3.1.2 TiO ₂ anti-reflection coating · · · · ·	48
3.1.3 SU-8 anti-reflection coupler · · · · ·	49
3.2 Between waveguides and photonic crystal structures · · · · ·	54
3.3 Inside photonic crystal structures · · · · ·	56

4 Applications in refractive index sensing	61
4.1 Applications of photonic crystals in refractive index sensing	62
4.2 Air slot waveguide and air slot cavity	63
4.3 Highly sensitive gas detection with air-slot photonic crystal nanocavity	65
5 Applications in optical trapping and back action	69
5.1 Introduction to optical trapping	71
5.2 Recent results in this field	74
5.3 Hollow photonic crystal cavities	76
5.4 Experimental set-up	78
5.5 Microfluidic cell	78
5.6 Single particle trapping and back action	81
6 Applications in THz photonic crystal lasers	87
6.1 Introduction to the THz frequency range	89
6.2 Quantum cascade laser	92
6.2.1 Quantum cascade laser	92
6.2.2 The THz QCL active region design	94
6.2.3 The waveguides	96
6.3 Fabry-Perot (FP) laser and Distributed feedback (DFB) laser	97
6.4 Photonic crystal THz lasers	101
6.5 Continuous-wave vertically emitting THz laser	105
Conclusions and perspectives	117
References	119
Publications	129

Abstract

Two dimensional photonic crystals (PhC) consist of spatially periodic dielectric medium. They allow optical control and manipulation of light propagation. Photonic crystals with photonic band gaps can be designed and constructed, preventing light from propagating in certain directions with specified frequencies. Within the photonic band gap, defect modes can be introduced in a large variety of designs, opening the way to a wealth of applications from sensing to laser. Alternatively, near a band edge, an ideal band evolves toward a singular point and the group velocity (v_g) of the corresponding waves is slowing down to a complete stop. The propagating modes have low v_g and high photonic density of states. These regions exhibiting slow light are presently the object of an intense activity with applications ranging from bandedge laser to data buffering and sensing.

Regarding the device fabrication technology, the objectives of this thesis are sorted into two topics. One topic is terahertz (THz) PhC quantum cascade (QC) laser light sources, which employ standard photolithography and dry etching. A robust surface emitting continuous-wave terahertz QC laser is realized by a second order Bragg grating extractor and a two-dimensional PhC structure. The goal is to improve the performance of PhC QCLs with single mode operation, reduced current threshold density (J_{th}), high emitting power and operating temperature.

The second topic is the design, fabrication and characterization of advanced photonic devices working at near-infrared wavelength for sensing and optical trapping applications. Benefiting from a two dimensional photonic band gap, the high quality factor (Q factor) cavity modes with small mode volumes are suitable for integration in an optical chip. A new type of silicon air-slot photonic crystal cavity was developed for optical refractive index sensing. Due to the strong overlap of the cavity mode with the detection volume, an impressive experimental sensitivity of 590 nm per refractive index unit (RIU) and a detection limit below 1×10^{-5} RIU were achieved.

Two-dimensional (2D) photonic crystal hollow cavities are used for optical trapping. Due to the large overlap of the particle with the optical mode combined with the subwavelength mode volume and large quality factors, self-induced trapping along with the back-action between a resonant optical field and a 500 nm single nanoparticle is achieved with sub-100 μ W trapping power.

Keywords:

Photonic crystals, slow light, gain enhancement, Terahertz, continuous wave, surface emission, hollow cavity, refractive index sensing, optical trapping, back action, quantum cascade laser, silicon on insulator, electron beam lithography.

Résumé

Les cristaux photoniques à deux dimensions sont des milieux diélectriques périodiques qui permettent le control optique et la manipulation des propriétés liées à la propagation de la lumière. Des cristaux photoniques peuvent être conçus et fabriqués de manière à créer une bande interdite photonique qui empêche la propagation des ondes lumineuses dans certaines directions sur une bande de fréquence bien précise. Il existe un large éventail de configurations permettant d'introduire des modes de défaut au cœur de la bande interdite. Ces derniers peuvent ensuite être utilisés pour de multiples applications allant de la détection à la réalisation de lasers. Un autre aspect très intéressant intervient au bord de la bande interdite. Là, une bande idéale évolue vers un point singulier où la vitesse de groupe (v_g) de l'onde correspondante ralenti jusqu'à atteindre zéro. Aux abords de cette région, les modes propagatifs ont une faible vitesse de groupe et une large densité d'états. Les régions dites « de lumière lente » sont actuellement l'objet d'une forte activité dont les applications s'étendent elles aussi de la détection aux lasers de bord de bande, en passant par le routage de données.

Concernant la technologie de fabrication des dispositifs, les objectifs de cette thèse sont séparés en deux parties. La première partie se consacre aux sources lasers terahertz (THz) à cascade quantique utilisant des cristaux photoniques et fait intervenir photolithographie standard et gravure sèche. Elle a mené à la réalisation d'un laser robuste, émettant en continu et par la surface à l'aide d'un extracteur à réseau de Bragg du deuxième ordre. L'objectif de ce travail est d'améliorer la performance des lasers à cascade quantique à cristaux photoniques fonctionnant en régime monomode, d'en réduire le seuil de densité de courant (J_{th}), d'attendre une forte puissance d'émission ainsi qu'une haute température de fonctionnement.

La deuxième partie se consacre à la fabrication et à la caractérisation de dispositifs photoniques avancés opérant dans le proche infra-rouge et destinés à la détection ainsi qu'au piégeage optique de nanoparticules. Les cavités à cristaux photoniques 2D bénéficient des effets de bande interdites pour atteindre de large facteurs de qualité et de petits volumes de mode tout en ayant la possibilité d'être intégré sur puce optique. Un nouveau type de cavité cristaux photonique à fente a été développée dans le but de détecter de très faibles variations d'indice de réfraction. Le large recouvrement du mode de cavité associé au fort facteur de qualité permet d'obtenir une sensibilité expérimentale de

590 nm par unité d'indice de réfraction (UIR) et une limite de détection inférieure à 1×10^{-5} UIR.

Des cavités creuses à cristaux photoniques sont également utilisées pour le piégeage optique. Le large recouvrement du mode de cavité, le volume de mode restreint et le facteur de qualité élevé permettent l'observation de piégeage auto induit ainsi que d'effets de rétroaction entre le champ confiné et une particule unique de 500 nm de diamètre même à des puissances inférieures à 100 μ W.

Mots-clés :

Cristaux photoniques, lumière lente, amélioration de gain, TeraHertz, émission continue, émission par la surface, cavité creuse, détection basée sur l'indice de réfraction, piégeage optique, rétroaction, laser à cascade quantique, silicium sur isolant, lithographie à faisceau d'électrons.

Chapter 1

Basics of photonic crystals

The interactions between electromagnetic radiation and matter govern most of the phenomena surrounding our everyday lives. For instance, the imaging process of the human eye is based on the principle of refraction where the electromagnetic wave is refracted and changes its direction of propagation when it impinges on an interface between two media with different indices. With the same underlying principle, modern microscopes and telescopes are built in order to observe the micro and macro worlds respectively. Another important phenomenon that we observe is reflection. The vast amount of data transported through worldwide networks is based on the reflection inside the optical fibers. It is possible to guide light in fibers owing to total internal reflection, which allows for a much higher bandwidth than metallic wires.

In this chapter, the basics of photonic crystals (PhCs) are discussed. Electromagnetic wave propagation in a dielectric medium is the starting point, which is governed by the Maxwell's equations. The scaling properties of the Maxwell equations are explained, which are important for photonic crystal (PhC) applications. In section 1.3, the physics of the electromagnetic wave confinement is detailed. PhC structures with one-dimensional, two-dimensional and three-dimensional periodicity are discussed in section 1.4. Different type of PhC defects, line type or point type, are introduced as well. In the last section, the methods of the modeling used in this thesis are briefly reviewed.

1.1 EM wave propagation in dielectric medium

All the applications of electromagnetic waves are based on the interaction between light and matter. The propagation of a electromagnetic wave is characterized by four Maxwell's equations (in SI unit):

$$\nabla \cdot D = \rho, \quad (1.1)$$

$$\nabla \cdot B = 0, \quad (1.2)$$

$$\nabla \times E = -\frac{\partial B}{\partial t}, \quad (1.3)$$

$$\nabla \times H = j + \frac{\partial D}{\partial t}, \quad (1.4)$$

Where,

E electric field, $[E] = \text{Vm}^{-1}$,

D electric displacement, $[D] = \text{Asm}^{-2}$,

B magnetic field, $[B] = \text{Vsm}^{-2}$,

H magnetic induction, $[H] = \text{Am}^{-1}$,

ρ free electric charge density, $[\rho] = \text{Asm}^{-3}$,

j free electric current density, $[j] = \text{Am}^{-2}$,

The relation between the electric field and the electric displacement as well as the relation between the magnetic field and the magnetic induction are given by the following equations:

$$D = \varepsilon_0 E + P, \quad (1.5)$$

$$B = \mu_0 (H + M), \quad (1.6)$$

Where,

$\varepsilon_0 = 8.8542 \cdot 10^{-12} \text{AsV}^{-1} \text{m}^{-1}$, absolute electric permittivity of vacuum,

$\mu_0 = 4\pi \cdot 10^{-7} \text{VsA}^{-1} \text{m}^{-1}$, absolute magnetic permeability of vacuum,

P electric polarization, $[P] = \text{Asm}^{-2}$,

M magnetization, $[M] = \text{Vsm}^{-2}$.

Here we consider linear optics and neglect the dependence of P on B . In the case of isotropic media, we are only interested in the local response of materials. With these simplifications we get the

$$P(r, \omega) = \varepsilon_0 \chi_e(\omega) E(r, \omega) \quad (1.7)$$

Similarly, one can get the following equation for the magnetization

$$M(r, \omega) = \chi_m(\omega) H(r, \omega) \quad (1.8)$$

Here, χ_e is the electric susceptibility, which characterizes the linear response of the material to an external electric field, χ_m is the magnetic susceptibility which corresponds to the linear response of the material to an external magnetic field. Then, equations (2.5) and (2.6) can be written as

$$D(r, \omega) = \varepsilon_0(1 + \chi_e(\omega))E(r, \omega) = \varepsilon_0\varepsilon(\omega)E(r, \omega), \quad (1.9)$$

$$B(r, \omega) = \mu_0(1 + \chi_m(\omega))H(r, \omega) = \mu_0\mu(\omega)H(r, \omega). \quad (1.10)$$

Where the electric permittivity $\varepsilon(\omega)$ and the magnetic permeability $\mu(\omega)$ appear.

In the case of a homogeneous medium, we can derive the wave equation for the electric field from Maxwell's equations

$$\left(\Delta - \varepsilon_0\mu_0 \frac{\partial^2}{\partial t^2} \mu\varepsilon\right) E = 0 \quad (1.11)$$

We take the ansatz $E(r, t) = E_0 \exp[i(kr - \omega t)] + \text{c.c.}$ and obtain:

$$k \cdot k = \mu\varepsilon\omega^2\mu_0\varepsilon_0 = n^2 \frac{\omega^2}{c_0^2} = n^2 k_0^2 \quad (1.12)$$

Where, $c_0^2 = \mu_0\varepsilon_0$, c_0 is the velocity of light in vacuum and k_0 is the vacuum wave vector, and

$$n(\omega)^2 = \mu(\omega)\varepsilon(\omega) \quad (1.13)$$

the square of the refractive index. For real valued refractive indices the phase velocity is

$$v_{ph} = \frac{c_0}{n} \quad (1.14)$$

In order to solve this eigenvalue problem, we need to make several assumptions. First, there are no free charges or currents inside the dielectric medium, we can set $\rho = j = 0$. Second, we assume the field strengths are small enough so that we are in the linear regime, so χ can be ignored. Third, we assume the material is bulky and isotropic, so that $E(r, \omega)$ and $D(r, \omega)$ are related by a scalar dielectric constant $\varepsilon(r, \omega)$. Fourth, we ignore any explicit frequency dependence of the dielectric constant at the frequency range of the physical system we are considering. Fifth, we focus only on lossless dielectric media, which means we can treat $\varepsilon(r)$ as purely real. The result is $D(r) = \varepsilon(r) E(r)$. For most dielectric materials of interest, the magnetic permeability is very close to 1 and we can set $B = \mu_0 H$ ¹.

With all of the assumptions mentioned above, the Maxwell equations (1.1) to (1.4) become

$$\nabla \cdot \varepsilon(r)E(r, t) = 0, \quad (1.15)$$

$$\nabla \cdot H(r, t) = 0, \quad (1.16)$$

$$\nabla \times E(r, t) + \frac{\partial H(r, t)}{\partial t} = 0, \quad (1.17)$$

$$\nabla \times H(r, t) - \epsilon(r) \frac{\partial E(r, t)}{\partial t} = 0. \quad (1.18)$$

In the Maxwell equations, the complex time and space functions of E and H can be expressed as

$$H(r, t) = H(r) e^{i\omega t}, \quad (1.19)$$

$$E(r, t) = E(r) e^{i\omega t}, \quad (1.20)$$

If we insert equations (1.19) and (1.20) into (1.15) and (1.16), the following conditions are achieved

$$\nabla \cdot H(r) = \nabla \cdot D(r) = 0, \quad (1.21)$$

These conditions have a physical meaning. There is no point source or form of displacement and magnetic field in the medium. The two curl equations of electric field (1.17) and magnetic field (1.18):

$$\nabla \times E(r) + \frac{i\omega}{c} H(r) = 0, \quad (1.22)$$

$$\nabla \times H(r) - \frac{i\omega}{c} \epsilon(r) E(r) = 0, \quad (1.23)$$

We can easily eliminate $E(r)$ and have a equation only with $H(r)$

$$\nabla \times \left(\frac{1}{\epsilon(r)} \nabla \times H(r) \right) = \left(\frac{\omega}{c} \right)^2 H(r), \quad (1.24)$$

This is so called master equation of $H(r)$. We can have corresponding master equation of $E(r)$ or express it with $H(r)$

$$E(r) = \left(\frac{-ic}{\omega \epsilon(r)} \right) \nabla \times H(r), \quad (1.25)$$

By this means, with a well-defined dielectric constant distribution $\epsilon(r)$, we can solve the master equation to find the $H(r)$ and $E(r)$ for a given frequency. From this starting point, we can reach more complicated systems.

1.2 Scaling properties of the Maxwell equations

The scaling property is a very powerful feature of electromagnetism in dielectric media. There is no fundamental length scale in the master equation. Not like in atomic physics where the fundamental length scale is the Bohr radius.

Based on the discussion in previous section, if we have an electromagnetic eigenmode $H(r)$ for frequency ω in a dielectric distribution $\epsilon(r)$, we will have the master equation of $H(r)$:

$$\nabla \times \left(\frac{1}{\epsilon(r)} \nabla \times H(r) \right) = \left(\frac{\omega}{c} \right)^2 H(r), \quad (1.26)$$

Next, if one is interested in the harmonic modes in a distribution of dielectric $\epsilon'(r)$ which is simply a compressed or expanded version of $\epsilon(r)$: $\epsilon'(r) = \epsilon(r/a)$ for some scale parameter a . Therefore, with the following changes of variables in (1.26), $r' = a*r$ and $\nabla' = \nabla/a$,

$$a \nabla' \times \left(\frac{1}{\epsilon(r'/a)} \nabla' \times H(r'/a) \right) = \left(\frac{\omega}{c} \right)^2 H(r'/a), \quad (1.27)$$

parameter a . Therefore, we have follow changes of variables in (1.26), $r' = a*r$ and

$$\nabla' \times \left(\frac{1}{\epsilon(r')} \nabla' \times H(r'/a) \right) = \left(\frac{\omega}{ca} \right)^2 H(r'/a), \quad (1.28)$$

This is nothing else but the master equation with the mode profile $H'(r') = H(r'/a)$, and frequency $\omega' = \omega/a$.

This scaling property of Maxwell equations is useful when investigate the optical properties of dielectric structures in different scales. The same design is valid for different wavelengths (microwave, infra-red, visible, UV). Due to the limitations of the current fabrication technology, as well as by knowing the scaling property of Maxwell equations, one can find the answer in centimeter or ever larger which is much easier to fabricate and still valid for micrometer or nanometer with the only difference of a scaling factor.

Another scaling law can be found on the dielectric constant. Just as there is no fundamental length scale, there is also no fundamental value of the dielectric constant. When we have $\epsilon'(r) = \epsilon(r)/a^2$

$$\nabla \times \left(\frac{1}{\epsilon'(r)} \nabla \times H(r) \right) = \left(\frac{a\omega}{c} \right)^2 H(r), \quad (1.29)$$

The result shows that field map and wavevector are unchanged. The physics is solely determined by the ratio of the dielectric constants $\epsilon'(r)/\epsilon(r)$.

1.3 EM wave confinement in dielectric medium

The master equation of $H(r)$ is an eigenvalue problem of a differential operator. Eigenvalues are $(\omega/c)^2 = k^2/\epsilon$, yielding the dispersion relation $\omega = ck/n_{\text{med}}$. The eigenvalues and eigenvectors give the propagation constant and the field distribution of the supported modes. If the spectrum is discrete for a given k , we can use integers for n , the band number. As the n value grows, the frequency of the mode also grows. As shown in Fig. 1.1, this plot of wave vector versus mode frequency is the band structure (or band diagram). The spectrum of states is continuous for all frequencies above the light line $\omega = ck$, which is a dashed red line in Fig. 1.1. The region of the band structure with $\omega > ck$ is called the light cone.

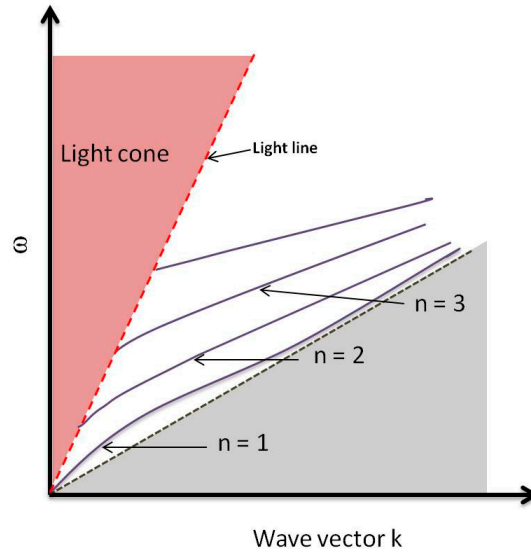


Figure 1.1: Dispersion diagram of TE polarized modes of a planar waveguide.

Index guiding An interesting situation arises when the light is incident from a medium with higher refractive index into a medium with lower refractive index $n_i > n_t$. As the angle of incidence θ_i increases, the angle of refraction θ_t increases accordingly as shown in Fig. 1.2 until reaching value $\pi/2$, i.e. the refracted wave propagates strictly parallel to the interface. Corresponding angle of incidence is called the critical angle $\theta_{ic} = \arcsin(n_t/n_i)$. For angles larger than θ_{ic} all light is reflected back into the medium of incidence, which is so called the total internal reflection (TIR). The electromagnetic field that penetrates into the medium 2 decays evanescently and does not carry any energy in the direction away from the interface, which is index guiding.

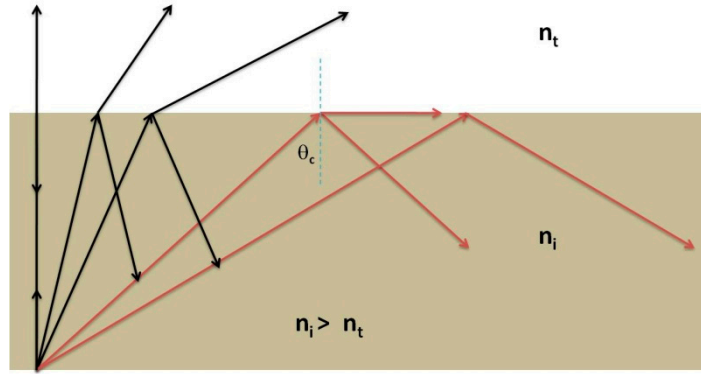


Figure 1.2: Schematic illustrations of total internal reflection.

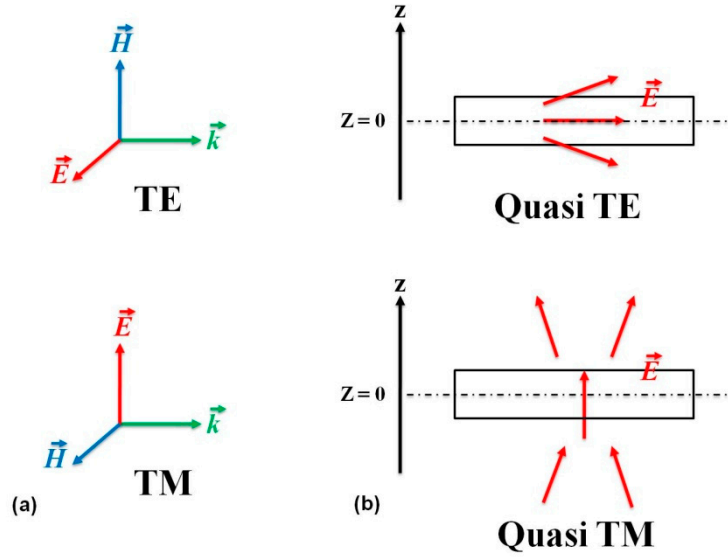


Fig. 1.3 The definitions of the TE and TM polarization (a). The polarization definition in ideal 2D system. (b). The polarization is defined with respect to the mirror plane at $z = 0$. The electrical field distribution may either be even (Quasi TE) or odd (Quasi TM).

In order to express the phase difference between the incident and the reflected light changing as a function of θ_i , the exact amplitude and phase relations upon reflection can be derived from the conditions of electric and magnetic field continuity at the interface (equation 1.30 to 1.33), which are the well-known Fresnel formulas:

$$r_{TE} = \frac{\tan(\theta_i - \theta_r)}{\tan(\theta_i + \theta_r)} = e^{i\varphi_{TE}} \quad (1.38)$$

$$r_{TM} = -\frac{\sin(\theta_i - \theta_r)}{\sin(\theta_i + \theta_r)} = e^{i\varphi_{TM}} \quad (1.39)$$

here r is the reflectivity coefficient and it depends on the polarization of the incident light. We define the polarization of the incident light in the following way: the TE polarization where the electric field is polarized parallel to the interface, i.e. no electric field in the

direction of propagation, and the TM polarization, where the magnetic field is parallel to the interface and has no component in the propagation direction. The schematic definitions of TE and TM polarization are showing in Fig. 1.3.

Total internal reflection effect is widely used for light guiding in waveguide. In this case, the core waveguide with higher refractive index is surrounded by another dielectric medium with a lower refractive index. Incident Light with an angle larger than the critical angle will be internally reflected at the interface for multiple times and propagates inside the waveguide without out-of-plane losses. However, in a real case, additional conditions need to be fulfilled. It is not true that any incident angle larger than θ_c is enough for light guiding. The original light and the light after two total internal reflections need to interfere with each other constructively. Otherwise, the light intensity decays along the propagation direction as a result of destructive interference. This is called the self consistency condition which can be expressed mathematically as following:

$$2d \frac{2\pi}{\lambda_0} \sin\theta^{TE/TM} - 2\varphi^{TE/TM} = 2\pi m, \quad m = 0, 1, 2 \dots N \quad (1.40)$$

On the left side of the equation 1.40, the first term is propagation and the second is the reflection. d and λ_0 is the waveguide thickness and the vacuum wavelength, respectively. The angles $\theta_m^{TE/TM}$ defines the wave vector components in the propagation direction, called the propagation constants $\beta_m^{TE/TM} = n_1 k_0 \cos\theta_m^{TE/TM}$. Note that the propagation constant differs for TE and TM modes due to the polarization dependence of the phase shift term φ .

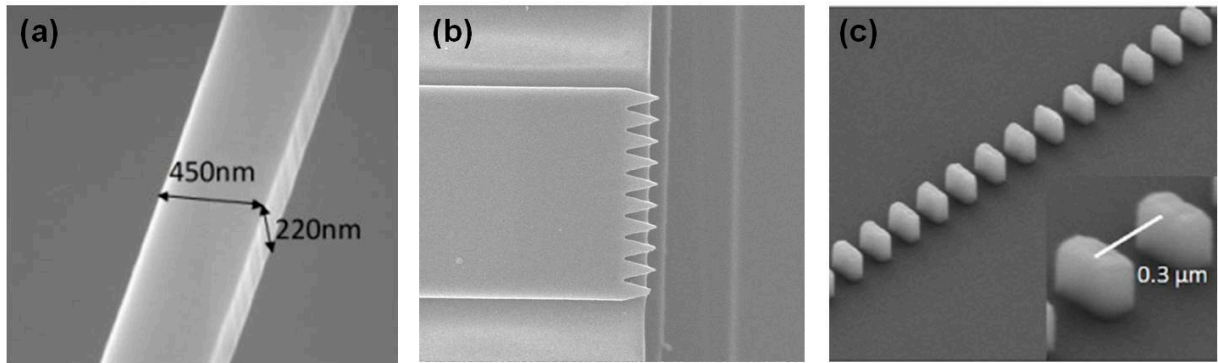


Fig. 1.4 Different designs of the two dimensional waveguides. ² (reprinted from ref. 2), (b) Rib waveguide with antireflection facet, (c) Sub-wavelength grating waveguide ³ (reprinted from ref. 3).

There are many different type of designs of the two dimensional waveguides. As showing in Fig. 1.4, Silicon on Insulator (SOI) waveguides based on a silicon strip on top of an oxide cladding are probably the most common, as their fabrication is compatible with the CMOS technology. At room temperature and telecom wavelengths of 1550 nm, the core and bottom cladding layers have refractive indices of 3.48 and 1.44 (silica oxide),

respectively. For typical cross-sectional dimensions of $450 \times 220 \text{ nm}^2$, the effective index of the fundamental TE mode is about 2.4, while the group index is approximately twice as large due to strong waveguide dispersion ⁴. Besides SOI waveguides, suspended strip waveguides supported by thin lateral pads or waveguides with both top and bottom oxide cladding can be used, similar design has already achieved in GaN platform ^{5, 6}. These configurations eliminate the polarization mixing and can reduce the propagation losses, however their processing requires an additional fabrication step.

1.4 Photonic crystals

In 1887, Lord Rayleigh studied the electromagnetic wave propagation in periodic media. His work is related to the peculiar reflective properties of a crystalline mineral with periodic planes. These structures are comparable with the current one-dimensional (1D) PhCs. Lord Rayleigh found out that there is a narrow band gap prohibiting light propagation through the planes. This band gap is angle-dependent, due to the different periodicities experienced by light propagating at non-normal incidences, producing iridescent reflected color patterns that vary sharply with angle. This effect is responsible for many other iridescent colors in nature, such as butterfly wings, sea mouse threads, natural opals and peacock feathers shown in Fig. 1.5. Their corresponding scanning electron microscope (SEM) images or optical microscope images indicate the periodic arrangement of the structures. All these beautiful colour examples have microscopic structures known as PhCs. Unlike pigments, which absorb or reflect certain frequencies of light as a result of their chemical composition, the way that PhCs reflect light is given by their physical structure.

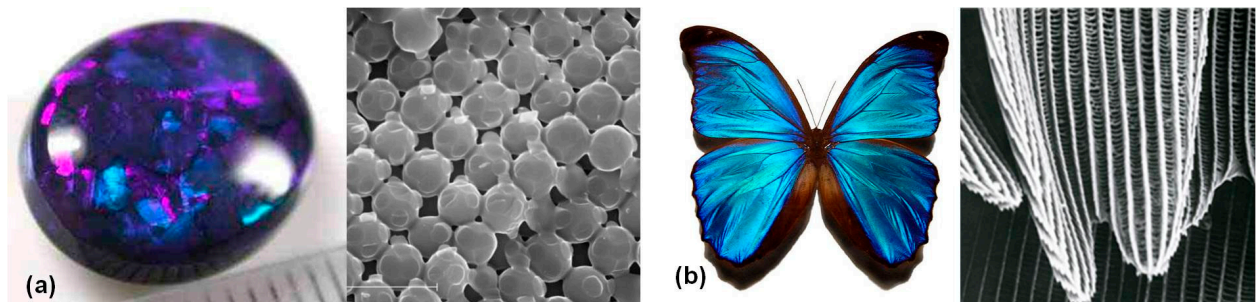


Fig. 1.5 (a), Black opal and its SEM image ^{7, 8} (reprinted from ref. 7 and 8). (b) Mopho Didus butterfly and its SEM image ^{9, 10} (reprinted from ref. 9 and 10).

In semiconductor physics, periodic arrangement of atoms in crystal lattices determines the periodic potential for the electrons and forms the band structure for electrons. This can be used to manipulate electrons in the crystals and achieve numerous applications for our daily life. PhC is an optical analog artificial structure of crystal structures and can manipulate photons. In PhC, photons experience the periodic potential caused by dielectric constant difference. This results in photonic band structure. PhCs were

originally proposed independently and simultaneously in 1987 by two researchers, in order to investigate two fundamental optical principles: the localization and trapping of light in a bulk material ¹¹ and the complete inhibition of spontaneous emission over a broad frequency range ¹². Sajeev John was investigating whether Anderson localization of electrons in a disordered solid can be extended to photons in a strongly scattering medium, and predicted that localized states of the electromagnetic field can be created in a periodic dielectric medium. At the same time, Eli Yablonovitch was trying to address the possibility of suppressing the unwanted spontaneous emission affecting the semiconductor lasers, and predicted that a 3D periodic dielectric can produce a forbidden gap in the electromagnetic spectrum. This generalization, which inspired the name “photonic crystal,” led to many subsequent developments ¹³⁻¹⁵ in the fabrication, theory, and applications.

1.4.1 One-dimensional Photonic crystals

Depending on their periodicity, PhCs can be defined as one-dimensional, two-dimensional and three-dimensional (1D, 2D, 3D), as illustrated in Fig 1.6. A full photonic band gap only can be realized in 3D PhCs for light propagating in all directions. 1D and 2D PhCs only have incomplete photonic band gaps, which restricts only a few directions of propagations. They are important to understand the fundamental optical properties of PhCs. Furthermore, they are much easier for fabrication and practical implementation for many applications.

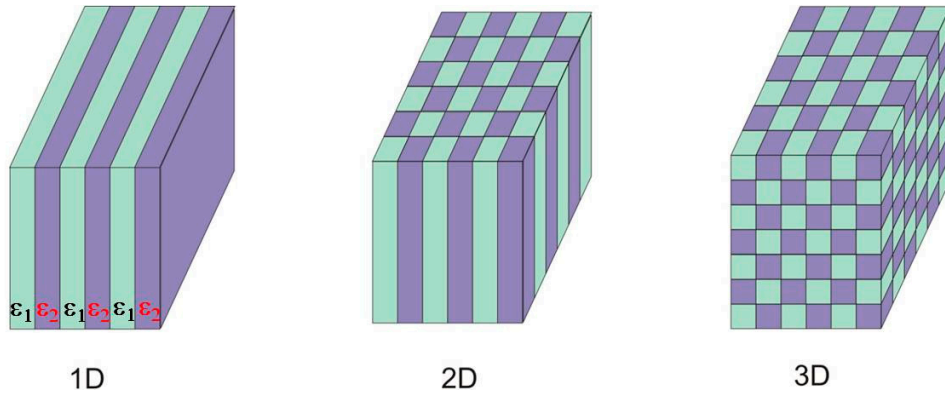


Figure 1.6: Schematic illustrations of PhCs periodic in one, two, and three dimensions.

In order to understand the origin of the photonic band gap throughout 1D, 2D and 3D PhCs, we can simply investigate the situation for 1D case. They all have the same physical basis. Let us consider a one-dimensional system with a uniform dielectric constant ($\Delta\epsilon = 0$), which has plane wave eigensolutions $\omega(k) = ck$, as shown in Fig. 1.7.a. This gives the usual unbounded dispersion relation. Based on Bloch theorem, the dispersion diagram is periodic. All dispersion properties of PhCs can be investigated inside the first Brillouin zone ($-\pi/a < k < \pi/a$, a is the lattice constant). In 1D PhC system with

$\varepsilon_1 < \varepsilon_2$, the forward ($k = \pi/a$) and backward ($k = -\pi/a$) propagation wave superpose with each other at the border of the first Brillouin zone. The coupling of the two counter-propagating waves results in splitting of the originally degenerate state into two states with frequency difference of $\Delta\omega$ (as show in Fig 1.7.b).

In Fig 1.7.b, the higher band state has electric field maxima in the low dielectric constant material. On the other hand, the lower band state has electric field maxima in the high dielectric constant material. For this reason, these bands are so called air band and dielectric band, respectively. This photonic band gap $\Delta\omega$ is related to the refractive index contrast. High refractive index contrast leads to large photonic band gap, low refractive index contrast leads to small photonic band gap

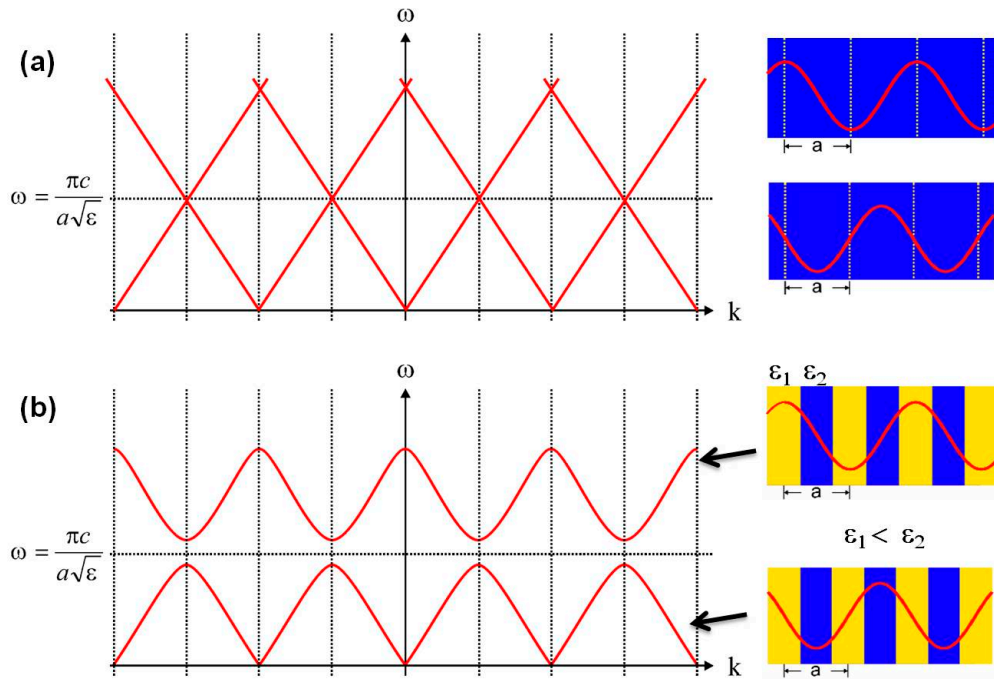


Figure 1.7: (a) Dispersion curve of uniform lattice with $\Delta\varepsilon = 0$. (b) Dispersion curve of 1D photonic crystal with $\varepsilon_1 < \varepsilon_2$.

1.4.2 Two-dimensional Photonic crystals

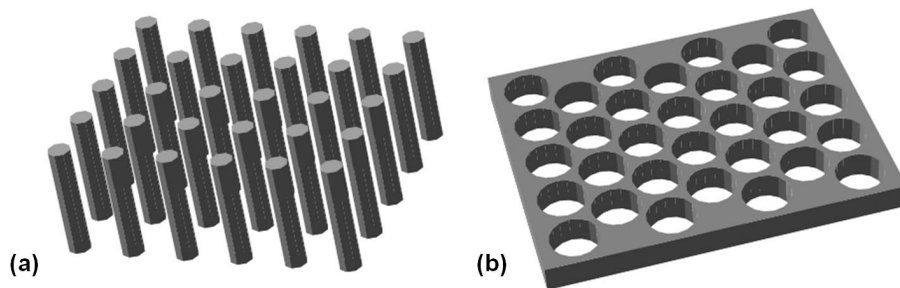


Figure 1.8: (a) High dielectric constant pillar in air structure. (b) Air hole in high dielectric constant slab structure.

By understanding the origin of the photonic band gap, one more dimension can be added. Ideal 2D PhC shows periodicity in two dimensions and infinitely long in the third one. In reality, we investigate 2D PhC with limited size in the third dimension (as shown in Fig 1.8). In this case, the light confinement for the third dimension is provided by planar waveguiding (see Section 1.3).

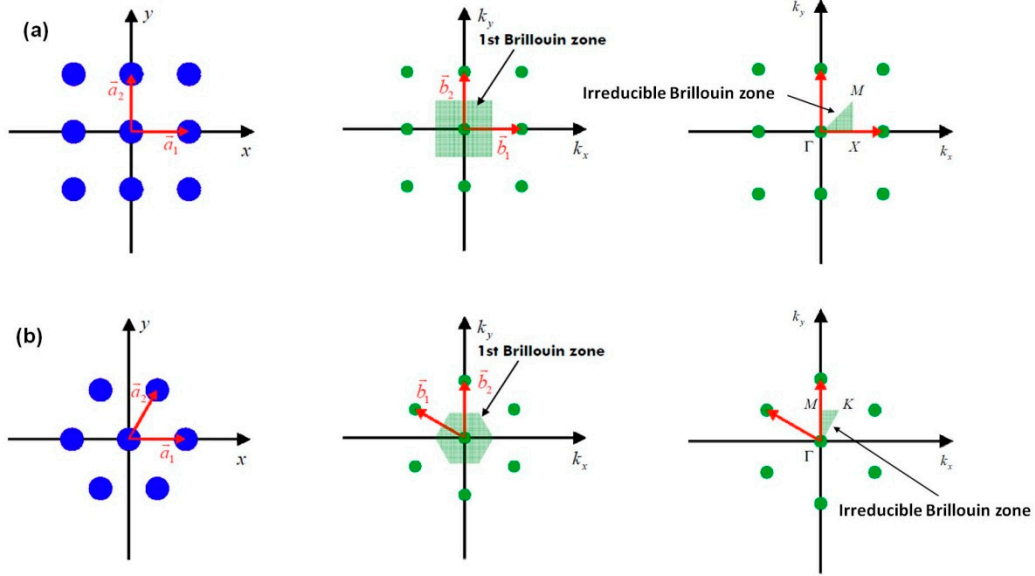


Figure 1.9: Lattice, reciprocal lattice and 1st Brillouin zone of the (a) square and (b) triangular PhC.

There are all kinds of periodicity in 2D PhCs. The most common are the square and triangular lattice (as shown in Fig 1.9). Each of them is defined by two lattice vector \mathbf{a}_1 and \mathbf{a}_2 . Each direct lattice is accompanied by a reciprocal lattice which is defined by two reciprocal lattice vector \mathbf{b}_1 and \mathbf{b}_2 . Direct and reciprocal lattice vectors are related by $\mathbf{a}_j \cdot \mathbf{b}_i = 2\pi\delta_{ij}$.

The dispersion of the 2D PhC is quite similar with the dispersion of the 1D PhC, but is more complex, because in this case the frequency is a function of the wavevector (\mathbf{k}) $\omega = \omega(\mathbf{k})$, instead of the scalar k as for 1D PhCs. For a given \mathbf{k} vector there are several possible values of frequencies: $\omega = \omega_n(\mathbf{k})$. These values define surfaces in the (ω, \mathbf{k}) space, called the photonic bands of the PhC. The examples of dispersions diagram for both pillar-type and hole-type 2D PhC are shown in the Fig. 1.10.

The bulk PhC dispersion curve for triangular lattice is calculated (both for filling factor of 40% and high/low index of 3.56/1). Hole-type structure has complete band gap (in red shadow) for TE polarization. Pillar type structures have a complete band gap (in blue shadow) for TM polarization. Such dispersion band structures are computed using a 2D Plane wave expansion (PWE) method that will be detailed later. As shown in the band

dispersion curve, the pillar type structure is best suited for TM light and the hole type structure is best suited for TE light.

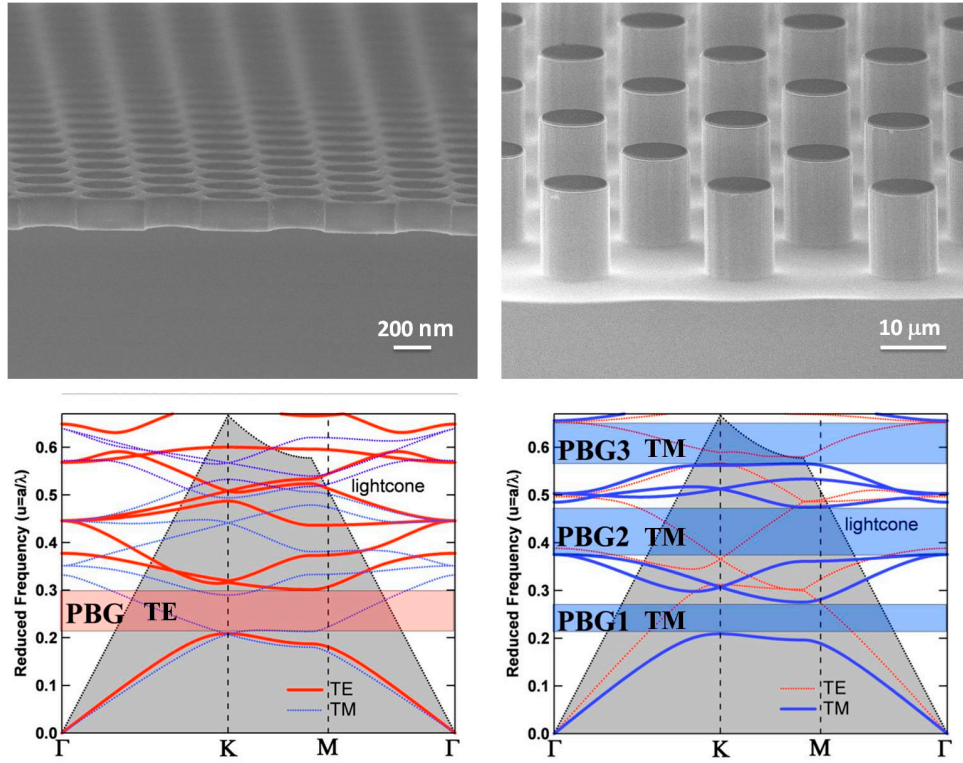


Figure 1.10: SEM images of hole-type (top left) and pillar type (top right) 2D PhCs. : Band dispersion curve of hole-type (bottom left) and pillar type (bottom right) 2D PhCs. Hole-type structure has complete band gap (in red shadow) for TE polarization. Pillar type structure has complete band gap (in blue shadow) for TM polarization.

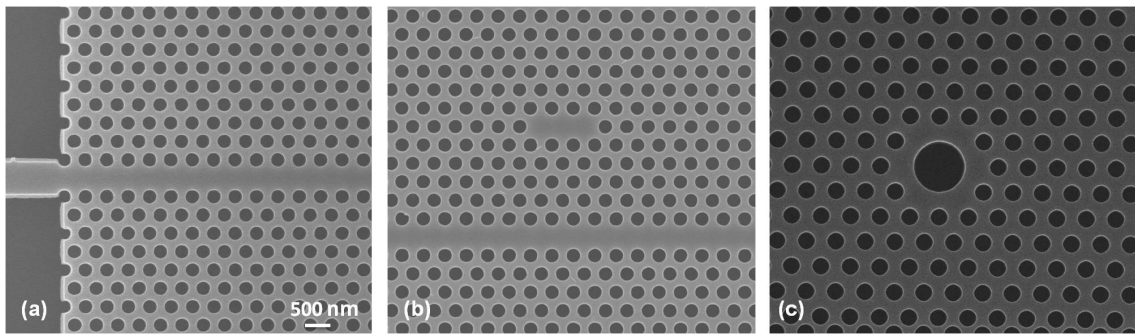


Figure 1.11: SEM images of typical defects in 2D PhCs. (a) W1 waveguide. (b) L3 cavity and W1 waveguide. (c) Big hole cavity.

Manipulating the light propagation in dielectric structures means two basic aspects: One is to prevent light propagation within selected frequency range; the other one is to allow light propagation within a selected frequency range. So far, we focus on the photonic band gap. This is just the first step and the second step is introducing defect modes into 2D

PhCs structures. By doing so, more interesting functions like PhC waveguiding, light localization, and light matter interaction enhancement can be finally achieved.

The defects can be divided into two groups: cavity and waveguide. PhC cavities are created by removing, adding or shifting the position of one or more lattice ‘atoms’ (holes or pillars). Cavity with one air hole missing is called H1 and with three holes missing in ΓK direction is called L3, and so on. With appropriate design, cavities can reach extremely high quality factors $Q \sim 10^6$ with ultra-small mode volumes, resulting in strong light matter interaction enhancement effect. PhC cavities find a vast number of applications in cavity quantum dot interaction, optical trapping and slow light enhancement. They also constitute a promising building block for optical (bio) sensors ¹⁶⁻¹⁸.

By removing one or n rows of air hole in ΓK direction from PhC lattice, W1 or W n waveguide is achieved. Such waveguides have in-plane confinement due to the photonic bandgap effect and the out-of-plane confinement due to index guiding. PhC W1 waveguides can guide light with propagation loss comparable to nanophotonic wire waveguides (5 dB/cm ^{19, 20}). In addition, they can realize sharp, virtually lossless bends and corners thus enable to control the direction of light at the wavelength scale. A lot of effort have been invested into optimization of such bends (changing the number, size or position of holes at the bends) to avoid spurious back-reflection loss within a reasonable operation bandwidth ^{21, 22}. W1 waveguides are also intensively studied as a possible candidate for slow light applications ²³, as they exhibit a region of flat dispersion in the proximity of the mode cutoff. Recently, an air slot was inserted in W1 waveguide, which is referred to as the W1 slot waveguide. It can provide for the enhancement and confinement of light in the low-index material ^{24, 25}.

1.4.3 Three-dimensional Photonic crystals

2D PhCs are quite useful, but the real world is three-dimensional. There is no photonic band gap in the out of plane direction. In this direction, 2D PhCs only have total internal reflection confinement, which is responsible for out of plane scattering losses and result in a relatively weak transmittance. Even in the case of in-plane propagation, 2D PhC requires a large aspect ratio (height/period) in order to meet experimental constraints. Strategies to overcome all these limitations are to introduce photonic band gap in the third dimension.

One of the first predictions of 3D photonic band gap was done in a face-centered-cubic structure with non-spherical atoms (as shown in Fig 1.12). This structure (called Yablonovite) can be fabricated by etching (or drilling) cylindrical holes in high-permittivity dielectric medium. The first sample was designed to work in microwave wavelength. With the help of ion beam etching method, holes with a radius of $0.234a$ results in a structure

with a complete photonic band gap of 19% (Fig 1.12) around a wavelength of 1.6 μm , illustrations of the ion beam etching method and the SEM image of the fabricated sample are shown in Fig 1.13.

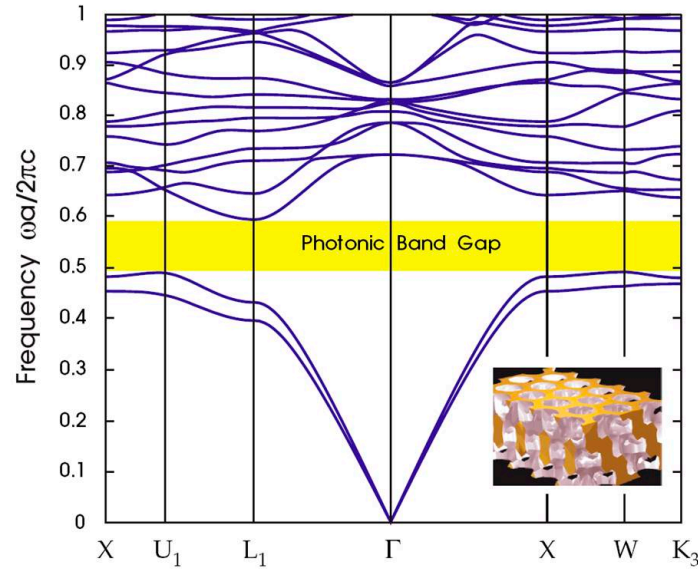


Figure 1.12: Photonic dispersion curve of Yablonovite. Inset is the schematic illustrations of Yablonovite and photonic band gap is indicated in yellow¹ (reprinted from ref. 1).

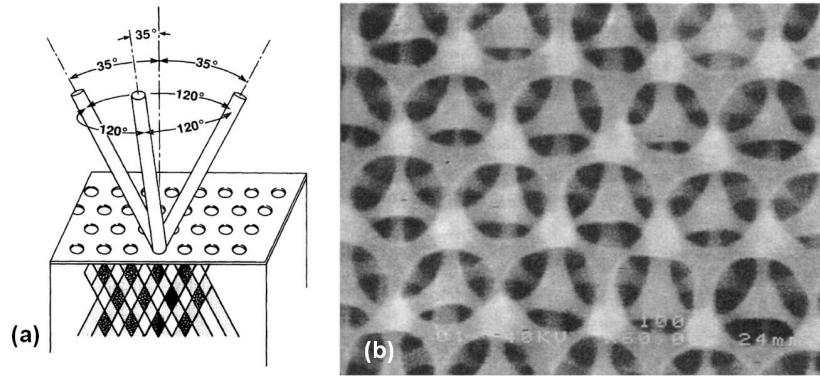


Figure 1.13: (a) Schematic illustrations 3D Yablonovite structure fabrication¹⁴ (reprinted from ref. 14). (b) SEM image of the fabricated Yablonovite structure by ions beam etching²⁶ (reprinted from ref. 26).

After the introduction of the Yablonovite structure, many different 3D PhC structures have been proposed. One group is the opal or the inverse-opal type (as shown in Fig 1.14). The opal structure is created with dielectric spheres (usually SiO_2) that are self-assembled. The inverse-opal is achieved by filling the opal structure with dielectric material and the removing the opal sphere during a subsequent etching step. The optical quality of these structures strongly depends on the homogeneity of the dielectric spheres. The photonic dispersion curve is very sensitive to any defects introduced in the fabrication steps.

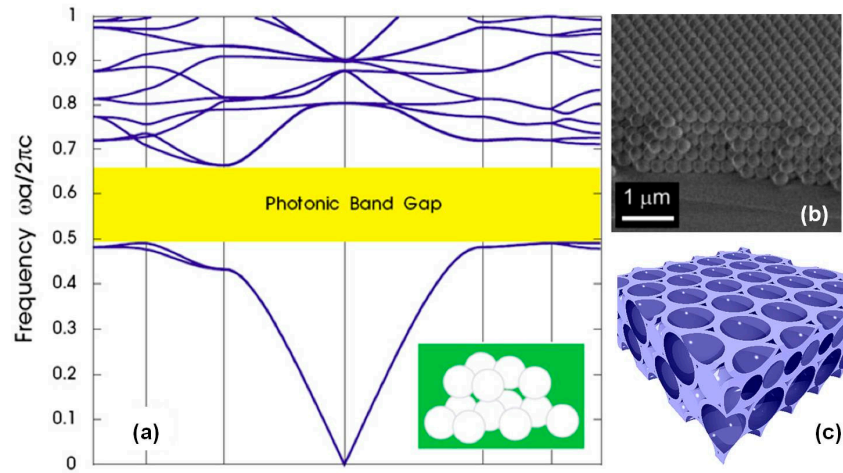


Figure 1.14: (a) Photonic dispersion curve of opal structure, photonic band gap is indicated in yellow ¹(reprinted from ref. 1). (b) SEM image of opal structure ²⁷ (reprinted from ref. 27). (c) Illustration of inverse-opal structure.

Another group of 3D PhCs are artificially fabricated structures. The woodpile structure is one of the highly investigated examples. The woodpile crystal is formed by a stack of dielectric 'logs' (normally rectangular) with alternating orthogonal orientations. It can be fabricated as a sequence of layers deposited and patterned by lithographic techniques developed for the semiconductor electronic industry. Recently, the invention and development of the direct laser writing method, which is a non-linear two-photon absorption process, gives access to the fabrication of more complicated structures in a single step in different photosensitive materials. These structures can then be replicated or inverted in silicon or other materials (As show in Fig 1.15 c).

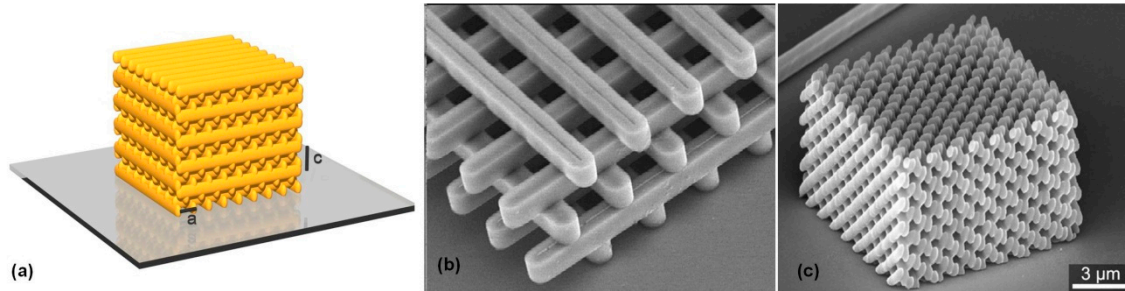


Figure 1.15: (a) Schematic illustration of a woodpile structure. (b) SEM image of a Si bar woodpile structure ²⁸ (reprinted from ref. 28). (c) SEM image of the standing for slanted pore structure fabricated by direct laser writing method ²⁹ (reprinted from ref. 29).

With 3D PhCs, we can achieve real complete photonic band gap and manipulate the propagation of the light in all directions. At the same time, it also has its own limitations. All the 3D PhC structures are difficult to fabricate even with the best technology available currently. Most of these fabrication processes are very costly, complicated and time-consuming. If one want to introduce some demanding defect states inside the photonic band gap, 3D PhCs are much more complex than 2D PhCs for the same reason. Hopefully,

progress of new upcoming technologies will make the situation better for the future, just like what has happened in most scientific fields in the past.

1.5 Numerical modeling methods

The PhC structures are designed with the help of numerical modelling techniques using any of the following methods: Plane-Wave Expansion (PWE), Finite Difference Time Domain (FDTD) method and Finite Element Method (FEM).

PWE can be used to calculate the dispersion band diagram. It solves Maxwell's equations by formulating an eigen-value problem out of it, and thus solves for the eigen-frequencies for each of the propagation directions. The advantage of this method is that it can be used for almost any PhC structure (complex structures require the use of the super-cell approach), it yields directly the dispersion diagram and it gives a fair insight into the physics of PhCs. All photonic band structure calculations presented in this work were performed using 2D PWE and Guided Wave Expansion (GWE) routines developed by D. Leuenberger³⁰ and V. Zabelin³¹.

FDTD is a versatile modelling technique used to calculate the electric field distribution by solving Maxwell's equations; it can be used to simulate 2D and 3D PhC structures for transmission, field distribution verses wavelength or Quality factor of a resonant cavity. However, it is a 'black box' method, which does not facilitate the physical understanding, it is extremely computer resource consuming and requires a right choice of initial and boundary conditions to excite all the desired Bloch modes and to avoid spurious reflections due to finite size of the calculation area.

FEM is a powerful tool for 2D and 3D simulation. It can find the eigenfrequency of the system by solving the partial differential equations (PDE) and integral equations. In addition, it can simulate transmission and reflection, and field distribution within a very short simulation time. All of the mentioned methods will be used for different purposes. The commercial FEM-based COMSOL simulation software was used to calculate the dispersion and electromagnetic distribution of optical defects and cavities, including their quality factors and optical losses.

Chapter 2

Fabrication techniques of photonic crystal devices

The focal contribution throughout my thesis is the fabrication of PhC devices with high quality optical performance. The smallest discrepancy in the sizes of (even as small as a few nanometers) the fabricated device can result in a noticeable effect on optical properties. In this context, it is highly important to reduce this discrepancy between the fabricated device and the original design as much as possible, or in other words, to control the fabrication induced disorder within acceptable levels. PhCs devices investigated in this thesis can be divided into two groups. One is silicon based passive PhC devices. The other one is GaAs/AlGaAs based active PhC devices. We detail the fabrication techniques in two groups. The devices are processed in CMI and ICMP clean rooms in EPFL. In the CMI clean rooms, we use a Vistec EBP5000 electron beam lithography (EBL) system, AMS200 DES inductively coupled plasma (ICP) dry etcher, Heidelberg DWL200 laser lithography system³², Bruker Atomic Force Microscope, Leybold optics LAB600H electron gun evaporator and Sopra GES 5E spectroscopic ellipsometer. In LOEQ clean rooms, we use Suss Microtech MJB3 UV400 mask aligner, Sentech ICP-RIE SI 500 RIE etcher, Oxford Plasmalab system 80 plus RIE Etcher, Plasmaline 415 Tegal, Ebeam 2000 electron beam evaporator, Oxford Plasmalab System 100 PECVD, SEM JEOL JSM-6701F, Tencor Alphastep IQ profilometer and JFP Model 100 wafer scribe. Most of the above mentioned equipments would be described separately with the main features concerning the fabrication procedures.

2.1 Si based photonic crystal devices fabrication procedures

In this thesis, positive resist method is used to fabricate silicon devices, the fabrication procedures are as following (as shown in Fig. 2.1):

Substrate Preparation: A diced SOI substrate (10×15 mm²) is cleaned by rinsing in Acetone and Isopropanol (IPA) for 5 minutes each and then cleaned in Acetone overnight.

Ultrasonic and pre-bake: The substrate is rinsed in an ultrasonic bath for 5 minutes at 45 kHz in Acetone. After rinsing in Acetone and IPA, the substrate is pre-baked at 110 °C for 3 minutes in order to release the water on the surface.

Ebeam resist spin coat: Positive resist (ZEP520A 1:1 with Anisole) is spin-coated onto the substrate surface for 30 seconds with 2000 rpm (thickness of 200 nm).

Hard Bake: The spin coated substrate is baked at 180 °C for 180 seconds.

Exposure: The resist is exposed by EBL.

Development: The sample is then developed in n-amyl-acetate 60 seconds. Afterwards, the sample is rinsed in 9:1 Methyl Isobutyl Ketone (MiBK):IPA for 30 second to stop the development process. At last, the sample is dried by N₂ gas.

Dry etching: The sample is etched by AMS200 ICP dry etching for 3 minutes 20 seconds (depending on the thickness of the nanostructures) with a gas mixture of SF₆ and C₄F₈.

Cleaning and photolithography resist spin coat: The primer and positive resist (Hexamethyldisilazane (HMDS) and AZ5214) are spin-coated onto the substrate surface for 10 and 30 seconds both with 5000 rpm, respectively. The sample is left in air for 5 minutes and soft baked at 90 °C for 5 minutes.

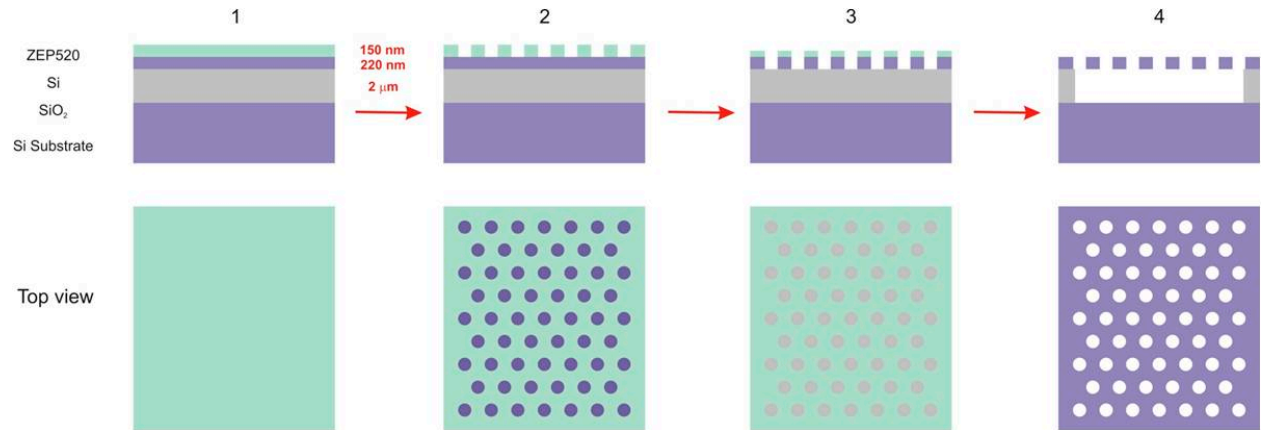


Figure 2.1 1: Sample preparation and spin-coating. 2: E-beam exposure and development. 3: Dry etching. 4: Membrane release in BHF.

Exposure: The wet etching window is exposed by Microtech MJB3 mask aligner for 4 seconds.

Development and hard bake: The sample is then developed in MF319 for 60 seconds. Afterwards, the sample is rinsed in water for 15 seconds to stop the development process. At last, the sample is dried by N₂ gas and baked at 115 °C for 15 minutes.

Facets protection: Wax is melted at 110 °C and swiped onto both facets to protect input and output waveguides during wet etching process.

Wet etching for membrane releasing: The sample is put in BHF for 30mins to selectively etch 2 μm SiO_2 layer.

Cleaning and drying: The wax and photolithography resist are removed in Acetone. The sample is then cleaned in acetone and IPA respectively. The sample is dried by IPA vapor at 90 °C for 3 minutes^{33, 34}.

The material system used to fabricate the silicon devices is Silicon-On-Insulator (SOI). This high quality wafer is purchased from SOITEC. The diameter of this wafer is 200 mm. There are 3 layers in this wafer. From the top to the bottom, they are: 220 nm silicon, 2 μm SiO_2 and 750 μm silicon substrate layer, respectively. The thickness tolerance of a 220nm silicon layer of an 8 inches SOI wafer is ± 2 nm (center part as shown in Fig. 2.2). The small variation of the silicon layer's thickness is important for well-controlled fabrication flows. The refractive index guiding planar waveguides are Air/Si/ SiO_2 and Air/Si/Air for SOI and Si membrane respectively. Depending on the designs, the full wafer is diced into 10×15 mm² or 25×30 mm² small pieces. It is possible to use pieces with the same thickness of silicon layers by using this thickness map (Fig. 2.2). In order to get better facet cleaving results, these small pieces are polished on their backside to reduce the thickness from 750 μm to 250 μm .

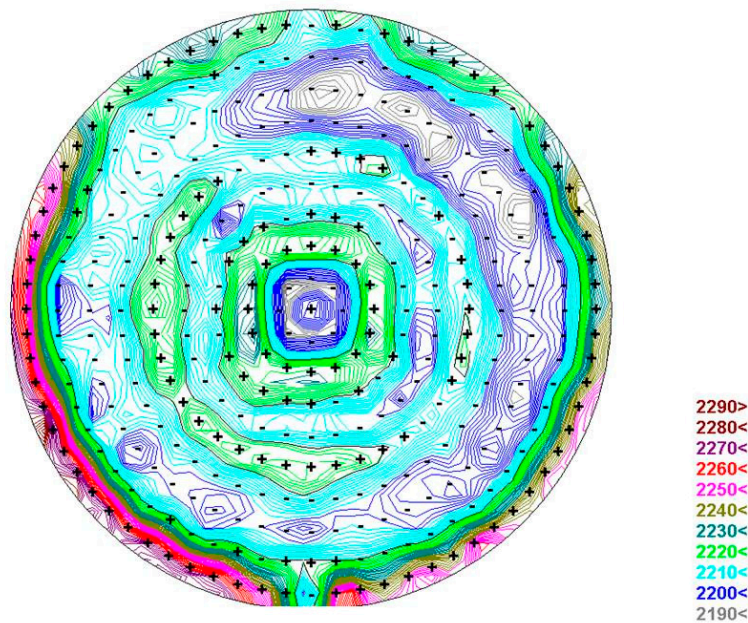


Figure 2.2: SOI wafer thickness mapping measured by SOPRA GES 5E Spectroscopic Ellipsometer. The thickness of the top silicon layer in an 8 inches wafer is displayed in different colors (the units are in angstrom)

Photoresists can be divided into two groups: positive and negative. In the case of the positive resists, the resist is exposed with the electron beam wherever the underlying

material has to be removed. In these resists, exposure to the electron beam or UV light changes the chemical structure of the resist so that it becomes more soluble in the developer. The exposed resist is then washed away by the developer solution, leaving windows of the bare underlying material (as shown in Fig. 2.3). The widely used positive photoresists are Polymethyl methacrylate (PMMA), AZ photoresist and ZEP520. ZEP520 is more sensitive to the e-beam and is better for fabricating smaller structures compared to the others. ZEP520 is used for e-beam photolithography in this thesis. AZ5214 is used in UV photolithography process. Negative resists behave in just the opposite manner. Exposure to the electron beam or UV light causes the negative resist to become polymerized, and harder to dissolve in the developer. Therefore, the negative resist remains on the surface wherever it is exposed, and the developer solution removes only the unexposed portions. The widely used negative photoresists are Hydrogen SilsesQuioxane (HSQ) and SU8. HSQ is a highly sensitive e-beam resist and is suitable for fabrication of nanostructures involving lift-off process. SU8 is less sensitive and is suitable for fabrication of micrometer-sized structures.

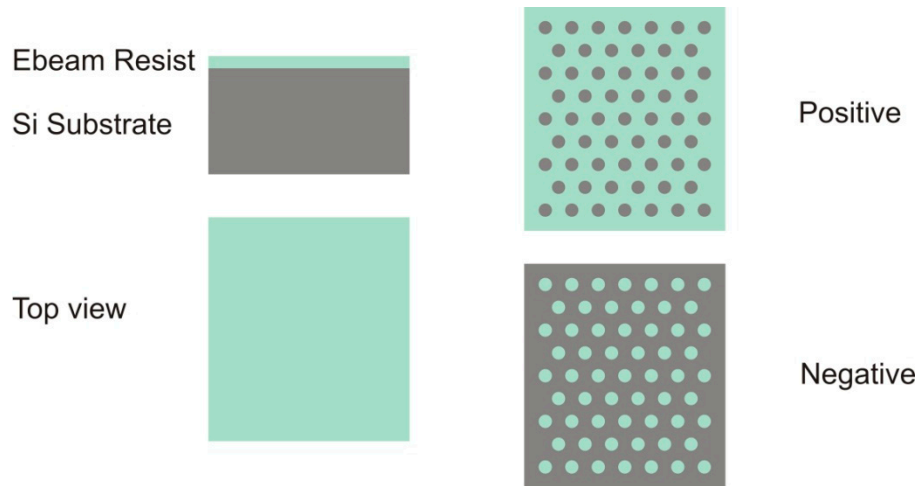


Figure 2.3 Positive and negative resist. Positive: after the development, the exposed part of resist goes away. Negative: after the development the exposed part of resist stays.

2.1.1 Electron-beam Lithography

Electron beam lithography (EBL) is a specialized technique used to fabricate the extremely fine patterns required by the modern electronics industry for integrated circuits (As shown in Fig. 2.4 the illustration of the setup). This is possible due to the very small spot size of the electrons, whereas the resolution in optical lithography is limited by the wavelength of light used for exposure. The electron beam has a wavelength so small that diffraction no longer defines the lithographic resolution.

This technique consists of scanning a beam of electrons across a surface covered with a sensitive resist film, thereby exposing the desired pattern. In order to transfer the photoresist pattern into a desired layer, lift-off or dry etching processes are used after the

EBL direct writing. In our work, nanostructures are obtained by e-beam lithography, which is followed by a dry etching process.

Additionally, an appropriate resist is required. This resist is chemically modified by the impinging electrons in a way that an appropriate solvent can etch away those regions which are either scanned by the electron beam (positive resist) or not scanned (negative resist). In the following section, the positive resist ZEP520A (A positive resist ZEP 520 is diluted with photoresist thinner Anisole at a volume ratio of 1:1.) is discussed, which is used for the lithography in the process of this thesis. A 200 nm thick photoresist is obtained at spin coating speed 2000 rpm for 30 s. The PhC structures in the ebeam resist films are transferred into the silicon layer by ICP dry etching process, which will be discussed later.

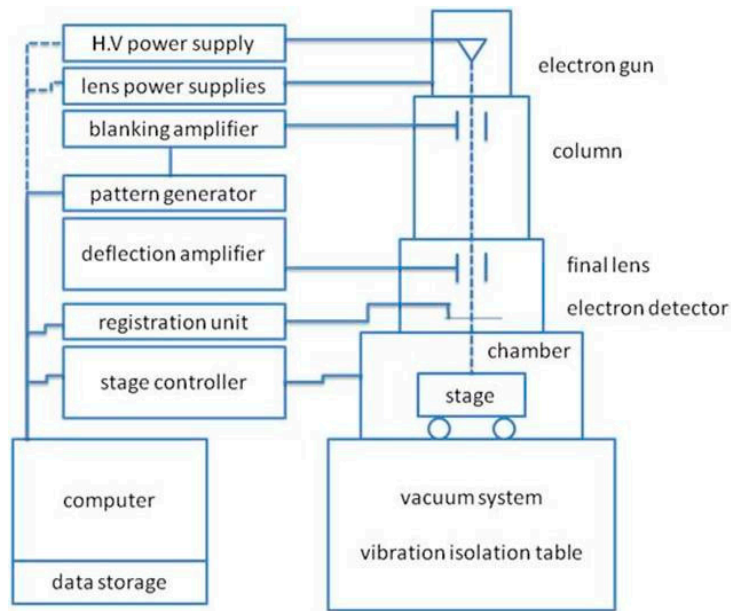


Figure 2.4 Schematic of electron beam lithography. The electron beam is generated from top and adjusted by lens before it impinges the sample in the chamber.

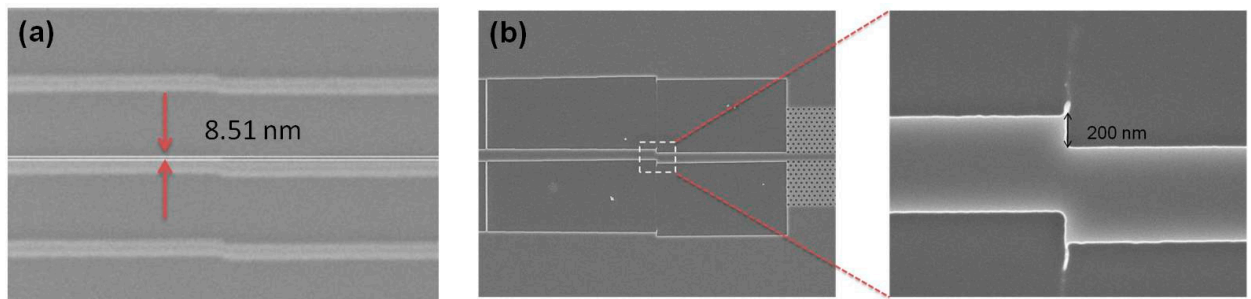


Figure 2.5 (a) SEM image of the stitching error ³⁵(reprinted from ref.35). (b) SEM image of electron lithography error due to the misalignment between different exposing layers. The zoom-in image shows a 200 nm misalignment error in the longitudinal direction.

However, the resist is not only exposed by primary electrons. A high-energy electron generates many secondary electrons in the resist, which can expose the resist as well. While the primary electrons penetrate the resist at well-defined positions, the secondary electrons are scattered off in all directions. For this reason, if one writes two structures close to each other, it can happen that after the development process just one connected structure remains instead of two separated ones. This is one of the difficulties encountered during the sample fabrication of this thesis. This effect, limiting the maximum resolution of the lithography, is called proximity effect. Thus, if the structure to be fabricated by lithography is modified or changed to a complete new design, one has to do so-called dose tests, to experimentally determine the ideal value of the dose for e-beam exposing.

During the exposure process, the control computer divides the whole pattern into many small exposure blocks and the size of these blocks is decided by the using resolution or the electron beam spot size (for example: $160 \times 160 \mu\text{m}$ at resolution of 2.5 nm). These blocks are then exposed one by one. Stitching error happens when there is any alignment offsets between the blocks (as show in Fig. 2.5a). Another type of error is due to the misalignment between different exposing layers of different resolutions (as shown in Fig 2.5b). These errors will be crucial for light propagation when it happens inside the PhC part. In order to avoid this as much as possible, one needs to properly select the resolution or block size corresponding to the size of PhC structures. If it is possible, it is better to place the highest resolution structures in one exposure block. In most occasions, extending the stabilizing time before exposure can reduce the misalignment error.

A variety of nanophotonic structures can be fabricated by other techniques. Focused ion beam is used to fabricate PhC devices by direct ion beam writing ^{36,37}. The grating-based devices fabricated by this technique have a low optical quality and limited applications ³⁸.

2.1.2 Etching

In nanofabrication, etching refers to a process by which a material is removed from the substrate or from any layer of material on the substrate. In principle, there are two different kinds of etching techniques: dry etching and wet etching.

Dry etching

In contrast to wet etching, dry etching does not utilize any liquid chemicals or etchants to remove the materials. It is generally performed in the gas phase, mostly assisted by plasma. There are two major etching mechanisms: physical etching and chemical etching. In this thesis, inductively coupled plasma etching, reactive ion etching and oxygen plasma etching are used.

In physical etching, the materials are removed by momentum transfer. The impact of incident ions on the target results in a series of collisions, and atoms from the target may be ejected. Physical etching can etch many materials and is anisotropic.

In chemical etching, species generated in the plasma react with the target and form volatile products. This etching mechanism is similar to wet etching and the etching is generally isotropic, which leads to an over etched pattern transfer. However, chemical etching can be highly material selective with suitable choice of chemistry.

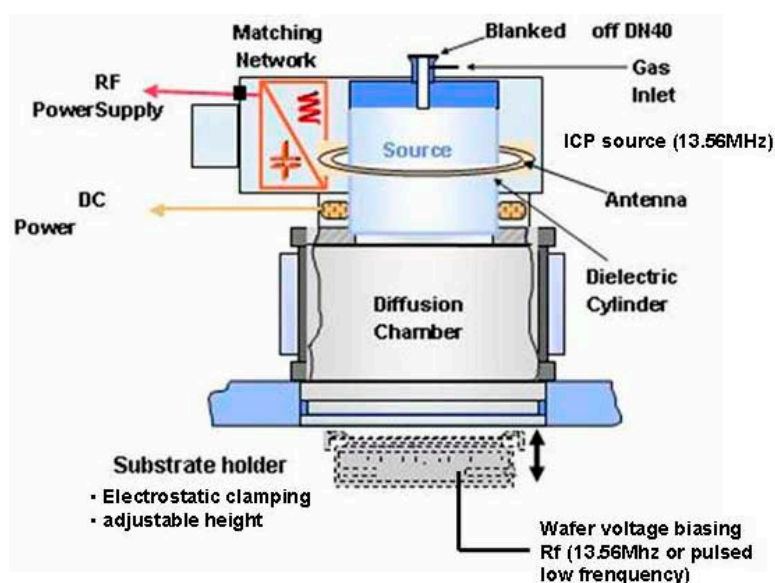


Figure 2.6 Schematic illustration of an AMS200 inductively coupled plasma etcher. It is composed of an ICP source, diffusion chamber and substrate holder³⁹ (reprinted from ref.39).

The most commonly used method for etching is the combination of physical etching and chemical etching. A typical example of this technique is ICP etching, which combines the purely physical character of sputtering with the chemical nature of plasma etching. With simultaneous bombardment of a substrate by both energetic ions and chemically reactive molecules or atoms, the material can be etched in a fast rate with anisotropic etching.

As shown in Fig. 2.6, ICP source is made with an antenna connected to an RF power supply and wrapped around an alumina cylinder. RF power (13.56MHz and 3 kW maximum) is coupled to the plasma through an inductive mode. The oscillating current in the antenna at 13.56 MHz induces an electromagnetic field in the alumina cylinder. For plasma ignition, some primary electrons collect the electromagnetic field energy (ions are too heavy to be accelerated). Inelastic collisions between hot electrons and neutrals (injected gas mixture) give ions/electrons pairs. Therefore, the main plasma is generated

inside the cylinder where the gas mixture and pressure are controlled. Diffusion chamber is a buffered zone to get better plasma uniformity. Permanent magnets surrounding the chamber limit charged particles wasting on the wall and keep a better plasma density.

The substrate holder (SH) is placed in the diffusion chamber. SH height is adjustable between 120 and 200 mm. Temperature can be adjusted between -10°C and $+40^{\circ}\text{C}$. Energy transfer between wafer and the chuck is insured by a He film applied between the wafer backside and the chuck. The pressure can be set between 3 and 15 mbar. Average ion energy is controlled through SH voltage biasing. It could be a pulsed LF voltage biasing (600 W maximum) or RF voltage biasing (13.56 MHz – 500 W maximum). The correct biasing mode is automatically selected by AMS200 when a recipe starts ³⁹.

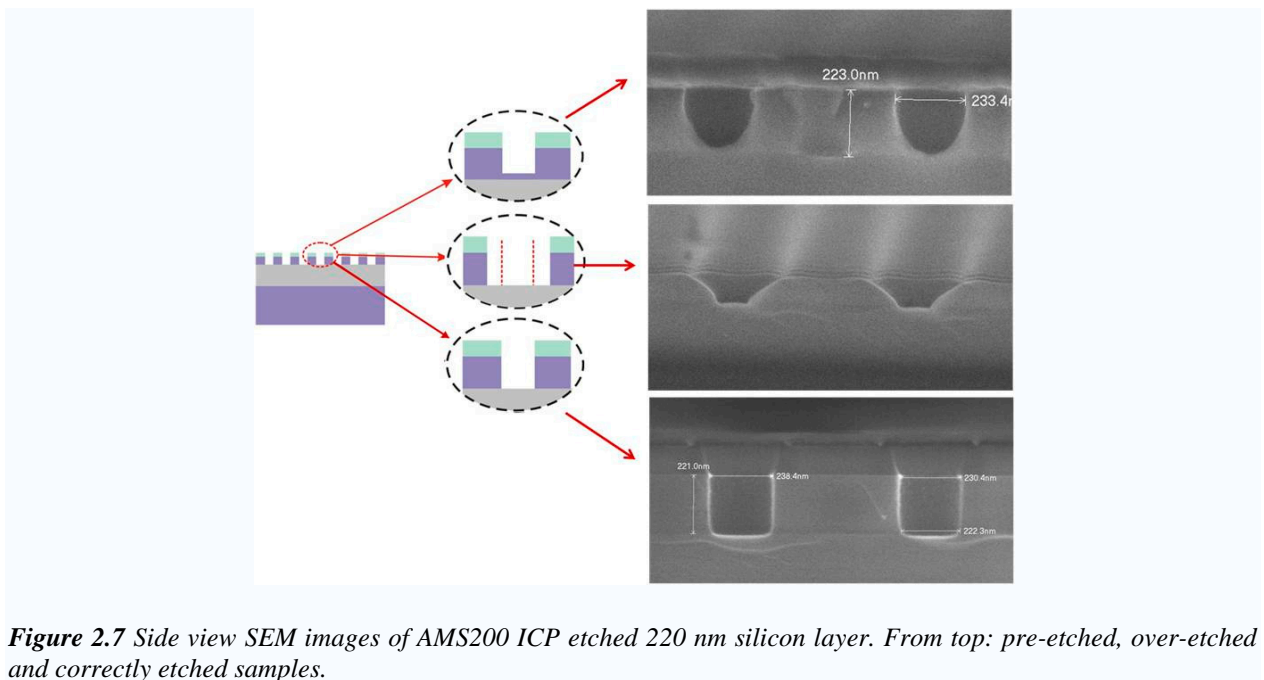


Figure 2.7 Side view SEM images of AMS200 ICP etched 220 nm silicon layer. From top: pre-etched, over-etched and correctly etched samples.

The gas mixture of C_4F_8 and SF_6 (with a ratio of 26/63 in sccm) is used for transferring PhC pattern from ZEP520 layer to silicon layer. The etching chamber pressure is 3×10^{-2} mbar. The RF generator power is 1500 W. SH height and temperature are 200 mm and 20°C , respectively. The etching time for 220 nm thick silicon layer is about 3 minutes 20 seconds. The pre-etched, over-etched and correctly etched examples are shown in Fig. 2.7.

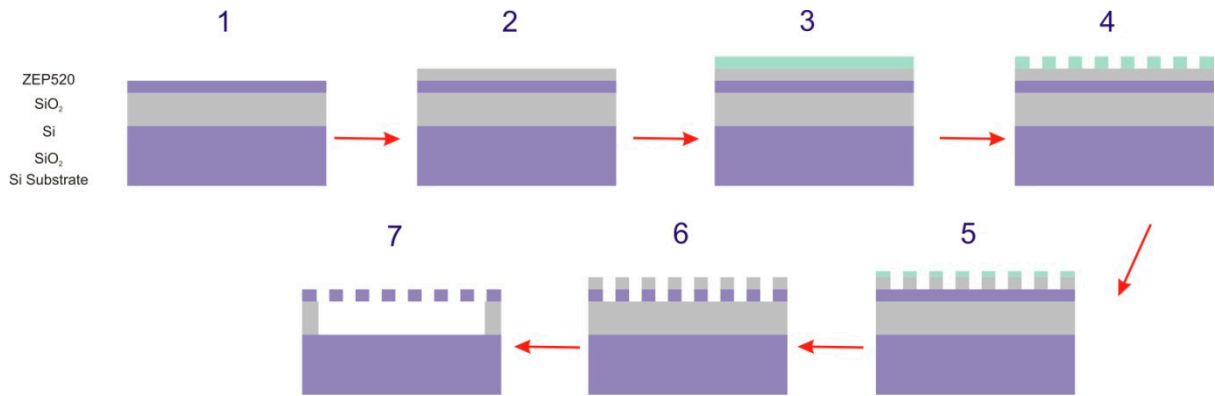


Figure 2.8 Illustration of processing flow using SiO_2 as hard etching mask. 1: Sample preparation. 2: Deposition of one SiO_2 layer by PECVD. 3: spin coating of ZEP520. 4: E-beam exposure and development. 5: Dry etching of SiO_2 layer. 6: Dry etching of SiO_2 layer. 7: Membrane release in BHF.

One common limitation of ICP dry etching is the air hole size enlargement and fabrication errors introduced in etching process^{40, 41}. This is because of the relatively low selectivity between ZEP520 and Silicon for the etching gas. One possible solution to improve the result of ICP dry etching process is to use one SiO_2 layer as hard etching mask (as shown in Fig. 2.8). Therefore, the PhC patterns will be first transferred to the SiO_2 layer by RIE dry etching and further transfer to the silicon layer afterwards. The selectivity is 20:1 between SiO_2 mask and silicon which is twice as much as that between ZEP520 mask and silicon. The small amount of the size enlargement can be achieved with high selectivity. This makes the fabrication of sub-100 nm or even smaller features possible. Therefore, this process can be useful when extreme-small structures are demanded in the design.

Wet etching

Wet etching is an etching process that utilizes liquid chemicals or etchants to remove materials from the wafer to transfer the specific patterns defined by photoresist masks into the substrate. Materials not covered by these masks are 'etched away' by the chemicals while those covered by the masks are left nearly intact.

Buffered Hydro Fluoride (BHF) acid is used to selectively wet etch the 2 μm SiO_2 layer. The etching selectivity between silicon and SiO_2 is larger than 1000. The damage for the silicon layer in this process is very weak. The SiO_2 etching rate is 70 nm/min. In our case, 30 minutes is used for etching 2 μm SiO_2 layer. A special drying process is used to avoid any damages of the silicon membrane (see **Cleaning and drying**)

2.1.3 Scanning-electron microscope

The resolution of conventional optical microscope is roughly limited by half of the wavelength of light. The first SEM was constructed by Zworykin Hiller and Snyder in 1942

and showed a resolution of down to 50 nm already. The latest SEM has a resolution of down to a few nm ⁴².

The SEM uses electrons instead of light to form an image. A beam of electrons is produced at the top of the microscope by heating of a metallic filament. The electron beam follows a vertical path through the column of the microscope. It makes its way through electromagnetic lenses which focus and direct the beam down towards the sample. Once it hits the sample, other electrons (backscattered or secondary) are ejected from the sample. Detectors collect the secondary or backscattered electrons, and convert them to a signal that is sent to a viewing screen similar to the one in an ordinary television, producing an image.

Electron gun

There are two different kinds of electron guns, which can emit free electrons. First type is a thermal electron gun, its cathode material is heated to such a high temperature that the kinetic energy of electrons higher than the potential of the material. The electrons can be emitted from the material and be accelerated by the high voltage. Second type, wherein, when a sufficiently high electric field is applied to a conductor, free electrons can be generated. The electron guns of most of the SEMs used today are combination of these two methods, to provide a constant high power. Virtual size and brightness are two very important quality parameters, which means as small as possible and as many electrons per unit area as possible. Narrow energy distribution of the electrons is also required which is strongly deteriorated by Coulomb interaction.

Lenses

Like the ray optics, lenses for electrons are required in a SEM to provide a focused and directed electron beam. The electrons are focused by electrostatic and magnetic forces. Magnetic lenses exploit the Lorentz force to direct the electrons beam towards the optical axis. However, at the same time the electrons are rotated along the optical axis. This property does not affect the focusing quality, but has a strong influence on the actual setup of the electron microscope. Depending on the focusing, the image is rotated differently, which has to be corrected appropriately. Besides magnetic lenses, one also has the opportunity to focus the electron beam via electric fields. They are not as commonly used and most often found in the gun region as a condenser lens. They can be combined with the extractor or anode used to pull electrons out of the cathode, and they are easily made for ultrahigh vacuum use. Also, aberrations in the condenser lens tend to be less important, system performance is usually dominated by the aberrations of the final lens. The term chromatic aberration denotes that electrons of different energy are focused differently. Spherical aberrations of electron lenses are characterized by a stronger focusing power of the exterior regions than the interior regions of the lens.

Detection

There are basically two possibilities to detect the signal: First, electrons, which are scattered or reflected back from the sample, can be detected. These electrons mainly have energies of some keV. The corresponding detector is located directly at the bottom end of the electron column. The second possibility is to detect secondary electrons, which are excited in the object by the primary electrons of the focused electron beam and which finally escape the sample. The energy of these electrons is usually just a few electron volts. In order to detect these low-energy electrons an additional grid is mounted in front of the detector to generate an electric field between detector and grid. Thus the electrons gain additional kinetic energy and are finally detected by a so-called Everhart-Thornley detector.

In order to investigate a non conductive sample, coating with a thin film of an electrically conducting material has to be used. Otherwise, since in the case of insulating samples, surface charges build up and deflect the course of secondary electrons. Therefore, for non-conducting samples such as dielectrics, a thin layer of graphite or metal is usually deposited to make them conductive and prevent surface charging.

The advantage of SEM over TEM is that it provides a tremendous depth of focus. Thus, a three-dimensional image of the exposed surface of a sample can be obtained. In contrast, TEM provides only a transmission contrast in a thin sample. But the resolution obtained by TEM can be better than that for SEM. In the latter case, typical resolutions are about 10 nm. Therefore information on size and shapes of nano-particles less than 10 nm, TEM is the appropriate technique.

2.1.4 Atomic force microscope

The atomic force microscope (AFM) is a very high resolution type of scanning probe microscope, with demonstrated resolution of fractions of a nanometer, more than 1000 times better than the optical diffraction limit. The precursor to the AFM, the scanning tunneling microscope, was developed by Gerd Binnig and Heinrich Rohrer in the early 1980s, a development that earned them the Nobel Prize for Physics in 1986. The AFM is one of the foremost tools for imaging, measuring and manipulating matter at the nano-scale ⁴³.

Atomic force microscopy detects the overall forces between a probe tip and the sample surface. In this case, the probe is attached to a cantilever-type spring. In contrast to STM, this imaging technique is not dependent on the electrical conductivity of the sample. The force exerted on the tip by the sample surface produces a bend of the cantilever. By using a cantilever with known spring constant C , the net force F can be directly obtained from the deflection, X , of the cantilever according to equation $F=CX$. The two frequently used modes employed to produce AFM images are the contact mode and the tapping mode.

In essence, the AFM operates by measuring attractive or repulsive forces between a tip and the sample. In the contact mode, the tip operates in the repulsive regime (during scan, the tip comes in contact with the sample); while in the noncontact mode, it operates in the attractive regime (the tip is very close to the sample, but not in contact with it). The contact mode can be used on samples in air and liquids, while the noncontact mode cannot be used in liquids.

The AFM has several advantages over the scanning electron microscope (SEM). Unlike the electron microscope which provides a two-dimensional projection or a two-dimensional image of a sample, the AFM provides a true three-dimensional surface profile. Additionally, samples viewed by AFM do not require any special treatments (such as metal/carbon coatings) that would irreversibly change or damage the sample. While an electron microscope needs an expensive vacuum environment for proper operation, most AFM modes can work perfectly well in ambient air or even in a liquid environment. This makes it possible to study biological macromolecules and even living organisms. In principle, AFM can provide higher resolution than SEM. It has been shown to give true atomic resolution in ultra-high vacuum (UHV) and, more recently, in liquid environments. High resolution AFM is comparable in resolution to Scanning Tunneling Microscopy and Transmission Electron Microscopy.

A disadvantage of AFM compared with the scanning electron microscope (SEM) is the image size. The SEM can image an area on the order of millimeters by millimeters with a depth of field on the order of millimeters. The AFM can only image a maximum height on the order of micrometers and a maximum scanning area of around 150 by 150 micrometers. Another inconvenience is that an incorrect choice of tip for the required resolution can lead to image artifacts. In most of cases, the AFM could not scan images as fast as an SEM, requiring several minutes for a typical scan, while an SEM is capable of scanning at near real-time (although at relatively low quality) after the chamber is evacuated. The relatively slow rate of scanning during AFM imaging often leads to a thermal drift in the image (Lapshin, 2004, 2007), making the AFM microscope less suited for measuring accurate distances between artifacts on the image. Due to the nature of AFM probes, they cannot normally measure steep walls or overhangs. Specially made cantilevers can be modulated sideways as well as up and down (as with dynamic contact and non-contact modes) to measure sidewalls, at the cost of more expensive cantilevers and additional artifacts.

2.2 GaAs/AlGaAs based photonic crystal devices fabrication procedures

The GaAs/AlGaAs based active PhC devices is discussed for applications in THz lasers. The processing flow is flowing:

Wafer bonding: QCL (10-14 μm thick) layer and 700 nm thick $\text{Al}_{0.3}\text{Ga}_{0.7}\text{As}$ etching stop layer are grown by Molecular Beam Epitaxy (MBE) on a semi-insulating GaAs substrate. Ti/Au (5 nm/500 nm) layers were evaporated onto both the QCL layer and a n+ doped substrate, the Au/Au surfaces of these wafers were then bonded together by means of thermo-compression wafer bonding in air at 300 °C with 4.5 MPa pressure for 45 minutes⁴⁴. Polishing of the substrate and then selective wet etching with a mixture solution containing citric acid (citric: H_2O_2 : H_2O = 3: 2: 3 in weight) are performed. The wet etching stops when etching stop layer is reached.

SiO_2 layer deposition: After a cleaning step, the etching stop layer is removed by wet etching with 40% HF acid for 1 minute. A 1000 nm thick SiO_2 layer was deposited by using the Plasma Enhanced Chemical Vapor Deposition method (PECVD, Oxford PlasmaLab100) on the QCL layer.

Patterning of the photoresist layer: Primer and positive resist (HDMS and AZ5214) is spin-coated onto the substrate surface for 10 and 30 seconds both at 5000 rpm. The sample is left in air for 5 minutes and soft baked at 90 °C for 5 minutes. PhC patterns are defined by photolithography in photoresist layer. The exposure time is 4 seconds.

Exposure: Designed PhC patterns are exposed by Microtech MJB3 mask aligner for 4 seconds exposure time.

Development and hard bake: The sample is then developed in MF319 for 60 seconds. Afterwards, the sample is rinsed in water for 15 second to stop the development process. At last, the sample is dried by N_2 gas and baked at 115 °C for 15 minutes.

Hard mask etching: PhC patterns are transferred into SiO_2 layer by Oxford Plasmalab system 80 plus RIE Etcher with a gas mixture of CHF_3 and Ar.

QCL layer etching: The sample is clean and ultrasonicated for 5 minutes at 35 kHz in acetone to remove the remaining photoresist. PhC patterns are transferred into QCL layer by Sentech ICP-RIE SI 500 RIE etcher with a gas mixture of BCl_3 , Cl_2 and N_2 .

BCB planarization: The sample is cleaned in BHF for 10 seconds to get smooth pillar sidewall. Three layers of BCB (CYCLOTENE 3022-46) are spin-coated and baked one by one on the sample (discuss in details later).

BCB etching: The BCB layer is etched down to 300-800 nm lower than QCL layer by Oxford Plasmalab system 80 plus RIE Etcher with a gas mixture of CF_4 and O_2 .

SiO_2 mask wet etching: The sample is immersed in BHF for 4 minutes to selectively etch the rest of the SiO_2 mask layer.

Isolating layer (optional): The isolating layer is defined in negative resist NLOF 2070 layer by photolithography with 6 seconds exposure time. The sample is then developed in MF319 for 120 seconds. The 100 nm thick SiO_2 is deposited by PECVD. Then the sample is left in acetone for 3 hours for lift-off.

Top contact pad layer: The top contact pad layer is defined in the negative resist NLOF 2070 layer by photolithography with 6 seconds of exposure time. The sample is then developed in MF319 for 120 seconds. The 5/1200 nm thick Ti/Au layer was deposited by Ebeam 2000 electron beam evaporator. Then the sample is left in acetone for 5 hours for lift-off.

Bottom contact layer: The 10/250 nm thick Ti/Au layer was deposited by Ebeam 2000 electron beam evaporator.

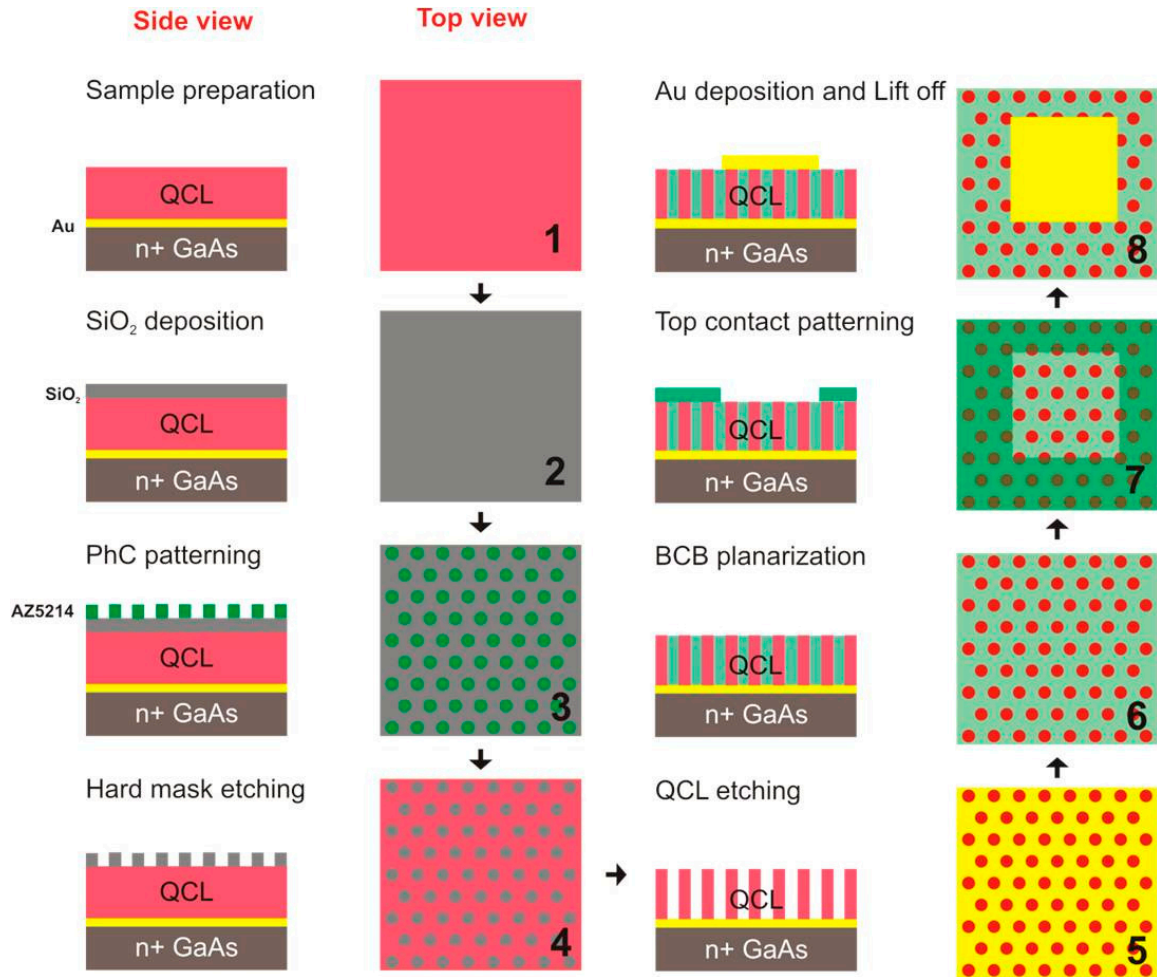


Figure 2.9 Illustration of THz PhC QC laser processing flow. 1: Sample preparation and wafer bonding. 2: Deposition of one SiO_2 hard mask layer by PECVD. 3: Photolithography and development. 4: RIE etching of SiO_2 layer and development. 5: ICP etching of the QCL layer. 6: BCB planarization. 7: Top contact pad patterning in NLOF 2070. 8: Top contact pad deposition and lift-off.

2.2.1 Plasma Enhanced Chemical Vapor Deposition (PECVD)

Plasma Enhanced Chemical Vapor Deposition (PECVD) is an excellent alternative for the deposition of a variety of thin films at lower temperatures than those utilized in CVD reactors without settling for a lesser film quality. For example, high quality silicon dioxide films can be deposited at 300 to 350 degrees centigrade while CVD requires temperatures in the range of 650 to 850 degrees centigrade to produce similar quality films.

PECVD uses electrical energy to generate a glow discharge (plasma) in which the energy is transferred into a gas mixture. This transforms the gas mixture into reactive radicals, ions, neutral atoms and molecules, and other highly excited species. These atomic and molecular fragments interact with a substrate and, depending on the nature of these interactions, either etching or deposition processes occur at the substrate. Since the formation of the reactive and energetic species in the gas phase occurs by collision in the gas phase, the substrate can be maintained at a low temperature. Hence, film formation can occur on substrates at a lower temperature than is possible in the conventional CVD process, which is a major advantage of PECVD.



Figure 2.10 Image of Oxford PlasmaLab100 PECVD ⁴⁵(reprinted from ref.45).

Oxford PlasmaLab100 PECVD (as shown in Fig. 2.10) is used in this thesis. It is used to deposit SiO₂ layer with two different recipes. The gas mixture of N₂98%/SiH₄2% and N₂O (with a ratio of 400/710 in sccm) is used for standard recipe. The etching chamber pressure is 1000 mTorr with substrate temperature at 300 °C. The deposition rate is 62 nm/min. For some special layers which are highly sensitive to the high temperature, low temperature recipe is used. The gas mixture of N₂98%/SiH₄2% and N₂O (with a ratio of 400/710 in sccm) is used for the standard recipe. The etching chamber pressure is 1000 mTorr with substrate temperature at 100 °C. The deposition rate is 40 nm/min.

2.2.2 Reactive Ion Etching (RIE)

The working principle of the Reactive Ion Etching has been introduced in the previous section. Oxford Plasmalab system 80 plus RIE Etcher Sentech ICP-RIE SI 500 RIE etcher are used to etch SiO₂ hard mask layer and GaAs/AlGaAs QCL layer, respectively. For transferring PhC pattern into SiO₂ layer, the gas mixture of CHF₃/Ar (with a ratio of 25/25 in sccm) is used for the standard recipe. The etching chamber pressure is 30 mTorr with a RF power of 200 W. The SiO₂ etching rate is 31 nm/min. For the 1000 nm SiO₂ layer, the etching time is 32 minutes. Then the sample is put in acetone in order to remove the rest photoresist layer. The resist layer will be very difficult to remove after the QCL layer etching step. Therefore, we need to make sure no resist left before the next processing step. For this step, ultrasonic in acetone for 5 minutes is a very effective way to tear off the resist layer. In order to avoid the damage to the QCL layer in the ultrasonic bath, relatively low frequency is used (30-35 kHz). Fig. 2.11 shows the microscopic images of sample before and after the ultrasonic step.

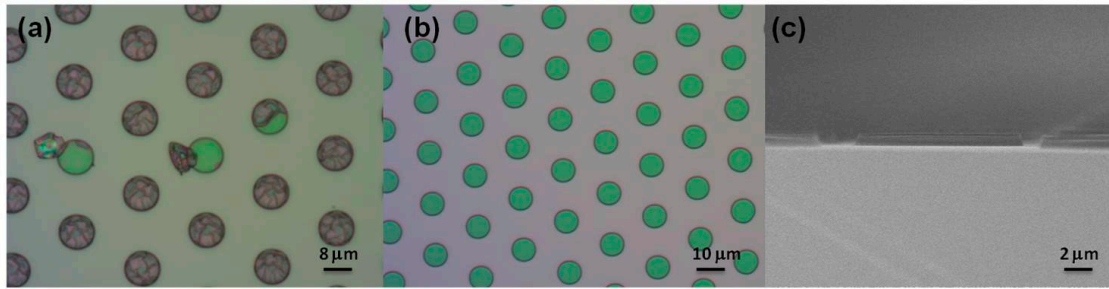


Figure 2.11 (a) Microscopic image of sample before the ultrasonic bath (b) Microscopic image of the sample after rinsing in the ultrasonic bath for 5 minutes at 35 KHz in acetone (c) SEM image of side view of SiO₂ hard mask.

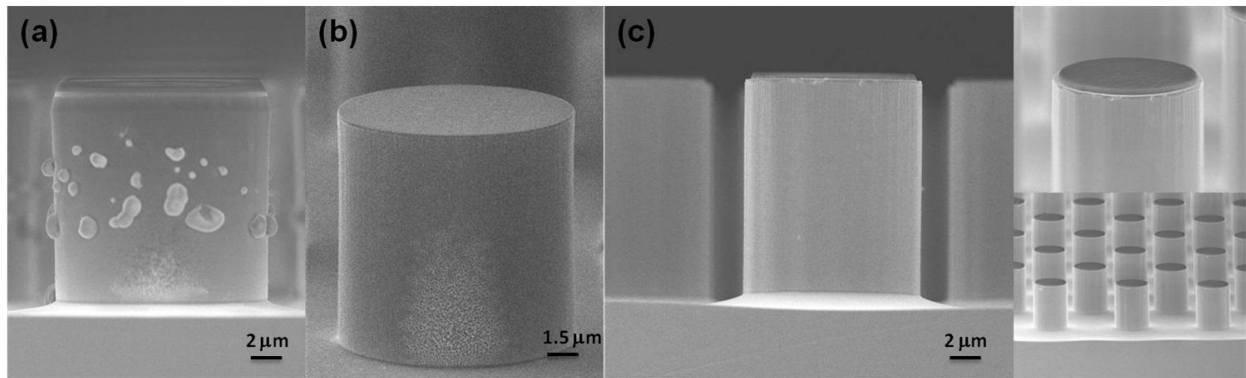


Figure 2.12 (a) SEM image of the QCL pillar after RIE dry etching (dummy sample). (b) SEM image of the QCL pillar after 15 seconds BHF cleaning and 4 minutes SiO₂ mask wet etching (dummy sample). (c) SEM image of QCL pillars after RIE dry etching and 15 seconds BHF ready for BCB planarization.

Sentech ICP-RIE SI 500 RIE etcher is used to etch GaAs/AlGaAs QCL layer. The gas mixture of BCl₃/Cl₂/N₂ (with a ratio of 12/10/4 in sccm) is used for the optimized recipe.

The etching chamber pressure is 0.33 Pa with a RF power of 500 W. The substrate temperature is 30 °C. The etching rate of the QCL layer is 17.5 nm/second. The etching time needs to be controlled accurately. Pre-etch which does not etch through the QCL layer will decrease the lasing efficiency. Over-etch which starts to etch the bottom Au layer will cause the sputtering of the gold nanoparticles onto the QCL pillar's sidewall and therefore increase the loss of the device. As shown in Fig. 2.11 a, after the QCL layer etching process, some side product of the etching process left on the sidewall of the QCL pillars. This will introduce extra losses in the system or even prevent the device from lasing. The sample is cleaned in BHF for 10 seconds to remove these side products. Later experimental result shows that this process does not damage the QCL layer. The QCL pillar after 15 seconds of cleaning in BHF and 4 minutes of SiO₂ mask wet etching process is shown in Fig. 2.12 b. Ultra smooth sidewalls and nearly perfect edges have been achieved. For the real sample, the SiO₂ mask wet etching process is after the BCB planarization step. Fig. 2.12 c shows the real sample after BHF cleaning and is ready for BCB planarization. The SiO₂ mask is on top of each pillar in dark color. These masks can protect the QCL pillar for damaging in the BCB etching process afterwards.

2.2.3 BCB planarization

The top contact plasmon layer is required for the light confinement and uniform current injection purpose. This is a challenging step in the fabrication of pillar type PhC QCL devices. The QCL layer needs to be planarized after the dry etching step. Furthermore the planarization provides freedom on the definition of surface plasmon patterns, and potentially it forms a better heat-conducting environment surrounding the QCL material than air ⁴⁴. A multi-layer planarization technique based on BCB (CYCLOTENE 3022-46) was applied to address this issue. The BCB's low refractive index, low curing temperature, low loss (as shown in Fig. 2. 13), and ability to be dry etched are the most important features for this purpose.

Due to the thickness of the QCL layer is about 12-15 μm and the maximum thickness of the single BCB layer is about 5 μm, multi-layer BCB planarization is performed. The primer AP300 and the first layer are spin-coated onto the sample surface for 10 and 40 seconds with 5000 and 4000 rpm, respectively. The first layer is baked on a program controlled hot plate. The baking curve is: Firstly, start at 75 °C and increase to 175 °C with 2°C /min. Secondly, dwelling at 175 °C for 3 hours. Thirdly, increase to 210 °C with 1 °C/min. Fourthly, dwelling at 210 °C for 1 hour. Last step, decrease to 75 °C with 5 °C/min. The second layer is spin-coated on the first layer for 40 seconds with 5000 rpm. Then baking curves of the second is the same as that of the first layer. The third layer is spin-coated on the first layer for 40 seconds with 5000 rpm. The baking curve is: Firstly, start at 75 °C and increase to 175 °C with 2°C /min. Secondly, dwelling at 175 °C for 3 hours. Thirdly, increase to 250 °C with 1 °C/min. Fourthly, dwelling at 250 °C for 1 hour. Last step,

decrease to 75 °C with 5 °C/min (as shown in Fig. 2. 14). N₂ purge is required when the baking temperature higher than 180 °C to prevent the BCB oxidation.

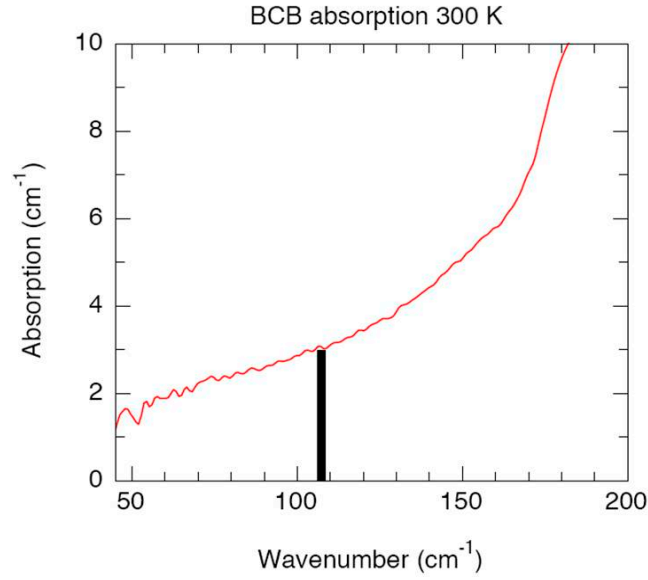


Figure 2.13 Measured absorption of BCB at 300 K. The transmission spectrum of a 3 mm thick hard baked BCB layer is measured at THz frequency range. The materials loss around 3 THz is 3.5 cm⁻¹ which is indicated in black bar in the figure.

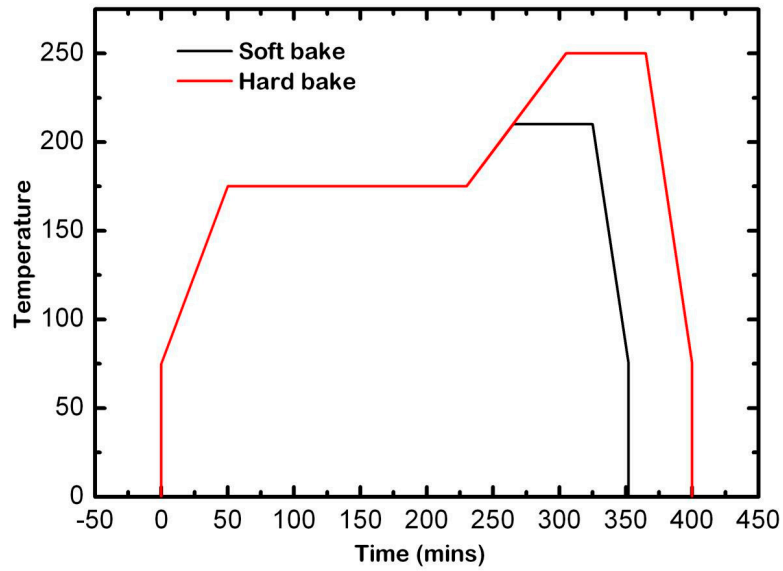


Figure 2.14 BCB baking curves. Soft baking curve is in black and hard baking curve is in red.

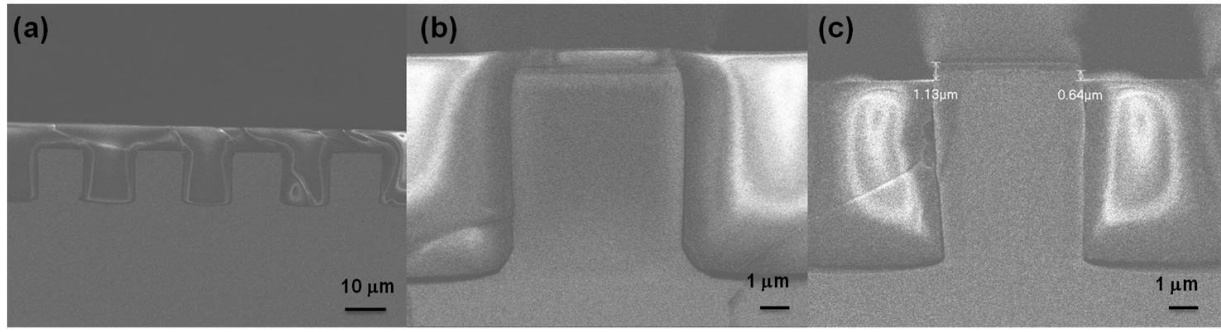


Figure 2.15 (a) SEM side view image of the sample after three layer BCB planarization. (b) SEM side view image of the sample after 4 minutes BCB dry etching. (c) SEM side view image of the sample after BCB dry etching and ready for wet etching.

After 3 layers of spin coating and baking, the entire sample is completely covered with BCB with a smooth surface as seen in Fig. 2.15 (a) (b). The measured surface roughness is negligible comparing to the 12 μm total thickness. The BCB was etched without any surface preparation on the sample using a CF_4/O_2 plasma mixture (with ratio of 40/60 in sccm) in the RIE. The chamber pressure is kept at 100 mTorr with a radio frequency (RF) power of 200 W. The BCB was etched to a depth a little bit lower than the top of the pillar, e.g., ~ 500 nm (Fig. 2.15 (c)), in order to guarantee that the remaining SiO_2 mask can be easily removed through the following wet etching. The etching rate is 600 nm/min.

2.2.4 E-beam evaporator

Thermo evaporation (resistance heated evaporation) and electron beam evaporation (e-beam evaporation) are two different techniques of evaporation. The technique of vapor deposition by thermo effect is the simplest. The disadvantages of this technique are: Potential contamination by the pod itself, the impossibility to evaporate metals with high melting temperature, the maximum thickness of the deposited layer is limited by the amount of metal in the pod.

The technique of vapor deposition by electron beam consists of depositing the grains of the granular material or small pieces of wire in a crucible. A beam of high energy electrons is directed onto the material. The electron source is a tungsten filament heated by a high current. Electrons are emitted from the surface of the tungsten at a low speed. A negative voltage of -10kV to -4kV is applied to the filament, which causes the acceleration of the electrons along the lines of the electrostatic field in the direction of the lower edge of the plate constituting the anode. However, the geometry of the cathode placed in front of the filament allows avoiding the impact of the electrons on the lower edge of the anode. The beam is deflected 270° by a magnetic field. The kinetic energy of the electrons is converted into heat at the point of impact. The flow of energy is of $104 \text{ W}\cdot\text{cm}^{-2}$. The electron

beam can melt and evaporate any material inside as the heat input is greater than the losses. The beam is concentrated at the surface of the material so that the melted material can be contained in a cooled receiver. In fact, only the surface of the material is molten. The material in contact with the crucible walls is solid. This eliminates the problem of contamination by the crucible and can deposit layers of very high purity. The advantage of this technique is the purity of the deposited layers. The two main drawbacks associated with this technique are: The emission of X-rays can damage the surfaces of the substrates. Ejection of droplets from the crucible can be deposited on substrates where excessive power is used.

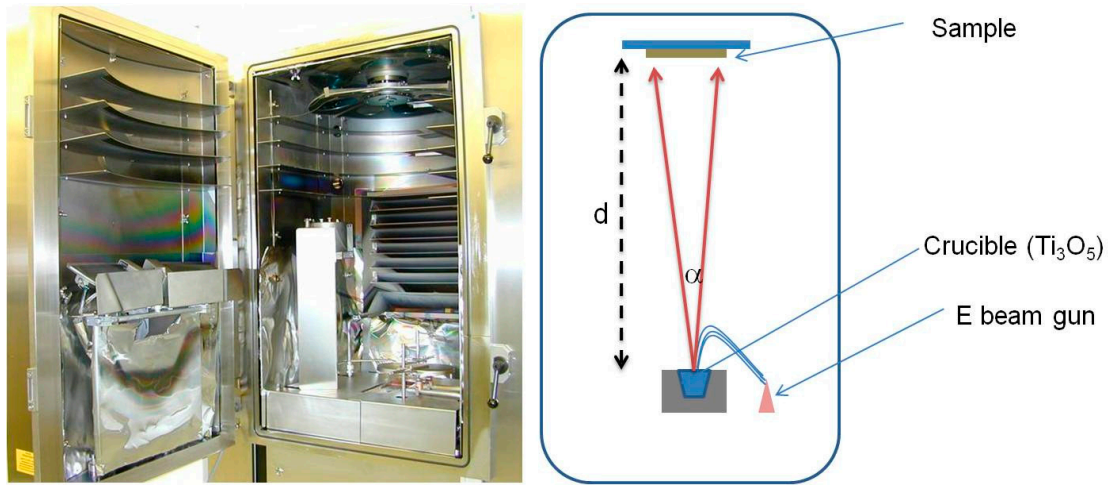


Figure 2.16 Real image ⁴⁶(left, reprinted from ref.15) and schematic image (right) of an electron beam evaporator. d is the distance for the source to the sample, which is 1010mm. α is the dispersion angle which is 0.02 degree for a 15mm long sample

One thick layer of top contact pad Ti/Au (4 nm/ 1300 nm) is evaporated on the sample. The high voltage is 8 kV with current of 40 mA/56 mA and the deposition rate is 0.12 nm/ 0.20 nm per second, respectively. This layer can provide a high enough light confinement and compensate the BCB over etching and surface roughness. For this step, the Au deposition rate needs to be lower than 0.30 nm/s. It is always important to avoid high e-beam power, which can introduce additional contaminations during the evaporation process.

2.3 Special cases and summary

At the end of this chapter, something common but important about device fabrication that cannot be learned from books need to be discussed. There is always a question to be answered: what is the key issue in fabrication? The answer can have many different formulations: advanced equipments, high-class clean room, experimentally proved process flow, personal interests in this field and so on. However, my own answer rests in **details**. For device fabrication, the key issue is 'details'. The way samples are held,

the way samples are cleaned, the way samples are dried and even the way samples are transferred can make the final result totally different. Therefore, details are the key element in the fabrication world but are underestimated most of the time.

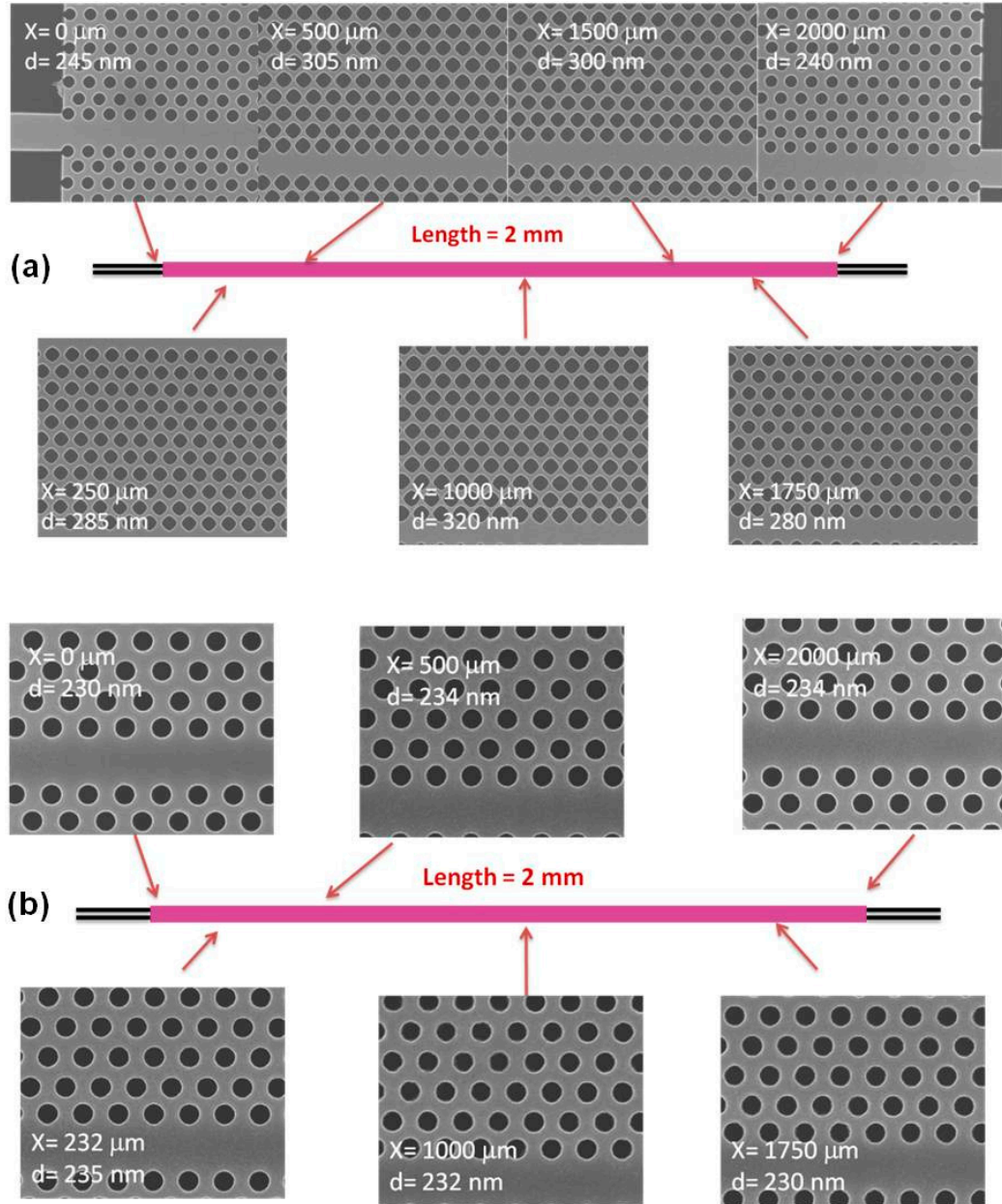


Figure 2.17 Fabrication of 2 mm long W1 waveguide with (a) and without (b) 60 second O_2 plasma cleaning before BHF wet etching. X is the SEM image in the W1 structure (indicated by red arrows), d is the diameter of the air hole in the corresponding images. (SEM images in (a) and (b) have different magnifications)

There is a good example for solving special difficulties during fabrication procedures. As shown in Fig. 2.17 a, the W1 waveguide (2 mm long) is fabricated with the standard silicon membrane process. The diameter of the air hole is 20 to 90 nm larger than design (250 to 320 nm instead of 230 nm). The size of the air holes has a maximum value in the centre of the W1 waveguide and reaches a minimum value at both ends. The shape of the air hole close to the centre of the W1 waveguide is square-like instead of circular. By checking every single fabrication step, the only difference between this sample and other 'normal' sample is the length of the W1 PhC waveguide. The 'normal' samples fabricated before this 2 mm long W1 waveguide have a length between 50 μm to 200 μm . Each sample, after the wet etching window exposure and before the BHF wet etching, is cleaned by O_2 plasma (power 100 W, 0.5 mbar) for 60 seconds to make sure no photoresist left from previous photolithography step. The wet etching window is O_2 cleaning window, which is increased 10 to 40 times (from 50/200 to 2000 μm). As shown in Fig 2.18 a, the etching rate is proportional to the size of the etching window. For a 2 mm long W1 waveguide, 60 seconds is so long that have already damaged the air hole. This is the reason for the increase of the size of the air holes. Etching ions are scattered back by the SiO_2 layer and damage the side wall of the air holes. This effect leads to the square-shape air holes. In order to solve this air hole damage effect, the O_2 plasma cleaning step is modified to 10 seconds with 50 W powers. The sample fabricated after this optimization step is shown in Fig. 2. 17b, the different SEM images of the air holes in this 2 mm long W1 waveguide show a less than 5 nm air hole diameter variation.

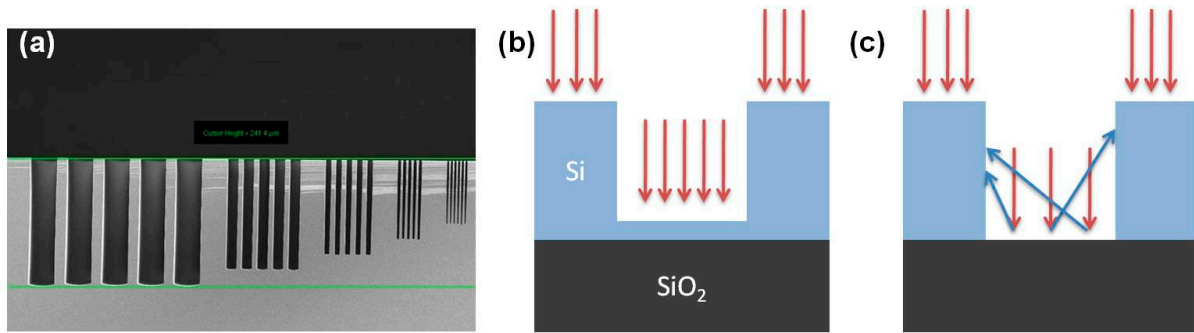


Figure 2.18 (a) The drying etching rate is proportional to the size of the etching window ³⁹(reprinted from ref.39). (b) Etching of the silicon layer before the etching of the SiO_2 layer. (c) Etching of the silicon layer after reaching the SiO_2 layer. Etching ions are scattered back and damage the side wall of the air holes.

There are certainly other factors that are also important beside the 'details'. One of them is to cultivate good habits. It is imperative to clean the sample box before putting a sample inside, to keep the development paddling frequency constant and so on. These will be easy if one makes it a habit and that helps a lot in the better processing of samples. The other factor is to imagine the processing flow in the mind, step by step, as accurately as possible, before starting it. By doing so, it is possible to identify the issues, which might happen later and hence be more confident with the whole processing. Another one is to

develop the ability to remain calm when an unexpected situation arises during the processing. This can avoid the situation spiraling down further and in limiting the damages caused. Last but not the least, it is always important to summarize both the good and bad results of each processing step, which will be helpful for the improvement of the next fabrication process.

Chapter 3

Coupling light into photonic crystal devices

A high efficiency in the coupling of light into the PhC devices is preferred in order to carefully investigate their optical properties. There are three major issues concerning the sequence of light propagation in the PhC devices that are considered in this thesis. Firstly, light from an input laser diode has to be coupled to the input facet of the ridge waveguide. It is highly important to increase the transmittance through the ridge waveguides by decreasing the reflection losses due to the Fabry-Perot interferences at the interface. Secondly, at the interface between the PhC device and the ridge waveguide, the coupling losses due to the mode mismatch have to be minimized including the propagation losses between fast and slow light regions. Thirdly, lower propagation losses are preferred inside the PhC structures. Any other possible mechanisms that can consequently introduce propagation losses have to be taken into account. It is also desirable to avoid thermo-optical damages for applications that require higher intensities inside the PhC devices and hence it is crucial to overcome the above-mentioned challenges.

In this chapter, different methods will be experimentally investigated to couple light into PhC devices for various purposes. This chapter is organized in the following manner: In Section 3.1, methods for coupling light from the optical fiber to the sample facet are discussed. The performances of SiN and TiO₂ antireflection coatings on the facets are compared to that of SU-8 couplers. In Section 3.2, the PhC group index tapers are used to overcome the mismatch in the group velocity between the fast light in the strip waveguide and the slow light in the guided mode of PhC waveguide. A few reasons for propagation losses inside the PhC are elaborated in Section 3.3.

3.1 Coupling from the lensed fiber to the facet of ridge waveguide

Two-dimensional PhC membranes on SOI wafers can achieve strong light confinement by index guiding, which is important to achieve the desired optical properties. However, large losses in the coupling of the SOI PhC device and the scattering losses in the PhC waveguide due to structural irregularities remain as the major challenges that limit further exploration. Large coupling losses are caused by the minimal geometric overlap and poor impedance matching of the optical modes between the input fiber ($5 \times 5 \mu\text{m}^2$) and

silicon waveguide ($3 \times 0.22 \mu\text{m}^2$). Furthermore, the small cross-sectional area and the large effective refractive index of the waveguide mode prohibit efficient coupling from the fiber. Silicon strip waveguides are commonly used to facilitate the coupling into the PhC waveguide. However, multiple mismatched interfaces between the fibers and the end-facets or between the waveguides and the PhCs result in strong Fabry-Perot oscillations in the transmission spectra, which can easily reach 30% of the signal amplitude (as shown in Fig. 3.1). As a result, intrinsic spectral features arising from the underlying photonic band structure are hidden in these Fabry-Perot interference fringes, rendering optical experiments more complex or even impossible. Many different approaches have been proposed to overcome these issues ⁴⁷⁻⁵¹. Different methods to improve the coupling efficiency and reduce Fabry-Perot fringes will be discussed in this section.

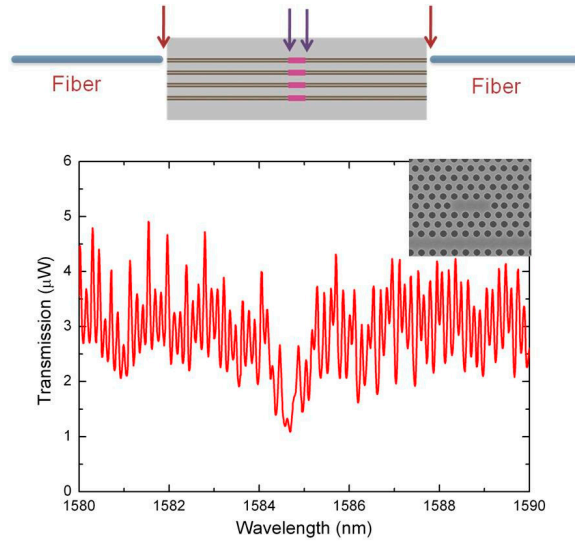


Figure 3.1 Top: Illustration of coupling losses at facets (in red arrows) and at PhC interfaces (in blue arrows). Bottom: Transmission spectrum of a fabricated PhC device. The W1 waveguide is side coupled with 2 standard L3 cavities. Intrinsic spectral features arising from the underlying photonic band structure are hidden in this over 30% of the signal amplitude Fabry-Perot noise. Inset is the SEM image of the device. $a=440 \text{ nm}$, $d=270 \text{ nm}$.

J. H. Schmidt and coworkers demonstrated the use of sub-wavelength gratings etched onto the facets of SOI ridge waveguides (as shown in Fig. 3.2) as a means to reduce facet reflectivity by the gradient-index effect ⁴⁹. Reflectivity values as low as 2.0% and 2.4% for the fundamental TE and TM modes, respectively, were demonstrated experimentally for an input wavelength at $1.55 \mu\text{m}$.

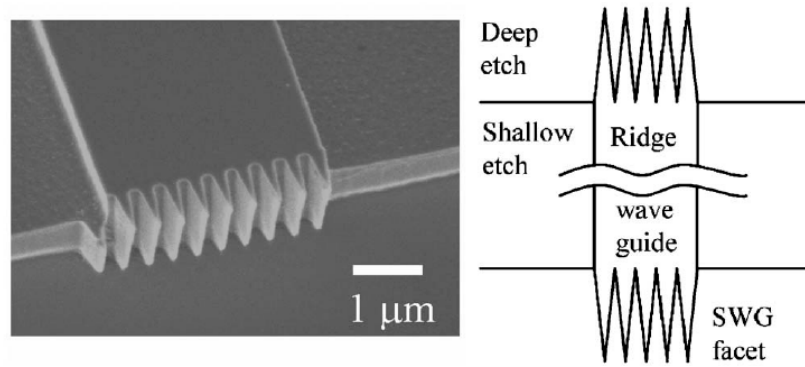


Figure 3.2 SEM image of an SOI ridge waveguide facet patterned with a triangular sub-wavelength grating (SWG) structure and the corresponding schematic top view of the device ⁴⁹(reprinted from ref.49).

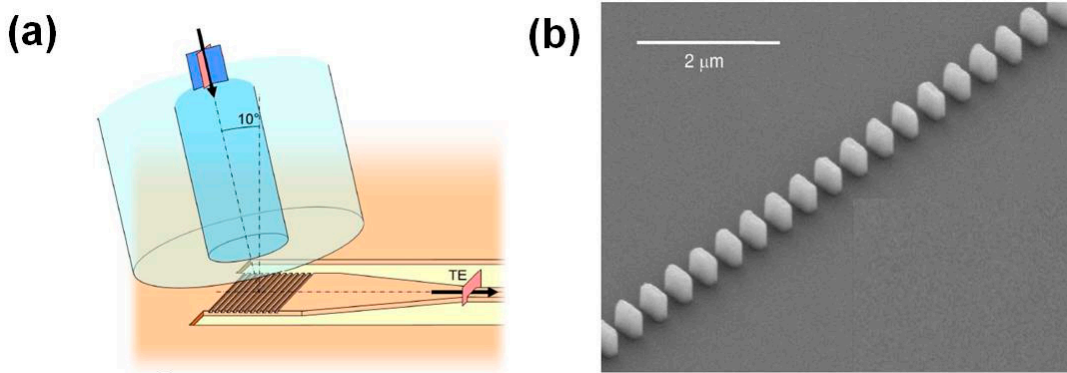


Figure 3.3 (a) Grating couplers between the optical fiber and the nanophotonic waveguide ^{50, 52}(reprinted from ref.52) (b) SEM image of a sub-wavelength grating waveguide ⁵¹(reprinted from ref.51).

As shown in Fig 3.3a, the surface-coupling approach uses waveguide gratings (or metal grating couplers ⁴⁸) to diffract light into the silicon waveguide or from the output of the waveguide to an optical fiber. Sub-wavelength gratings (SWG) are also used to engineer the refractive index in photonic waveguides (in Fig 3.3b), including practical components such as input couplers and multiplexer circuits. This technique allows for direct control of the mode confinement by changing the refractive index of a waveguide core over a broad wavelength range.

3.1.1 SiN anti-reflection coating

In order to improve the light coupling efficiency between the input fiber and the strip waveguide and hence reduce the strong Fabry-Perot oscillations, an anti-reflection coating is applied on both facets of the device. Anti-reflection coatings are typically applied onto the surface of optical devices to reduce the reflections at the interfaces. This can improve the coupling efficiency and consequently reduce the losses. Lord Rayleigh

proposed the first anti-reflection coating in 1886. A single layer anti-reflection coating consists of one layer of transparent material, which behaves as a quarter-wave plate. The refractive index of this layer is defined by:

$$n_2 = \sqrt{n_1 n_3}, \quad (3.1)$$

For the silicon ridge waveguide, $n_1 = 1$, $n_3 = 3.47$, $n_2 = 1.863$. In the case of guided modes, the effective refractive index changes for different guided modes or polarizations and the exact effective refractive index needs to be taken into account. As shown in Fig. 3.2, this quarter-wave plate can provide a destructive interference between light reflected from the silicon layer (n_3) and the coating layer (n_2). The thickness of this layer is given by:

$$\text{thickness} = \lambda/4n_2, \quad (3.2)$$

Here, λ is the central wavelength and n is the refractive index of the coating material.

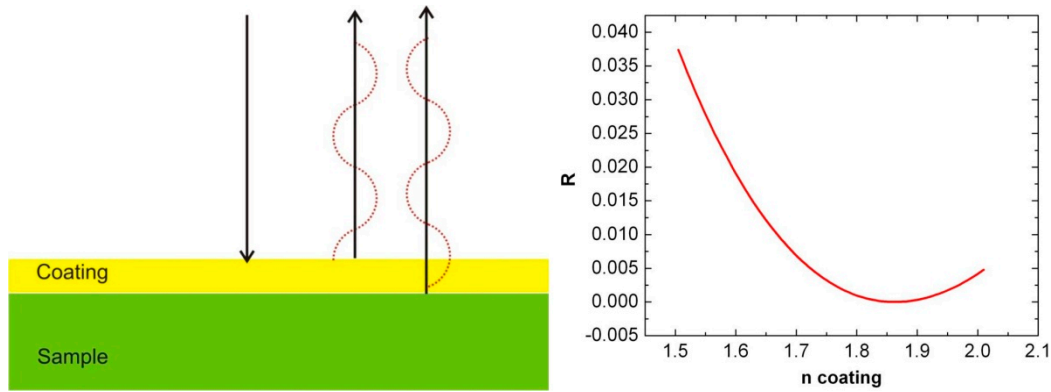


Figure 3.4 Left: Illustration of the anti-reflection coating as a single quarter-wave plate. Right: Simulated reflectivity changes with the refractive index of the coating material. The minimum reflectivity is observed at 1.85.

Based on the above discussion, Si_3N_4 is selected as the coating material. As $1.55 \mu\text{m}$ is the central wavelength, the thickness of the coating layer is found to be 200 nm. A single 200 nm Si_3N_4 layer is deposited on the facet of the sample. A special sample holder is designed for this purpose (as shown in Fig. 3.5). The sample is carefully oriented with its top surface (the side with the PhC devices) facing the holder surface in order to avoid the deposition on the sample surface. Oxford PlasmaLab100 PECVD (as shown in Fig. 2.10) is used for the Si_3N_4 layer deposition. A gas mixture of N_2 98% / SiH_4 2% and N_2O (with a ratio of 400/710 in sccm) is used as the standard recipe. The etching chamber pressure is 1000 mTorr with substrate temperature at 300°C . The deposition rate is 25.5 nm/min.

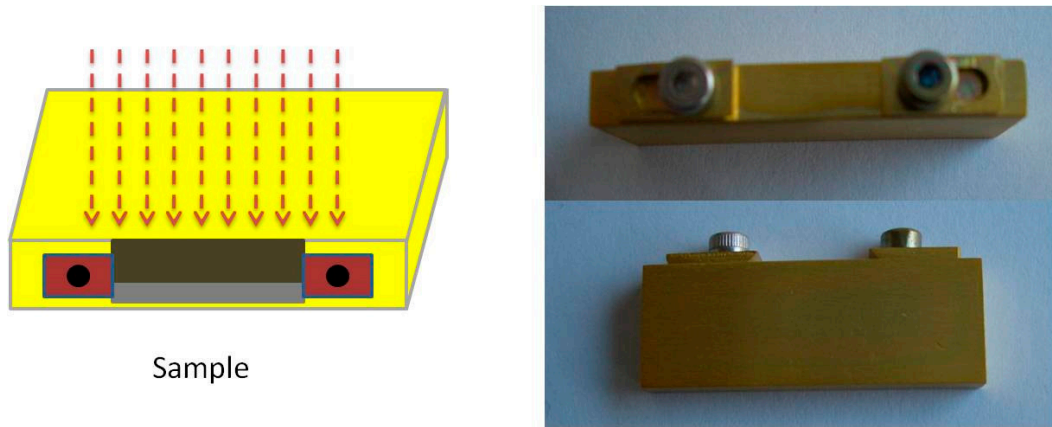


Figure 3.5 Left: Illustration of the sample holder for Si_3N_4 coating in PECVD. The sample is carefully oriented with its top surface (the side with PhC devices) facing the holder surface. The gas flow comes from the top towards the sample facet. Right: Side view and top view images of the sample holder. The dimension of the holder is $35 \times 15 \times 6 \text{ mm}^3$.

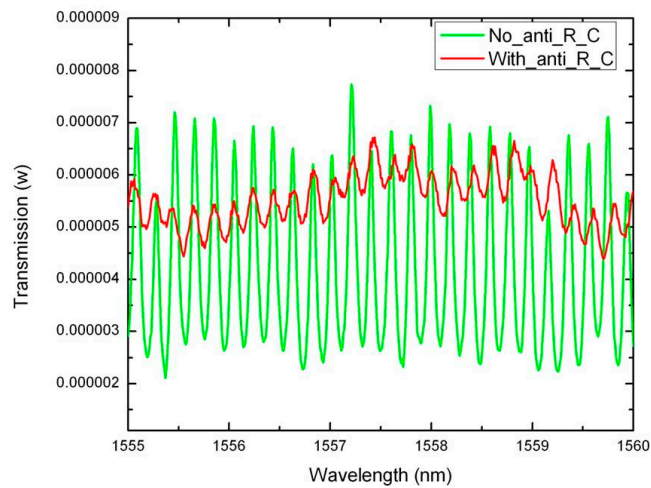


Figure 3.6 Transmission spectrum of a $3 \mu\text{m}$ width silicon ridge waveguide. Spectrum of the same device measured before and after anti-reflection coating are in green and red, respectively. Input power is 1 mW at the Tunics and scanning wavelength step is 10 pm.

	Sample 1	Sample 2	Sample 3
R (before coating)	27.51%	29.45%	26.45%
R (after coating)	4.33%	3.75%	3.57%

Table 3.1 Reflectivity for three different silicon ridge waveguides before and after the 200 nm Si_3N_4 layer coating.

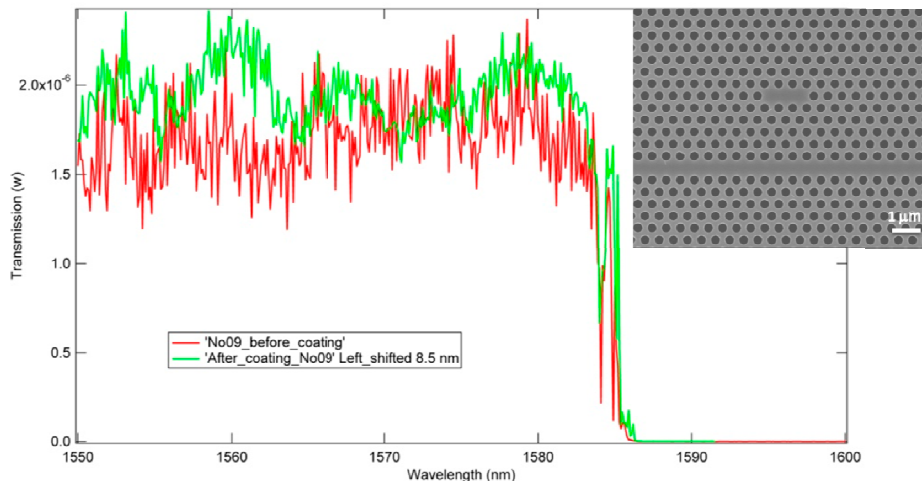


Figure 3.7 Transmission spectrum of a W1 waveguide with a single side-coupled L3 cavity. Spectrum of the same device measured before and after (blue shifted by 8.5 nm for better comparison) the anti-reflection coating are in red and green, respectively. Input power is 1 mW and scanning step is 50 pm. Inset: SEM image of the measured device, $a=440$ nm, $d=270$ nm.

Transmission spectrum of a 3 μm wide silicon ridge waveguide is measured before and after the anti-reflection coating in order to optimize the parameters of this Si_3N_4 layer. As shown in Fig. 3.6, the amplitude of Fabry-Perot oscillations is significantly reduced after the coating. As recorded in Table 3.1, the reflectivity at the facets is decreased from more than 25% to less than 4.5% after the coating process. Furthermore, concerning the effect of the device with the PhC structures, transmission spectrum of a W1 waveguide with a side coupled L3 cavity is measured before and after the anti-reflection coating (as shown in Fig 3.7). A decrease in the amplitude of the Fabry-Perot oscillations before the photonic band edge is observed. However, the deposition of Si_3N_4 on the surface of the device combined with the heating of the sample up to 300 $^\circ\text{C}$ during the process leads to a red shift of 8.5 nm in the spectrum. This red shift is a major disadvantage of the Si_3N_4 anti-reflection coating and needs to be overcome.

3.1.2 TiO_2 anti-reflection coating

In the previous section, Fabry-Perot oscillations are decreased with the application of a 200 nm Si_3N_4 anti-reflection layer on both the facets of the device. There are several drawbacks for this process. It is seen from the experimental results that the thicknesses at the center and at the edge of the substrates to be coated with PECVD are observed to be non-uniform. The thickness, which is very important in our case, is that of the layer on top of the 220 nm thick Si layer. This thickness is neither convenient to be characterized nor can be fully controlled. Therefore, the measurement results are slightly different from one deposition to another. In addition, the deposition in PECVD is almost non-directional. This is the main reason for undesired deposition of Si_3N_4 on the sample's surface. These

undesired depositions are most likely responsible for the 8.5 nm red shift, which is observed in Fig 3.7. One of the solutions to improve the process is the use of an e-beam evaporator (as shown in Fig 2.16). TiO_2 is selected instead of Si_3N_4 as the coating material because of the material refractive index and availability.

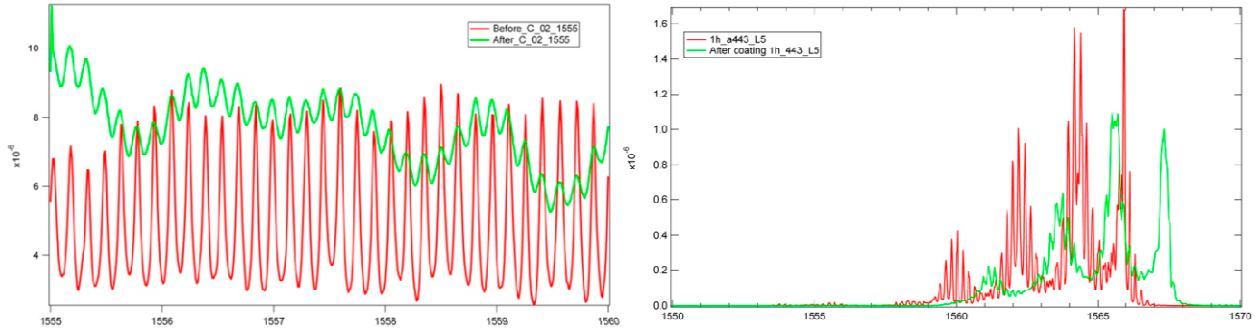


Figure 3.8 Left: Transmission spectrum of a 3 μm wide silicon ridge waveguide. Right: Transmission spectrum of a 5 L3 CCW. Spectrum of the same device measured before and after the 170 nm TiO_2 layer anti-reflection coating are shown in red and green, respectively. Input power is 1 mW at the Tunics and the scanning wavelength step is 10 pm. $a=441$ nm, $d=270$ nm, barrier is one standard air hole.

In the case of the e-beam evaporator used in the TiO_2 coating, Ti_3O_5 is used as the source material. The measured refractive index of TiO_2 at 1.55 μm is 2.07. The thickness of the coating layer defined by equation 3.2 is 170 nm. The high voltage is 5 kV and evaporation rate is 18 nm/min. The distance from the source to the sample is 1010 mm. The dispersion angle for a 15 mm long sample is 0.02 degrees, which corresponds to the e-beam evaporation being highly directional. As shown in Fig. 3.8, the amplitude of the Fabry-Perot oscillations is significantly reduced after the coating. The reflectivity of the facet is decreased from more than 20% to less than 3% after the coating process. In case of the device with PhC structures, transmission spectrum of a 5 L3 CCW is measured before and after the anti-reflection coating (as shown in Fig 3.8). The decreasing of the amplitude of Fabry-Perot oscillations is observed. Moreover, the high directionality of the coating process ensures a minimal deposition of coating material on the sample surface. Consequently, a red shift of less than 1.5 nm in the spectrum is observed before and after the coating process. This is significantly smaller than the 8.5 nm shift observed with the previous Si_3N_4 layer. A well controlled coating layer thickness and a minimal red shift of the spectrum after the coating process are the two major improvements gained due to the use of the e-beam evaporator instead of the PECVD.

3.1.3 SU-8 anti-reflection coupler

The presence of huge coupling losses is a direct result of the small geometric overlap and poor impedance matching of the optical modes between the input fiber and silicon waveguide. The small cross-sectional area and the large effective refractive index of

the waveguide mode prohibit efficient direct coupling from the fiber to the ridge. In the previous sections, efforts have been focused on reducing the strong Fabry-Perot oscillations. A few solutions have been proposed and investigated for improving the poor impedance matching of the optical modes between the input fiber and silicon waveguide^{47, 53}. SU-8 optical modes couplers and refractive index tapers are amongst the best performing candidates to this problem.

PhC defect modes can be applied for optical sensing and optical trapping. The optical circuit with single-mode operation in the silicon ridge waveguide at wavelengths around $1.5 \mu\text{m}$ requires the thickness of the silicon slab to be below 300 nm (220 nm for our case) and the width of the ridge waveguide to be below 500 nm ⁷. The small cross-sectional area and the high effective refractive index of the waveguide mode prohibit efficient coupling between the fibers and the facets. SU-8 couplers with a cross-section equivalent to that of the fiber are introduced at the facet of the device to increase the coupling efficiency (Fig. 3.9). Afterwards, the light is coupled to an adiabatically tapered silicon waveguide with the desired cross-section dimensions. Consequently, a high coupling efficiency at the facets and reduced Fabry-Perot interferences between the two facets are achieved in the same time.

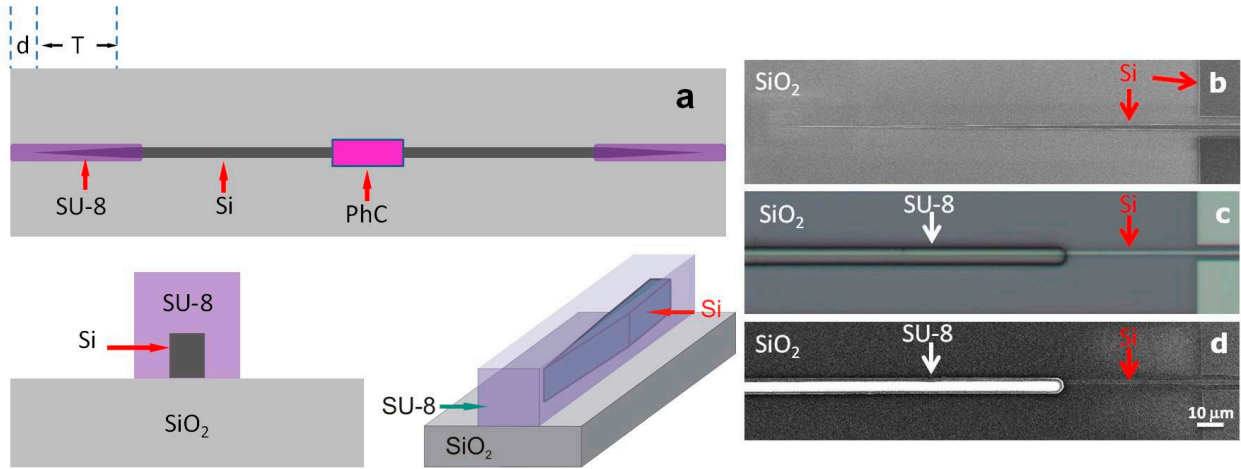


Fig. 3.9: a: Design of the SU-8 coupler (SU-8 in purple, SiO₂ in light grey, Si in dark grey), $d = 50 \mu\text{m}$, $T = 200 \mu\text{m}$. b: SEM image of the tapered waveguide. Microscope (c) and SEM (d) images of tapered waveguide with SU-8 coupler, respectively.

SU-8 coupler fabrication: SU-8 is one of the negative photo resists with a refractive index of 1.7 at $1.55 \mu\text{m}$. The fabrication steps for these SU-8 couplers fall in between the ICP dry etching and the photolithography steps in the standard PhC fabrication process (see section 2.1). SU-8 1040 is spin-coated onto the substrate surface for 30 seconds with 1500 rpm. The sample is allowed to cool in air for 5 minutes and is then soft baked at 90°C for 5 minutes. The patterns for the coupler are exposed with a Microtech MJB3 mask aligner for 12 seconds. The sample is then developed in MF319 for 120 seconds.

Afterwards, the sample is rinsed in water for 15 seconds to stop the development process. At last, the sample is dried by N_2 gas and baked at $115^\circ C$ for 15 minutes. The finished SU-8 couplers have a dimension of $4 \times 4 \mu m^2$.

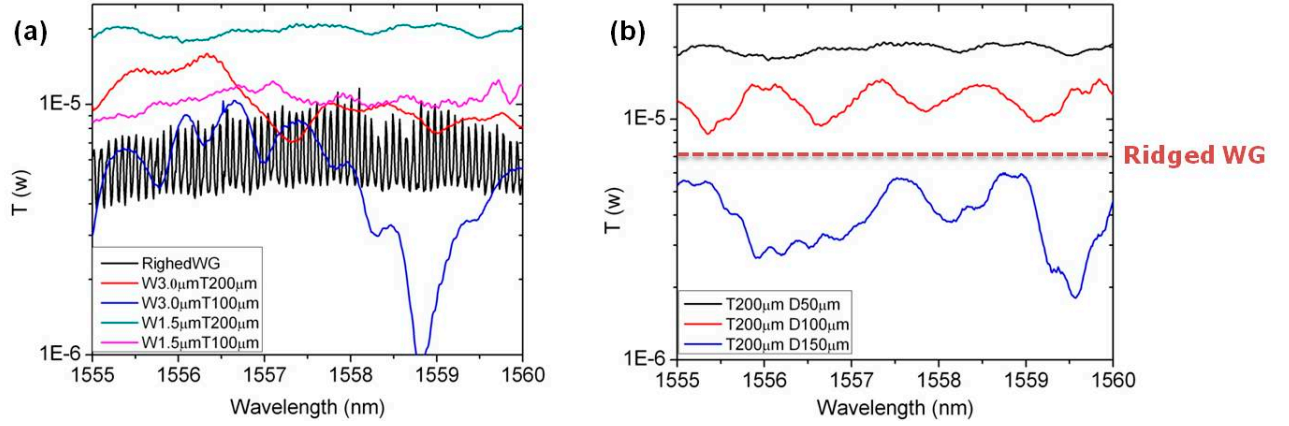


Fig. 3.10: (a) Transmission spectrum of a ridge waveguide (in black), $3.0 \mu m$ wide ridge waveguides with SU-8 couplers of 100 and $200 \mu m$ tapered parts, which are placed $50 \mu m$ from the facet (in blue and red) and $1.5 \mu m$ wide ridge waveguides with SU-8 couplers of 100 and $200 \mu m$ tapered parts, which are placed $50 \mu m$ from the facet (in purple and green)). (b) $1.5 \mu m$ wide ridge waveguide with a SU-8 coupler of $200 \mu m$ tapered part, which is placed 50, 100 and $200 \mu m$ from the facet (in black, red and blue). The approximate transmission power of the ridge waveguide is indicated with a dashed red line.

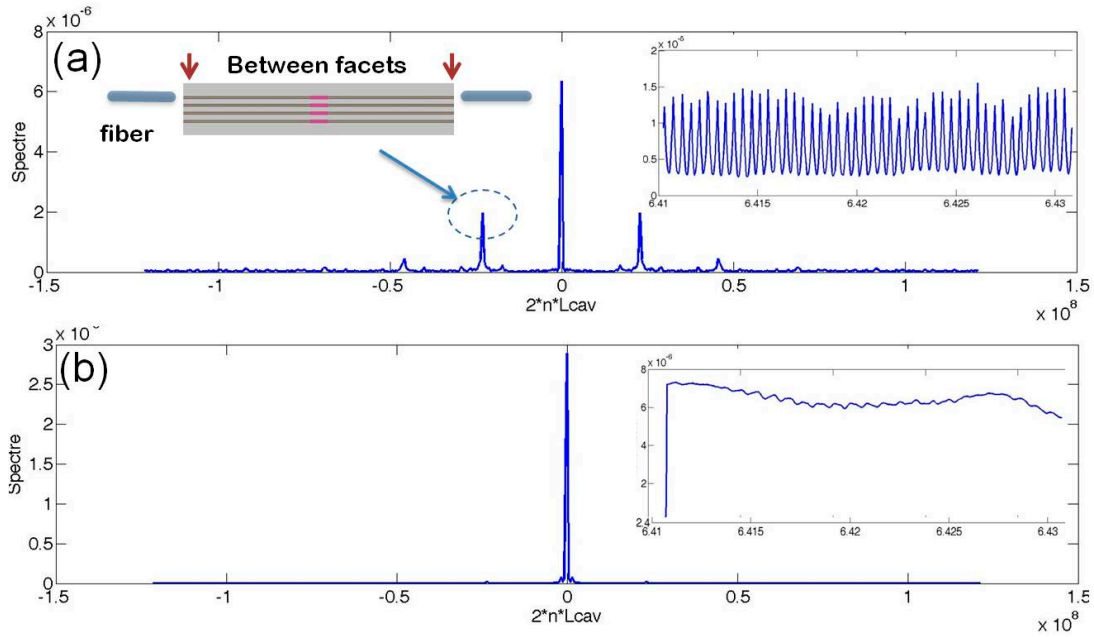


Fig. 3.11: (a) As shown in the Fourier transform of the transmission spectrum of a ridge waveguide, Fabry-Perot oscillations (peaks next to the center one) are due to the interference between two facets. Inset: transmission spectrum of a ridge waveguide. (b) Fourier transform of the transmission spectrum of a ridge waveguide with the SU-8 coupler (peaks due to the interference between two facets have disappeared). Inset: transmission spectrum of a ridge waveguide with the SU-8 coupler.

In order to optimize the parameters of the SU-8 coupler design, couplers are fabricated on tapered silicon waveguides, which have different widths, lengths of tapered parts and distance to the facet. As shown in Fig. 3.10, Si waveguides of $1.5\ \mu\text{m}$ width have a better optical performance than those of $3.0\ \mu\text{m}$ width. Meanwhile, the transmission power is proportional to the length of the tapered part and is inversely proportional to the distance from the facet. The optimized design is $1.5\ \mu\text{m}$ wide waveguide, which has a $200\ \mu\text{m}$ tapered part and is placed $50\ \mu\text{m}$ from the facet.

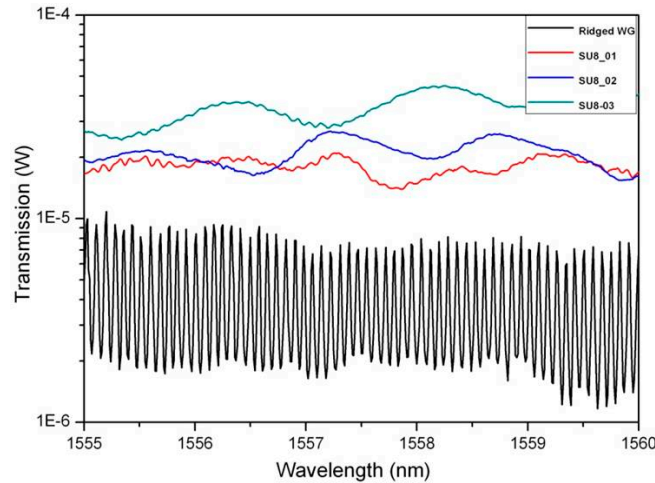


Fig. 3.12: Transmission spectrum of a ridge waveguide without coupler (in black) and three ridge waveguides with SU-8 couplers (in red, blue and green). The width of the ridge waveguide is $1.5\ \mu\text{m}$ and the cross section of the SU-8 coupler is $4\times 4\ \mu\text{m}$. The length of the tapered part is $200\ \mu\text{m}$ and is placed $50\ \mu\text{m}$ from the facet

In the case of Fabry-Perot fringes, the $200\ \mu\text{m}$ long tapered part brings a smoother refractive index change from SU-8 to silicon and successfully reduces the fringes significantly. Fourier transform of the transmission spectrum shows the vanishing of the peaks representing the Fabry-Perot interferences between the two facets (Fig 3.11). The reflectivity between two facets is reduced from more than 20% down to less than 1%. SU-8 couplers with a cross-section equivalent to that of the fiber increase the coupling efficiency. As shown in Fig 3.12, the measured transmission power through the ridge waveguide has increased from $6\ \mu\text{W}$ to $30\ \mu\text{W}$ (5 times).

In particular, for the coupling efficiency of the SU-8 coupler with the PhC structure, transmission spectra of ridged silicon waveguide and W1 waveguide with SU-8 coupler are measured (Fig. 3.13). After normalizing the spectra with respect to the fiber-to-fiber transmission spectrum, a 3 mm long silicon waveguide shows an insertion loss of 5 dB (2.5 dB/facet). The same device with a $100\ \mu\text{m}$ W1 waveguide has a total loss of 11 dB. A 30 dB drop of transmission power at the W1 photonic band edge is observed. Additionally, the transmission spectra of L3 cavities using two coupling schemes are measured (Fig. 3.14). Both these cavities are coupled with a W1 waveguide and SU-8 coupler. The features of the

L3 cavity mode can be easily obtained without Fabry-Perot oscillation fringes. This is very useful for the investigation of the optical properties of ultra-sensitive PhC cavities and their further applications.

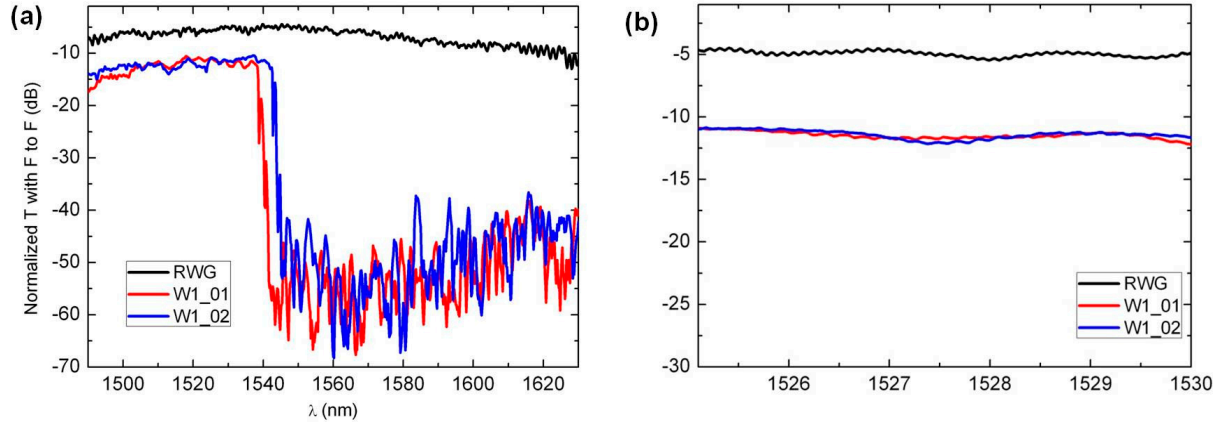


Fig. 3.13: (a) Transmission spectrum of a ridge waveguide (in black) and W1 waveguide with SU-8 coupler (in red, and blue). Normalized with fiber-to-fiber transmission spectrum. (b) Zoom in on (b) from 1525 nm to 1530 nm in wavelength.

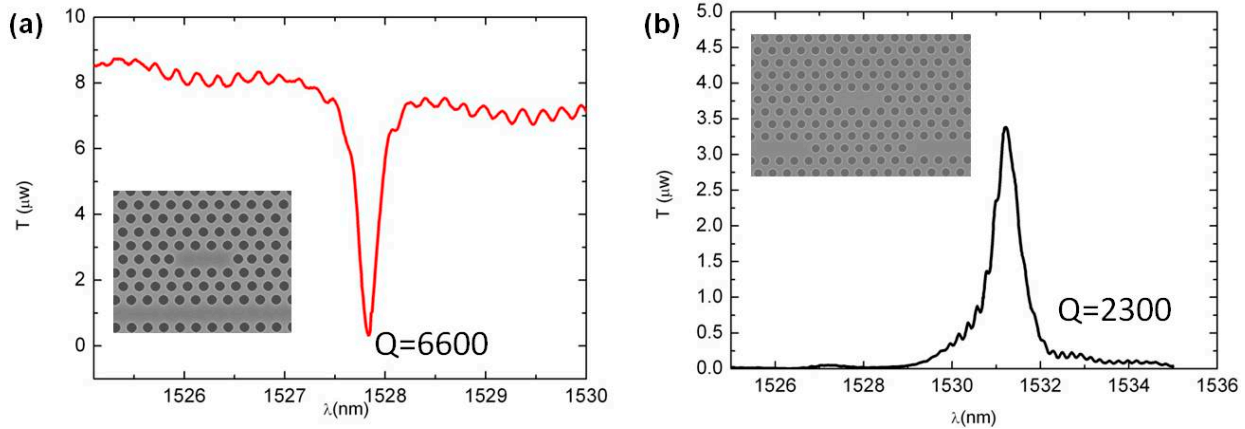


Fig. 3.14: (a) Transmission spectrum of a W1 waveguide with a side coupled L3 cavity (in red) with SU-8 coupler. The measured Q -factor is 6600. (b) Transmission spectrum of a Gamma-M coupled L3 cavity (in black) with SU-8 coupler. The measured Q -factor is 2300. Insets are SEM images of measured devices. $a=440$ nm, $d=270$ nm.

It can be observed from the results shown above that the transmission has increased in the ridge waveguide from 6 μ W to 30 μ W (5 times) and the reflectivity between two facets has decreased from 22% to 1% (Fig. 3.12). The length of tapered part is 200 μ m and the distance from the end of tapered waveguide to the facet is 50 μ m taking into account the high coupling efficiency and the ease of fabrication. This result also has been confirmed with PhC integrated devices. By improving the coupling efficiency and reflectivity, we can achieve better optical performance for our PhC devices for optical sensing and optical trapping.

3.2 Between waveguides and photonic crystal structures

Light coupled into a silicon waveguide will experience a group velocity difference when it enters the PhC structures. The efficient coupling of light into PhC defect modes has been a challenging topic. In PhCs, the slow light phenomenon is related to the multiple reflection and interference of Bloch modes within the periodic PhC lattice. This leads to the creation of flat photonic bands, which are characterized by group velocities that are considerably lower than that of the corresponding unstructured homogeneous medium. Slow light can provide the possibility to manipulate the speed of light and enhance both linear and non-linear light matter interaction from absorption to gain. In order to fully benefit from the slow light effect, it is important to efficiently couple in and out of the PhC waveguides. However, efficient coupling between a ridge waveguide and a slow light PhC waveguide is a challenging task. Due to the apparent mismatch in the group velocities between the fast light region of the ridge waveguide and the slow light region of the guided PhC waveguide mode, coupling becomes increasingly inefficient when approaching the slow light region, which limits the possibility of slow light in practical applications. Significant efforts have been directed to overcome the challenges due to this problem⁵⁴⁻⁶². One of the options is the use of the group velocity taper.

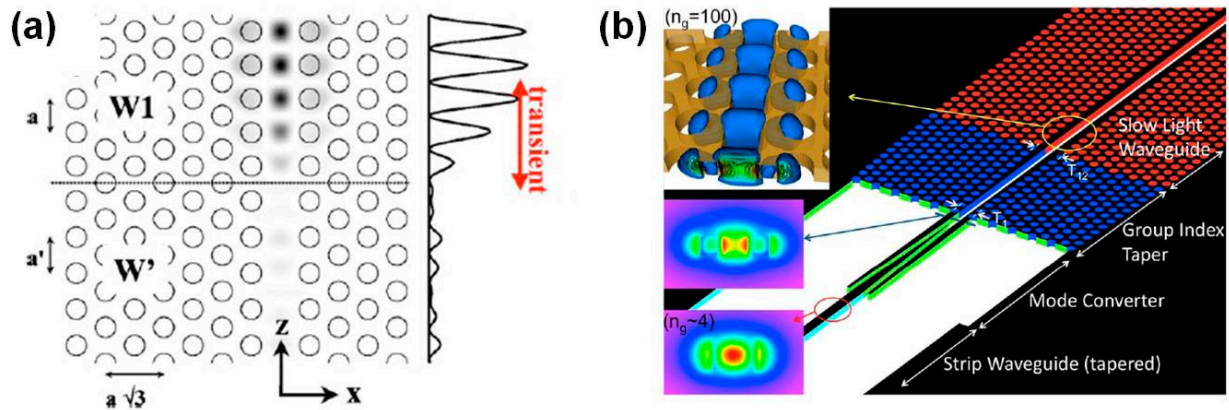


Fig. 3.15: (a) Interface between two PhC waveguide supporting slow (W1) and fast (W') Bloch modes at the same frequencies ($n_g = 100$)⁵⁴(reprinted from ref.55). (b) Schematic of the slow light slotted PhC waveguide, group index taper, mode converter, and strip waveguide (tapered). The insets show the mode profiles of a strip waveguide and a slow light slotted PCW at a high group index ($n_g = 100$)⁵⁵(reprinted from ref.55).

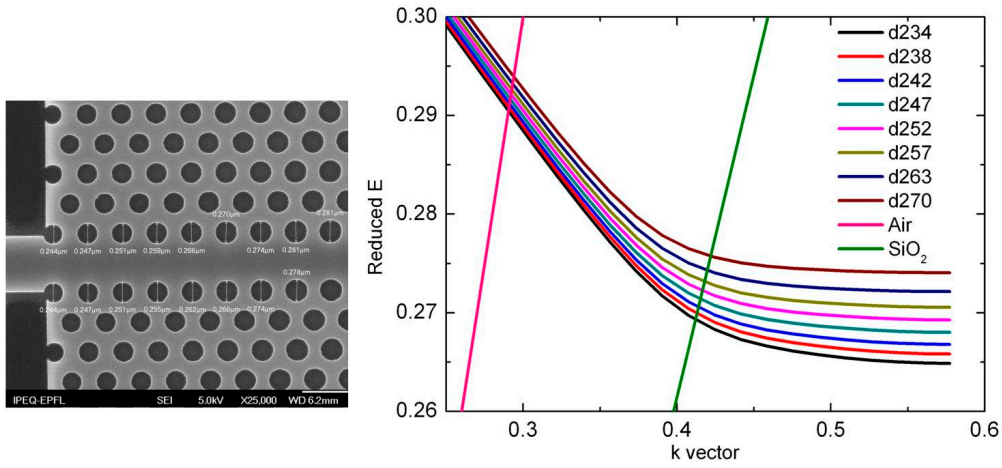


Fig. 3.16: PWE calculated W1 waveguide dispersion curves for $a = 440$ nm and $d = 234, 238, 242, 247, 252, 257, 263, 270$ nm. Inset is the SEM image of the fabricated sample.

Group velocity taper is used for coupling light from z -invariant ridge waveguides into slow Bloch modes of single-row defect PhC waveguides (Fig. 3.15a). High coupling efficiencies close to 96% are predicted with 2D computational results for taper lengths of only a few wavelengths. Furthermore, C. Y. Lin and coworkers experimentally demonstrated the highly efficient coupling into a slow light slotted PhC waveguide⁵⁵(Fig. 3.15b). With optical mode converters and group index tapers that provide for a good optical mode matching, a nearly flat transmission over the entire guided mode spectrum of 68.8 nm wavelength range with a minimum insertion loss of 2.4 dB was achieved. This design is highly interesting in order to design efficient and compact devices that benefit from the slow light enhancement without increasing the coupling loss to the devices.

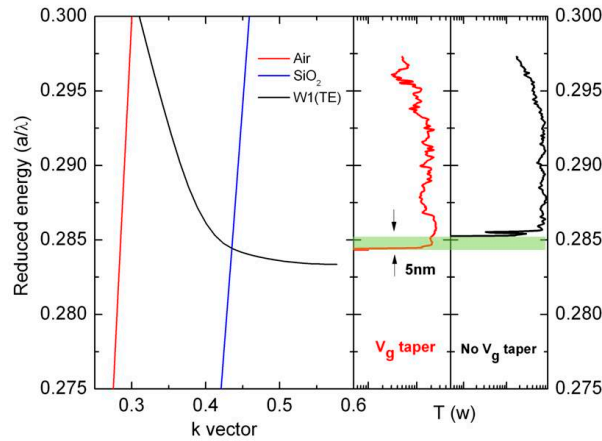


Fig. 3.17: Transmission spectrum of a W1 waveguide with (in black) and without (in red) the group velocity taper plotted along with PWE calculated W1 waveguide dispersion curve. Both devices have SU-8 couplers. The width of the ridge waveguide is $1.5 \mu\text{m}$ and the cross section of SU-8 coupler is $4 \times 4 \mu\text{m}$. The length of the tapered part is $200 \mu\text{m}$ and is placed $50 \mu\text{m}$ from the facet

As shown in Fig 3.16, the design is a standard W1 waveguide with lattice constant and air hole diameter of 440 nm and 270 nm, respectively. The choice of air hole diameters d_n ($n=1, 2, \dots, 8$) in order to create the group velocity taper is based on an empirical equation $d_n=144.15+8.19n-0.46n^2$, which can create a smooth transition of hole diameters within a very short distance as shown in Fig. 3.13b⁵⁶. The group velocity taper is composed of 8 rows of air holes with diameters of 234, 238, 242, 247, 252, 257, 263, 270 nm. By doing so, the group velocity is smoothly decreased from the fast light region to the slow light region. SEM of the fabricated device shows good quality in term of air hole shape and dimension. For a better comparison, transmission spectra of W1 waveguides with and without group velocity tapers are plotted along with PWE calculated dispersion curve. The W1 waveguide with the group velocity taper shows light transmission for an additional bandwidth of 5 nm in the slow light region compared to the one without the taper (as shown in Fig. 3.17).

Slow light in PhC waveguides can significantly enhance light-matter interactions, which are a promising goal for realizing advanced photonic devices such as tunable delay lines, highly-efficient modulators and slow light applications in sensing or trapping^{18,23}. It is important and challenging to efficiently couple in and out of the PhC waveguide operating close to the slow light regime. The apparent mismatch in the group velocities between the fast light in the strip waveguide and the slow light in the guided mode of PhC waveguide can be improved by using PhC tapers with gradually changing air hole diameters. This design is useful for other practical applications of slow light, which will be explained, in later chapters.

3.3 Inside photonic crystal structures

Inherent scattering losses inside PhC structures due to structural irregularities have been identified as a major obstacle that hinders their further exploration. These irregularities are introduced during the fabrication process. One of the key steps is e-beam lithography. In this section, investigation of the disorder effect introduced by different E-beam writing resolutions will be discussed.

In two-dimensional PhCs, light propagates in the slow light regime near the band gap. The propagation of light will be strongly perturbed by residual structural disorder. In order to investigate this effect, planar PhCs are fabricated with different E-beam writing resolutions to introduce artificial disorder. As shown in Fig. 3.18 a, b, coupled cavity waveguide⁶³ structures are fabricated with 3 different E-beam writing resolutions, which are 1.25, 2.5 and 5.0 nm respectively. Two types of disorder can be introduced in this process namely, hole-size disorder and hole-position disorder (Fig. 3.18 c).

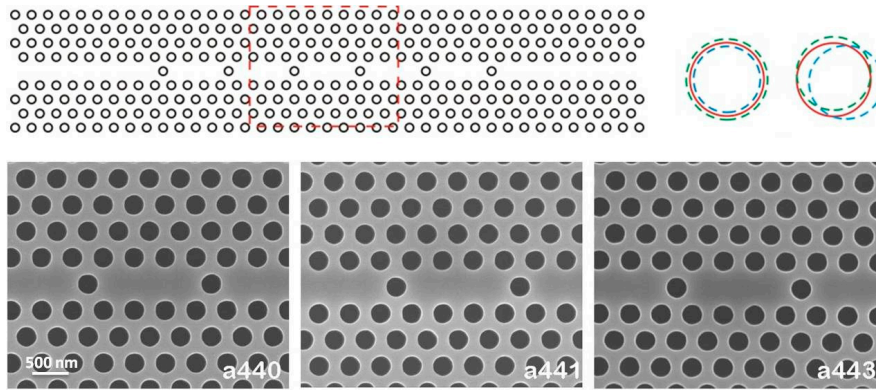


Figure 3.18 (a) design of inline 5 L3 coupled cavity waveguide $a=440$ nm, $d=270$ nm. (b) SEM images of three fabricated samples ($a=440, 441, 443$ nm) with different E-beam writing resolutions (1.25, 2.5, 5.0 nm) (c) size and location disorder (design in red, fabricated in blue and green).

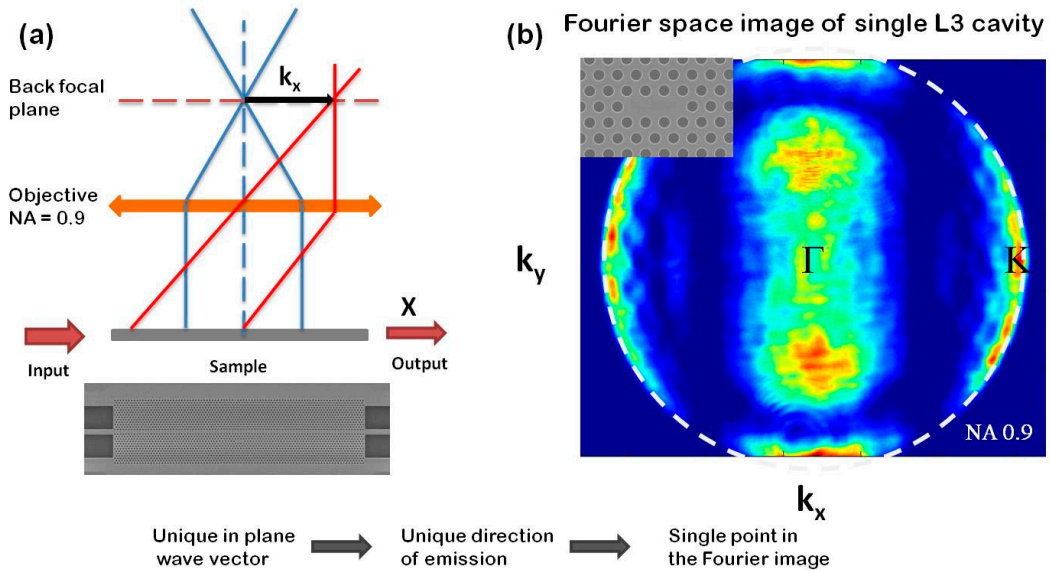


Figure 3.19 (a) Schematic of the working principle of the Fourier setup (b) Fourier space image of a single L3 cavity (Inset is the SEM image of the L3 cavity)

In the proximity of the band edge, an ideal band evolves toward a singular point and the speed of the corresponding waves slow down to a complete stop. Such a behavior at the band edge is particularly appealing for light waves in order to delay light propagation or to enhance nonlinear interaction with matter. Two major effects in real photonic structures affect this ideal behavior: the intrinsic out-of-plane losses and the residual structural disorder. The dispersion curve of the PhCs can be engineered in order to be entirely located below the light cone over a wide frequency range. Thus, the intrinsic out-of-plane losses are zero and only the residual disorder is left. Light propagation through a coupled cavity waveguide structure has attracted significant interest in our research group. For such structures, the intrinsic out-of-plane losses and the residual structural disorder can both affect the light propagation. With our Fourier space imaging setup (as show in Fig 3.19) ⁶⁴,

we can obtain the real space image and the dispersion diagrams of the coupled cavity waveguide structures (Fig. 3.20). Due to the local disorder introduced by the E-beam resolution and the out-of-plane losses, the coupled cavity waveguide mode dispersion curves (Fig.3.21) broaden around the Γ point ($k=0$). However, we did not observe a similar effect around K point. The out-of-plane losses are lower than that of the Γ point and the residual disorder is not strong enough to be observed. The limitation of the processing technique could be a possible reason.

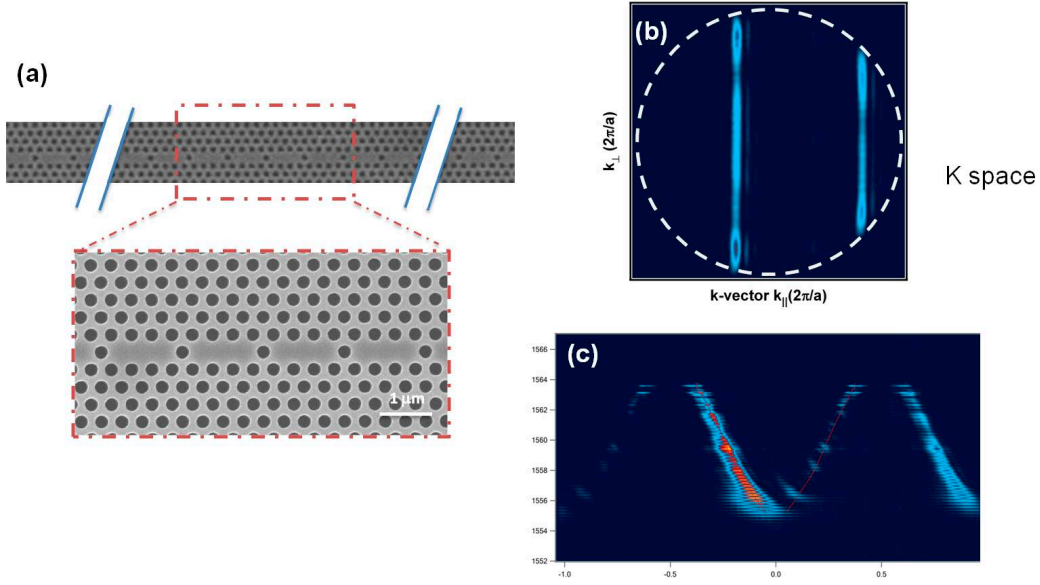


Figure 3.20 (a) SEM images of outline 50 L3 coupled cavity waveguide (CCW) ($a = 443\text{nm}$, $d = 282\text{ nm}$). (b) Fourier space image of 50 L3 CCW operating above the light line. (c) Reconstruction of the CCW mode dispersion curve in K space by scanning different wavelengths.

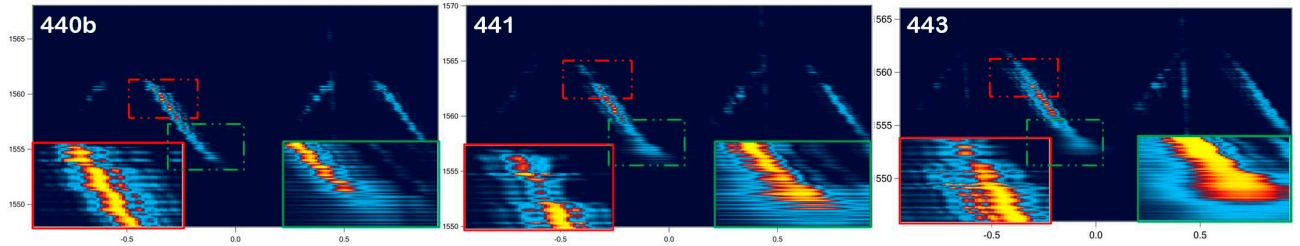


Figure 3.21 Mode dispersion in K space of inline 50 L3 coupled cavity waveguides, from left: $a = 440, 441$ and 443 nm .

In conclusion, different approaches are experimentally investigated to improve the coupling efficiency into PhC devices, especially for the slow light enhancement applications. At the facet of the device, anti-reflection coating layers (Si_3N_4 or TiO_2) and SU-8 couplers are discussed. A thin layer of TiO_2 coated by e-beam evaporation on the facets can successfully decrease the reflectivity down to 3%. Furthermore, SU-8 couplers can achieve both lower than 1% reflectivity and higher than 5 times transmission power. PhC tapers

with gradually changed air hole diameters are used to overcome the mismatch in the group velocities between the fast light in the strip waveguide and the slow light in the PhC waveguide mode. Most of approaches discussed in this chapter are based on the integration of previous demonstrations into our designs. However, it is important to combine different approaches to find the optimized design for the applications in this thesis. These SU-8 couplers and PhC group index tapers are useful in applications of PhC structures in refractive index sensing and optical trapping, which will be elaborated in the later chapters of this thesis.

Chapter 4

Applications in refractive index sensing

The dispersion and propagation properties of two-dimensional PhC devices have been investigated with various experimental demonstrations ^{40, 64, 65}. These properties can be used in a variety of applications involving light-matter interactions. Refractive index (RI) sensing is one such application that makes use of the optical confinement of the defect mode in PhC devices. Defect modes can be introduced inside the photonic band gap by appropriate design of cavities. Such cavities allow for a strong optical field confinement, leading to a dramatic enhancement of both the optical intensity and the light matter interaction. Since the spectral position of the cavity resonance is highly sensitive to the RI changes in the local environment, it can be used as a sensor to detect the presence or absence of the target molecules. This feature opens the door to a wealth of applications in the field of integrated optical sensors, especially towards applications in the life sciences.

PhC biosensors form a novel type of optical bio-sensing platform, which has been presented in the recent literature ⁶⁶⁻⁷². Integrated 2D PhC cavities fabricated with the low cost SOI platform owing to their high Q factors and small mode volumes are ideal candidates for refractive index sensing for biological applications. However, in widely used PhC cavities, the strong light-matter interaction is possible only within the high index material wherein the maximum of the confined optical field is located. This is not very favorable for precision refractive index sensing ^{16, 17}, as the analyte is present in the low index medium. Enhancement of the field overlap between the optical mode and the cladding medium would be beneficial for refractive index sensing applications, as it would increase the device sensitivity and/or lead to the reduction of the necessary amount of analyte. An air-slot cavity is investigated based on this principle. This PhC cavity with a sub-hundred nanometer-wide air slot is designed as the cavity defect region. Due to a large electric field discontinuity at the slot boundaries ²⁴, such a cavity confines TE polarized modes in the slot allowing for a large interaction of the optical field with the low-index medium.

J. Jágerská performed the necessary simulations and the refractive index gas sensing experiments. H. Zhang and I fabricated the PhC devices. This project being the first experiment in which I was involved in the beginning of my PhD, I would like to present these experimental results concerning the applications aspect of my thesis work.

4.1 Applications of photonic crystals in refractive index sensing

There have been quite a few demonstrations utilizing PhCs in sensing applications²²⁻²⁶. One of the leading approaches is the use of a 2D PhC cavity. In the work of Lee *et al.*⁷³, they demonstrated an ultrasensitive two-dimensional PhC micro-cavity biosensor (Fig. 4.1). The device was fabricated on a silicon-on-insulator wafer and has its resonance at 1.58 μm . Coating the surface of the device with proteins of different concentrations resulted in a unique resonance red shift. The presented device was shown to detect a molecular monolayer with a total mass as small as 2.5 fg. The device performance was also verified by measuring the red shift corresponding to the binding of Glutaraldehyde and Bovine Serum Albumin (BSA). The experimental results were in good agreement with theoretical computations and with ellipsometric measurements performed on a flat oxidized silicon wafer surface.

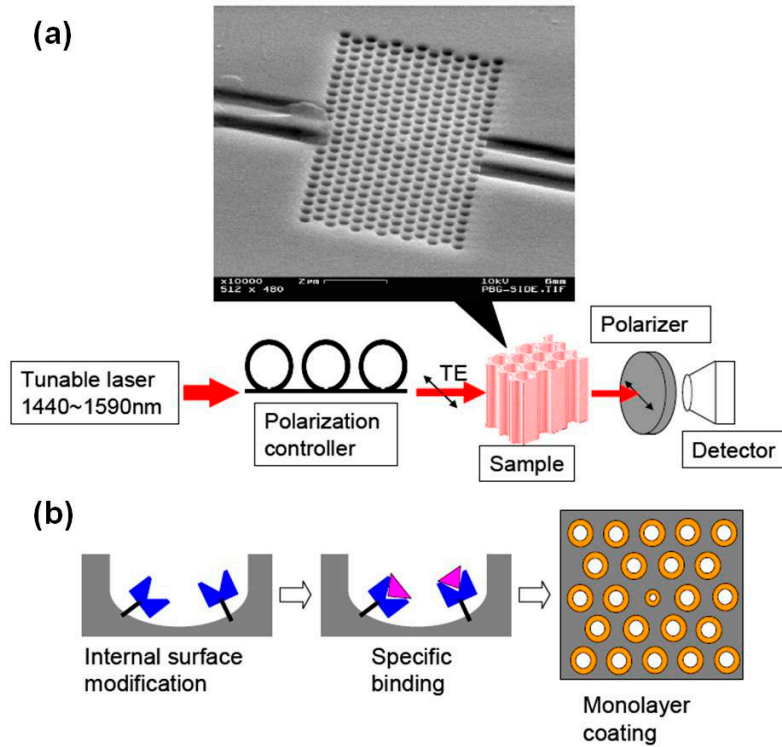


Figure 4.1 (a) SEM image of the sensing PhC device and the schematic of the associated experimental setup. A tunable laser (1440 nm to 1590 nm) was used as the light source. The optical signal was coupled in and out of the PhC using tapered ridge waveguides. An InGaAs detector was used to measure the transmission signal. (b) Schematic of bio-molecule recognition: the probe molecules selectively capture the target molecules. The bio-molecules form a uniform layer on the internal surface of the sensor. In reality the layer thickness is very small compared with the pore size⁷³ (reprinted from ref.73)

4.2 Air slot waveguide and air slot cavity

In most of the cases, the major proportion of the cavity mode energy is confined inside the medium with high dielectric constant such as Silicon. This strongly limits the sensitivity of the sensing application. In contrast to this, the air slot PhC cavity has a large percentage of the cavity mode confined inside the air slot. This cavity mode is highly sensitive to the refractive index changes in the cladding layer. Therefore, air slot PhC cavity is highly interesting for refractive index and biosensing applications. We develop a new type of silicon air-slot PhC cavity for optical refractive index sensing. This cavity has an experimentally measured high quality factor of up to $Q \sim 2 \times 10^4$. Due to the strong overlap of the cavity mode with the detection volume, we are able to achieve an impressive experimental sensitivity of 590 nm/RIU and a detection limit below 1×10^{-5} RIU.

The air slot PhC cavity was inspired by the air slot waveguide (as shown in Fig. 4.2). The first air slot waveguide was theoretically proposed and experimentally demonstrated by Lipson *et al.* in 2004²⁴. They presented a novel waveguide design for enhancing and confining light in a nanometer-wide low-index material. Light enhancement and confinement is caused by the large discontinuity of the electric field at high-index-contrast interfaces. They showed that by use of such a structure the field could be confined within a 50 nm wide low-index region with ultra-high intensities. They also fabricated ring resonators based on the structure and showed that the structure could be implemented in highly integrated photonic platforms.

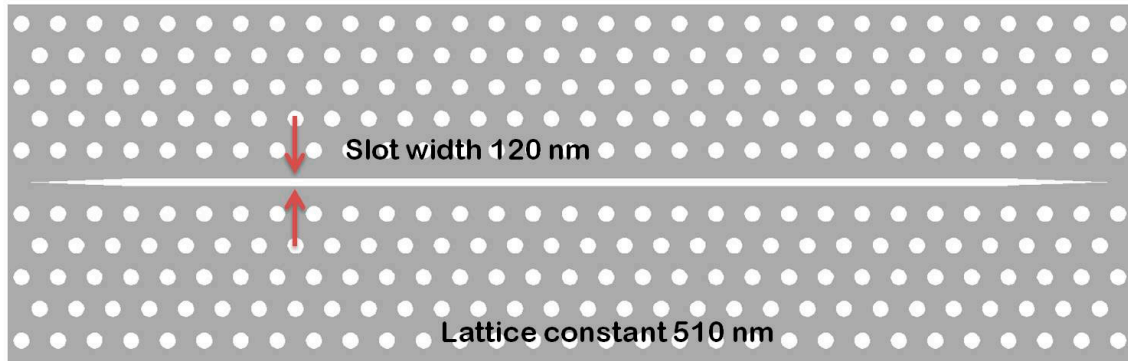


Figure 4.2 Schematic drawing of a PhC slot waveguide. The slot width is 120 nm. Lattice constant is 510 nm. Filling factor is 40%.

When an air slot is opened inside the W1 defect region, the original line defect modes are shifted to higher optical frequencies as a result of increasing overlap of their field with the air (as shown in Fig 4.3). The even W1 mode, which is strongly confined within the line-defect region, is shifted rapidly towards the air band, while the odd W1 mode is only marginally affected due to a rather weak mode profile overlap with the air-

slot. In addition, a new waveguide mode denoted as slot-waveguide mode (SW1) is lifted up from the dielectric band, shifting its cut-off to higher frequencies as the width of the slit increases. It is characterized by even symmetry, positive slope of the dispersion curve and strong spatial overlap of the optical field with the air Γ :

$$\Gamma = \frac{\int_a |E(r)|^2 d^3r}{\int_{a+d} |E(r)|^2 d^3r}, \quad (4.1)$$

where a stands for the air and d for the dielectric. In the case of a 120 nm wide slot, the spatial overlap of the SW1 mode with the air is as high as 92%.

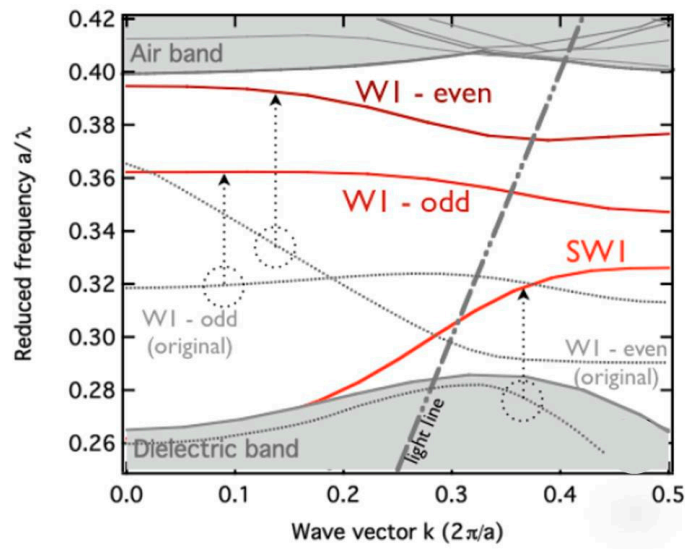


Figure 4.3 Dispersion diagram of a W1-based slot waveguide with $a = 510$ nm and slot width of 120 nm, showing the slot waveguide mode (SW1), the original W1-odd and W1-even mode ⁷⁴(reprinted from ref. 74).

The air-slot cavity was proposed for the first time in a 1D PhC by Robinson *et al.* ⁷⁵, followed by several different designs in PhC slabs ^{76,77}. However, the full potential of such structures for highly sensitive on-chip sensing applications has not yet been clearly assessed. Here, a PhC air-slot cavity is investigated. In order to create a cavity, one can either modify the properties of the PhC mirror, or the dimensions of the slot itself. The first approach was adopted by J.T. Robinson *et al.* ⁷⁵, where the lattice constant of the PhC is locally reduced to create a heterostructure cavity, as well as in the works of Yamamoto *et al.* ⁷⁷ and Gao *et al.* ⁷⁸, where the holes adjacent to the slot were transversally shifted to define a width-modulated line-defect cavity.

Fig. 4.4a shows the fabricated air-slot PhC cavity, which is based on a W1 waveguide with an air-slot embedded in the line defect region (fabrication details in section 2.1). In our design, the PhC lattice is kept unchanged, but the width of the air slot is locally reduced by 20 nm to delimit the volume of the cavity (insert of Fig. 4.4a). Reduced slot width results

in formation of reflective barriers for the cavity mode, as it can be inferred from the dispersion diagram of a slot PhC waveguide shown in Fig. 4.4b). The theoretical dispersion was calculated and assumes a PhC with a lattice constant $a = 510$ nm, filling factor $f = 0.4$ and the width of the line defect region corresponding to one omitted row of holes (W1 waveguide). When opening an air-slot inside the W1 defect region, the TE-polarized slot waveguide mode is pulled up from the dielectric band, shifting the mode cut-off to higher frequencies as the width of the slit increases. Consequently, the cut-off of the 120-nm slot waveguide mode (plotted in Fig. 4.4b) lies at slightly higher frequencies than the cut-off of the 100-nm wide one, and hence, the former can support a defect state when sandwiched between two 100-nm wide slot waveguide sections.

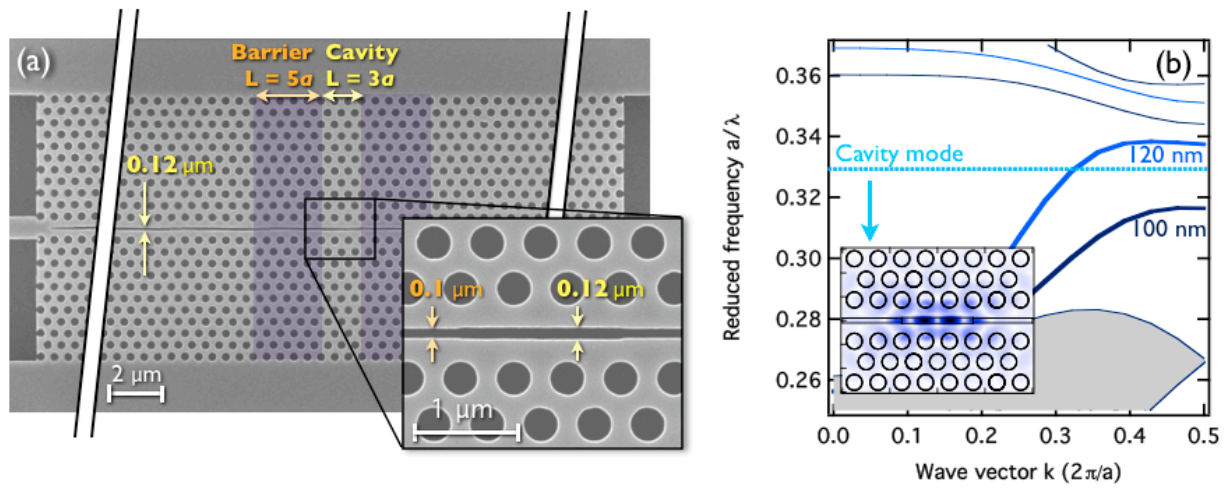


Figure 4.4 (a) Scanning Electron Microscopy (SEM) image of the air-slot cavity. Barrier regions are highlighted by false color. (b) Dispersion curves of 100 and 120 nm wide PhC slot waveguides and the air-slot cavity mode calculated by Guided Mode Expansion method. Inset: Electric field distribution $|E_{xy}|$ of the cavity mode

4.3 Highly sensitive gas detection with air-slot photonic crystal nanocavity

* The main results in this section are originally published in “Refractive index sensing with an air-slot PhC nanocavity” *Opt Lett* **35**, 2523-2525 (2010)¹⁸.

The fabricated devices were characterized using a setup combining the end-fire and imaging techniques, as shown in Fig. 4.5a. More details about the far-field imaging technique and the direct imaging of the cavity modes can be found in chapter 3 and other references^{10,11}. Fig. 4.5b shows the recorded transmission spectrum for an air-slot cavity with the same parameters as previously specified for the theoretical calculations. We can identify a narrow transmission peak that corresponds to the resonance mode of the air-slot cavity. A broad and weak resonance observed between the cut-off at 1580 nm is attributed to an evanescent mode, which can penetrate through the barriers due to evanescent

tunneling. The proper cavity mode can be identified with far-field imaging, even if the transmitted signal is extremely weak or accompanied with spurious Fabry-Perot resonances that often appear as peaks in our case. As shown in the inset in Fig. 4.5b the far-field radiation pattern of the cavity mode has a stable, highly symmetric pattern determined only by geometrical properties of the cavity. It differs distinctly from the angular emission spectrum of residual resonance peaks. The evanescent mode creates a speckle pattern that changes with excitation wavelength.

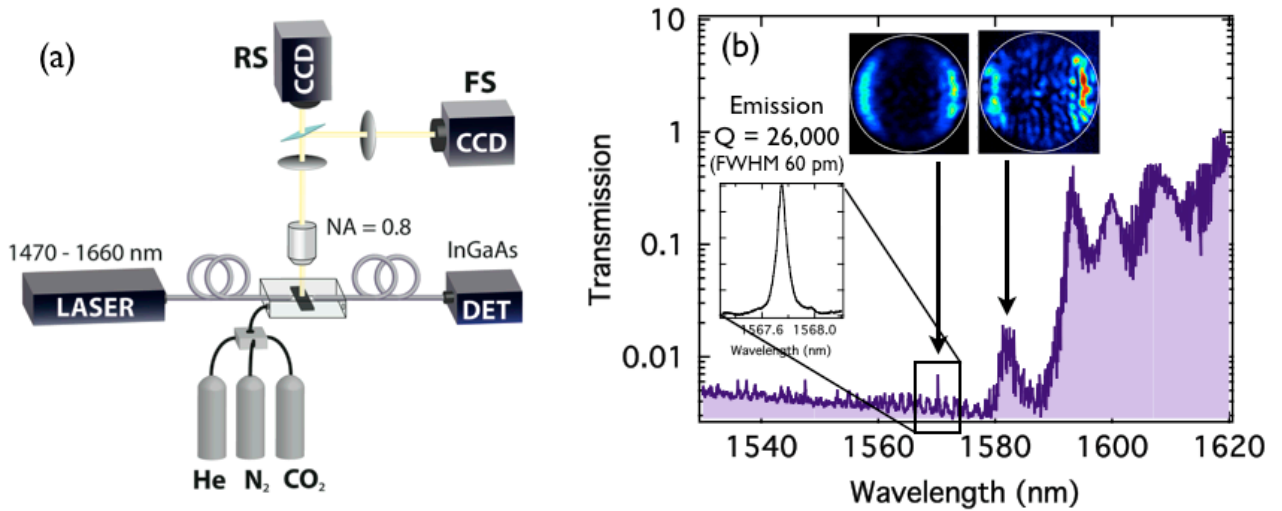


Figure 4.5: (a) Schematic drawing of the combined endfire imaging setup. (b) Transmission spectrum of the air-slot cavity and the far-field images of both the cavity mode and a spurious evanescent mode resonance. Inset shows the experimental emission spectrum of the cavity.

Knowing the mode field overlap Γ (in equation 4.1, 0.83 in this experiment), the first-order perturbation theory can be used to estimate the sensitivity S of the device to the refractive index change Δn inside the slot^{79, 80}

$$S = \frac{\Delta\lambda}{\Delta n} = \Gamma \frac{\lambda}{n_{\text{eff}}}, \quad (4.2)$$

where λ is the resonance wavelength of the cavity and $n_{\text{eff}}^2 = \Gamma n_{\text{gas}}^2 + (1 - \Gamma)n_{\text{Si}}^2$ is the effective index experienced by the cavity mode. For resonance frequency $\lambda = 1570$ nm, $n_{\text{gas}} = 1$, and $n_{\text{Si}} = 3.47$, we get a sensitivity of $S = 770$ nm per refractive index unit (RIU), which is quite remarkable for a sensor with an active sensing volume as low as $0.04 \mu\text{m}^3 = 40$ attoliters.

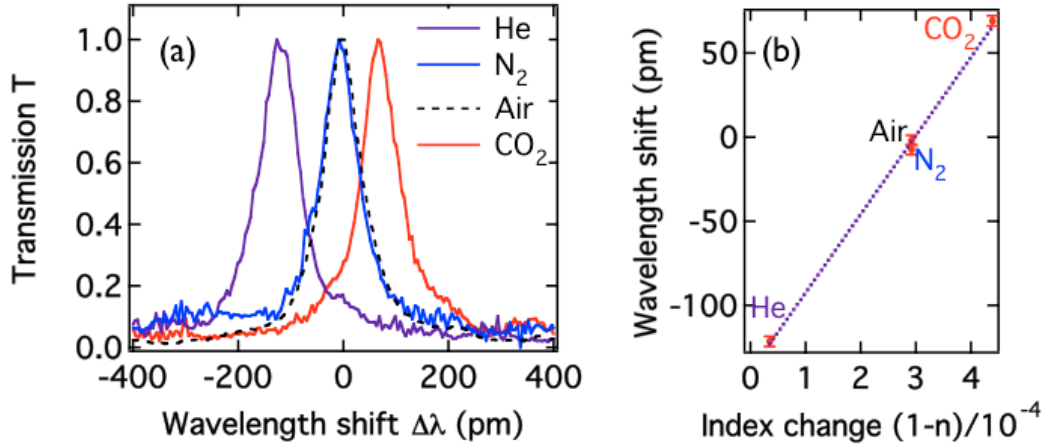


Figure 4.6: (a) Spectral position of the cavity resonance upon exposure to helium, nitrogen and carbon dioxide. Reference peak measured for the air is shown as a dashed line. (b) Wavelength shift of the cavity resonance plotted as a function of the refractive index change of the respective gas. The marker size corresponds to the error bar of ± 3 pm.

The shift of the air-slot cavity resonance in response to the change of the gas refractive index is shown in Fig. 4.6. If we consider the air as the reference medium, we can observe both negative shift of the resonance peak position for helium and shift to higher optical wavelengths for carbon dioxide that exhibits the highest refraction. As plotted in Fig. 4.6b, the dependence of the wavelength shift on the refractive index change is strictly linear and the interpolation of the measured values yields the experimental sensitivity $\Delta\lambda/\Delta n = 590$ nm/RIU, which is in a good agreement with the theoretical value of 570 nm/RIU. Repetitive measurements on a longer time scale show that the peak position can be retrieved with a precision of ± 3 pm, which implies the detection limit (DL, ratio of the resolution and the sensitivity) of the device of 1×10^{-5} RIU. Nevertheless, it should be mentioned that along with the refractive index of the surrounding medium, there are other parameters that can induce a shift of the resonance frequency of the air-slot cavity mode, e.g., temperature, humidity adsorbed at the structure sidewalls, or progressive oxidation of the sample surface. In particular, the latter turns out to be the most detrimental, as it can induce a shift of the resonance peak by as much as 45 pm per hour. This effect can be eliminated when working with O₂-free gases, or compensated using an identical reference structure. Further enhancement of the sensor detection limit can be achieved by increasing the Q factor of the cavity, which improves the precision of the resonance frequency readout. However, note that the 40 attoliters sensing volume holds as little as 1×10^6 molecules;

In conclusion, a highly sensitive refractive index detection scheme with a PhC air-slot cavity is presented. Because of a strong overlap of the cavity mode with the surrounding medium, such a cavity can achieve an experimental sensitivity of 510 nm/RIU with the detection limit higher than 1×10^{-5} RIU, which is comparable with state-of-the-

art devices ¹⁶. Nevertheless, the major advantage of the sensor is an extremely small active sensing volume of 40 aliters, which is made possible due to the strong confinement of the optical field in PhC point-defect cavities. Such a small volume not only allows one to drastically decrease the necessary amount of analyte, but it also makes the sensor suitable for high-density integration oriented toward parallel or multiplex detection.

Chapter 5

Applications in optical trapping and back action

Optical tweezers as demonstrated by Ashkin and Dziedzic ^{81,82}, have been widely applied in a variety of physical and biological studies. It is highly important to extend the features of these free space tweezers into an integrated platform owing to two major reasons. Firstly, they are pursued for the aspect of miniaturization to replicate the current functionalities on a single chip and minimizing the need for bulk optics. Secondly, to overcome the Abbe's diffraction limit that prevents the trapping of smaller sized particles such as proteins and viruses.

Near field optical trapping can be summarized in two groups in terms of non-plasmonic platforms. One of them is the evanescent field trapping in a silicon-core waveguide. In the case of slot waveguides, when a particle comes in contact with the optically excited waveguide it might be captured in the propagating field and begins to move in the direction of optical propagation. In contrast to the traditional localized optical traps, such waveguide based trapping schemes allow for only the propulsion of the particles along a line, which limits their potential applications. The other group involving non-plasmonic platforms is that of optical resonator trapping. The inherent nature of light to concentrate in the high refractive index medium results in the fact that the trapped particle interacts only with a limited fraction of the resonant optical field. As a consequence, trapping powers required for demonstrating trapping are relatively high.

Resonant optical trapping is highly interesting not only for manipulating small particles but also for understanding the optomechanical interaction between cavities and sub-wavelength sized objects. Recent experiments have widely studied the coupling between a resonant optical field and single atoms ^{83,84} or micromechanical resonators ^{85,86}. However, the interaction between the mechanics of a large isolated nanoscale particle and a high finesse optical cavity, though theoretically predicted ⁸⁷⁻⁹⁰, is yet to be demonstrated. Quantitative investigation of this optomechanical interaction requires the use of cavities with high quality factors (Q) and large field gradients. In this context, it has been suggested ^{88,91,92} that PhC cavities tailored with an appropriate mode configuration would qualify as excellent candidates. However, the trapped particle interacts only with a limited fraction of the optical field due to the nature of light to concentrate in the high refractive index

medium. As a first consequence, input laser powers required for demonstrating trapping so far, lie in the order of tens or even hundreds of milliwatts even though it has been predicted as early as 2006 that sub-mW trapping of 100 nm sized particles should be achievable ⁹¹. The second consequence is that the cavity mode is weakly perturbed by the presence of a particle in its vicinity making standard PhC cavities unsuitable for noticeable back-action effects. Nevertheless, it is possible to design dielectric microcavities with a significant field overlap on the low index medium, which we will refer to as hollow optical cavities ^{76, 93, 94} in analogy with the hollow core fibre terminology. In such cavities, it is expected that the enhanced field overlap can simultaneously allow quantifying the particle perturbation on the cavity mode and to evidence back-action ^{85, 95} phenomena.

One of the major objectives of this thesis is to apply hollow PhC cavities to optical trapping. Resonant optical trapping, when achieved in a hollow PhC cavity is accompanied by cavity back-action effects that result from two mechanisms. Firstly the effect of the particle on the resonant field creates a shift in the cavity eigenfrequency. Secondly, the effect of the resonant field on the particle is shown as a wavelength-dependent trapping strength. Hollow PhC cavities around 1.55 μm were designed, fabricated and characterized for optical trapping. This work was an extensive collaborative effort within our research group. Any single research project under this topic scheme contains different phases: design, simulation, device fabrication (PhC device and micro-fluidic membrane) and trapping experiments. We discussed about the design all together at the beginning. U. Dharanipathy mainly worked on the design of the sample and the numerical simulations. I was responsible for the device fabrication along with the antireflection coatings (PhC device by myself and micro-fluidic membrane by collaborators with my assistance). N. Descharmes and M. Tonin have performed the trapping experiments. These results have been done by 4 PhD students during a time span of 3 years. I was mainly involved in design, device fabrication and the discussion of the results.

This chapter is organized in the following way: In Section 5.1, the brief background review of optical trapping is given. The ray optics and the Rayleigh approximation of trapping force are discussed. Section 5.2 presents a brief introduction of recent results in optical trapping. A few examples for waveguide trapping and cavity optical trapping are shown. In Section 5.3, hollow PhC cavities used in this work taking into account the limitations of the previous works. In Section 5.4, the experimental setup will be detailed. As an important achievement, the design, fabrication and operation of the PDMS microfluidic cell will be explained in Section 5.5. In Section 5.6, Self-Induced Trapping along with the back-action between a resonant optical field and a 500 nm single nanoparticle is reported.

5.1 Introduction to optical trapping

A. Ashkin and his coworkers showed in the late 1980s that one could use the forces of radiation pressure from a focused laser beam to significantly affect the dynamics of small transparent micrometer sized neutral particles^{81, 82}. They demonstrated that optical forces could displace and levitate micron-sized dielectric particles in both water and air, and also developed a stable, three-dimensional trap based on counter-propagating laser beams. Two basic optical forces were identified: a scattering force in the direction of the incident light beam, and a gradient force in the direction of the intensity gradient of the beam. The techniques of optical trapping and manipulation of neutral particles by lasers provide unique means to accelerate, decelerate, deflect, guide, and even stably trap small particles.

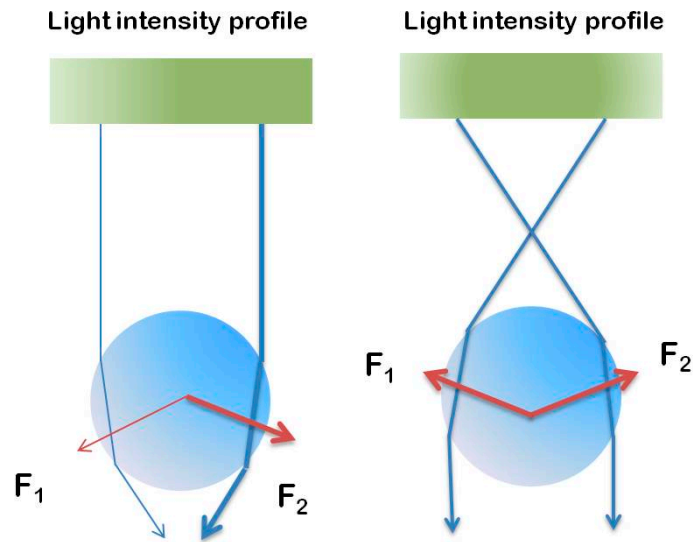


Figure 5.1 Ray optics description of the gradient force. Left: A transparent particle is illuminated by a parallel beam of light with an intensity gradient increasing from left to right. Two representative rays of light of different intensities (represented by blue lines of different thickness) from the beam are shown. The net force on the bead is to the right, in the direction of the intensity gradient, and slightly down. Right: In this case, a focused beam of light with a radial intensity gradient illuminates the bead. The change in momentum in this instance leads to a net force towards the focus. If the bead moves in the focused beam, the imbalance of optical forces will draw it back to the equilibrium position⁹⁶.

An optical trap is formed by tightly focusing a laser beam with an objective lens of high numerical aperture (NA). A dielectric particle near the focus will experience a force due to the transfer of momentum from the scattering of incident photons. The resulting optical force has traditionally been decomposed into two components: (1) a scattering force, in the direction of light propagation and (2) a gradient force, in the direction of the spatial light gradient. This decomposition is merely a convenient and intuitive means of discussing the overall optical force.

One can consider the radiation pressure force of light on a totally reflecting particle. As we know, the momentum of a single photon is $h\nu/c$. If we have an incident power of P , we have $P/h\nu$ photons striking the particle per second. Since all these photons are assumed to reflect straight back, the total change in momentum of the light is $2P/c$ per second. P is the power on the particle, or energy flux and c is the speed of light in free space. As a result, there is a net momentum transfer to the particle from the incident photons. For an isotropic scattering, the resulting forces cancel in all but the forward direction, and an effective scattering cross section can be calculated for the object ⁹⁷.

In most conventional situations, the scattering force dominates. However, if there is a steep intensity gradient (i.e., near the focus of a laser), the second component of the optical force, the gradient force, must be considered. The gradient force, as the name suggests, arises from the fact that a dipole in an inhomogeneous electric field experiences a force in the direction of the field gradient (as shown in Fig. 5.1). In an optical trap, the laser induces fluctuating dipoles in the dielectric particle, and it is the interaction of these dipoles with the inhomogeneous electric field at the focus that gives rise to the gradient trapping force. The gradient force is proportional to both the polarizability of the dielectric and the optical intensity gradient at the focus.

Most particles trapped in optical tweezers are too small for geometric optics to be a reliable approximation ⁹⁸. Ray optics calculations are useful for large spheres (few micrometers diameter). An alternative approximate method is to consider particles that are small compared to the wavelength—the Rayleigh limit. One of the effects of an electromagnetic field on matter is to induce a dielectric polarization, determined by the field and the permittivity of the medium. The refractive index is determined by the permittivity, so the polarization is a function of the optical properties of the medium. For the case of a sphere in a uniform field: a dipole moment of

$$\mathbf{p} = 4\pi n_{\text{med}}^2 \epsilon_0 r^3 \left(\frac{m^2 - 1}{m^2 + 2} \right) \mathbf{E}, \quad (5.1)$$

is induced in the sphere by an electric field \mathbf{E} , where n_{med} is the refractive index of the surrounding medium, m is the relative refractive index of the particle, with $m = n_{\text{part}}/n_{\text{med}}$, and we use \mathbf{p} for the dipole moment. From the energy of dipole in an applied field, it can be shown that the force acting on the sphere is ⁹⁹

$$\mathbf{F}_{\text{grad}} = \frac{2\pi n_{\text{med}}^2 r^3}{c} \left(\frac{m^2 - 1}{m^2 + 2} \right) \nabla I, \quad (5.2.1)$$

$$\mathbf{F}_{\text{grad}}/V \propto \nabla I, \quad (5.2.2)$$

Since this is proportional to the gradient of the irradiance I , it is called the gradient force. Note that it is also proportional to the volume of the sphere (i.e., proportional to r^3). If a

trapped particle is much smaller than the wavelength of the trapping beam, it will be in an approximately uniform field. It is worth to mention the gradient force volume density is proportional to the gradient of the optical field.

If the field were static, Eq. (5.2.2) would give the total force. However, the field is time-varying, with the direction of the induced dipole moment changing twice every optical period. This time-varying dipole moment is equivalent to a current, and since a magnetic field exerts a force on a current, one expects a force to act on the sphere. An oscillating dipole moment is the classic ideal short dipole antenna, which radiates energy. Since energy is removed from the incident beam and reradiated, momentum must also be removed from the incident beam. For a Rayleigh scatterer, the re-radiation is symmetric and has a total momentum flux of zero. Hence the momentum transfer to the particle is equal to the momentum associated with the incident energy lost, and the force magnitude is ⁹⁹

$$F_{\text{scat}} = \frac{8\pi n_{\text{med}}^2 k^4 r^6}{c} \left(\frac{m^2 - 1}{m^2 + 2} \right) I, \quad (5.3)$$

where k is the wavenumber of the trapping beam. This force is usually called the scattering force. While the scaling of gradient forces and scattering forces with volume suggests that, any non-absorbing sufficiently small particles can be trapped in three dimensions, this is not the case in practice. The trapped particle undergoes random motion due to thermal fluctuations—Brownian motion. The thermal kinetic energy of a particle in the trap is $k_B T$, where k_B is Boltzmann's constant and T is the absolute temperature. Noting that a conservative force is the gradient of a scalar function and that the gradient force is proportional to the irradiance, we see that the gradient force is conservative, and is the gradient of the trapping potential

$$U = \frac{2\pi n_{\text{med}} r^3}{c} \left(\frac{m^2 - 1}{m^2 + 2} \right) I, \quad (5.4)$$

If this trapping potential exceeds the thermal kinetic energy significantly, the particle is unlikely to escape due to Brownian motion. We can also compare the trapping force against the average magnitude of the force due to Brownian motion, which is $12\pi\eta k_B T$ where η is the viscosity of the fluid. Viscous drag in the medium will assist the trap in preventing escape; consideration of this is essentially equivalent to comparing the trapping potential with the thermal kinetic energy. In principle, the Brownian motion force, which is independent of the trapping power, can be overcome by the use of sufficient power, but the power required may well destroy the particle (especially complex biological materials) in practice.

Both the geometric optics and Rayleigh approximation provide the means to understand qualitative pictures of trapping, and useful quantitative results in their

respective size regimes. However, many particles in optical trapping lie between these two regimes, and require the use of exact electromagnetic theory to calculate forces and torques.

5.2 Recent results in this field

In this section we review some of the recent experimental results of near field optical trapping. In each case, we begin with a single short case study and briefly review the key achievements. Although the mechanisms are similar, we split this section into two parts: planar waveguides and optical resonators. We have tried to focus here on techniques very similar to our work, which will be discussed in the following sections.

Manipulation of dielectric objects with much smaller diameters (sub-100 nm), however, requires stronger optical confinement and higher intensities than cannot be provided by these diffraction-limited systems. Yang and co-workers (as shown in Fig. 5.2) present an optofluidic transportation approach to overcome these limitations, using subwavelength liquid-core slot waveguides¹⁰⁰. As illustrated in Fig. 5.2, the slot waveguide comprises a nanoscale slot sandwiched between two materials of much higher refractive index. As shown in Fig. 5.2 b, there exists a pseudo-transverse-electric (TE) mode that has a large electric field discontinuity at the horizontal boundaries of the slot region. The result is a high-intensity eigenmode in the slot making the majority of the optical energy accessible within the low-index fluid region.

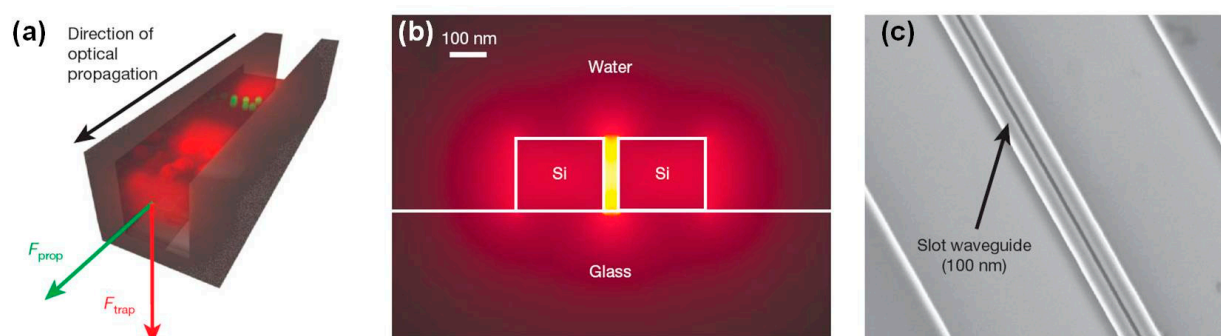


Figure 5.2 Nanoscale optofluidic transport. (a), Schematic illustrating the transport of two different sizes of nanoparticles in a slot waveguide. (b), Mode profile for a silicon-on-insulator 40-nm slot waveguide immersed in water. The main trapping region is in the high-intensity slot mode. (c), Scanning electron microscope image of 100-nm slot waveguide structure (reprinted from ref. 100).

The technique simultaneously makes use of near-field optical forces to confine matter inside the waveguide and scattering/adsorption forces to transport it. The ability of the slot waveguide to condense the accessible electromagnetic energy to scales as small as 60nm allows them also to overcome the fundamental diffraction problem. They applied the approach to the trapping and transport of 75 nm dielectric nanoparticles and λ -DNA molecules.

Another type of optical trapping is the optical resonator trapping. In the paper by Mandal co-workers¹⁰¹, they present a new class of resonant optical traps that are capable of generating extremely strong optical field gradients in three dimensions while simultaneously enhancing the trap stiffness due to the amplification of the optical field within the resonator and enabling advanced particle handling functionalities. As illustrated in Fig. 5.3a, their optical trap consists of a one-dimensional silicon PhC resonator that is evanescently coupled to a single mode ridge waveguide. The standing wave nature of the resonant optical field within the resonator enables a true static point trap with strong field confinement in all three dimensions. When light at the resonance wavelength is coupled from the bus-waveguide, a stationary interference pattern is formed within the PhC resonator resulting in a tight confinement of the optical field in an extremely small volume as illustrated in Fig. 5.3b. These strong field gradients coupled with the resonant amplification of the optical field within the resonator enables the stable trapping of particles ranging in size from 50 to 500 nm.

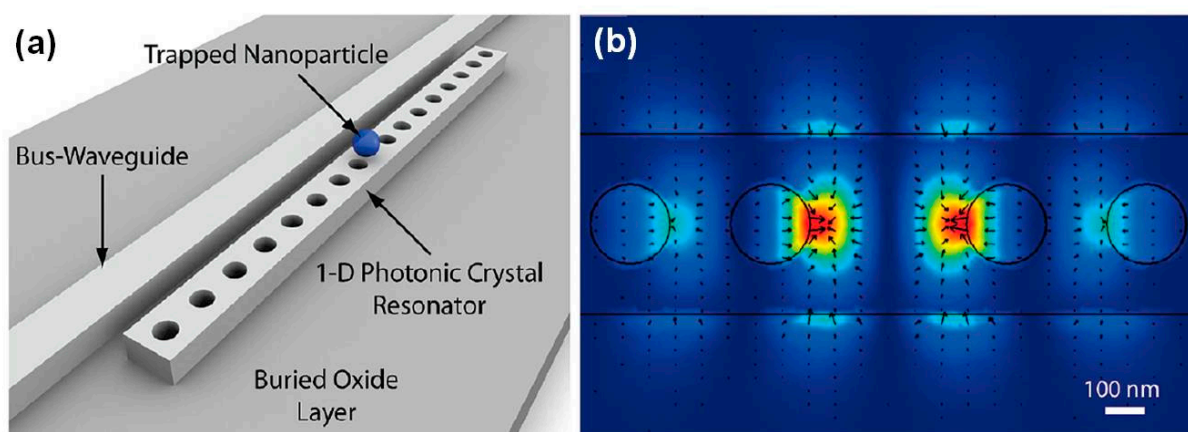


Figure 5.3 PhC resonator for enhanced optical trapping. (a), 3D schematic of the one-dimensional PhC resonator optical trapping architecture (b), 3D FEM simulation illustrating the strong field confinement and amplification within the one-dimensional resonator cavity. The black arrows indicate the direction and magnitude of the local optical forces (reprinted from ref. 101).

The trapping of 48 nm and 62 nm dielectric nanoparticles was demonstrated along with the ability to transport, trap, and manipulate larger nanoparticles by simultaneously exploiting the propagating nature of the light in a coupling waveguide and its stationary nature within the resonator. Field amplification within the resonator is shown to produce a trap several orders of magnitude stronger than conventional tweezers and an order of magnitude stiffer than other near-field techniques. Their approach is important as a new class of optical trapping platforms that could eventually enable complex all-optical single molecule manipulation and directed assembly of nanoscale material.

5.3 Hollow photonic crystal cavities

Hollow PhC cavities are the specific type of cavities used in our work. Therefore, we briefly introduce the advantages of this type of cavities as a key component in the trapping platform.

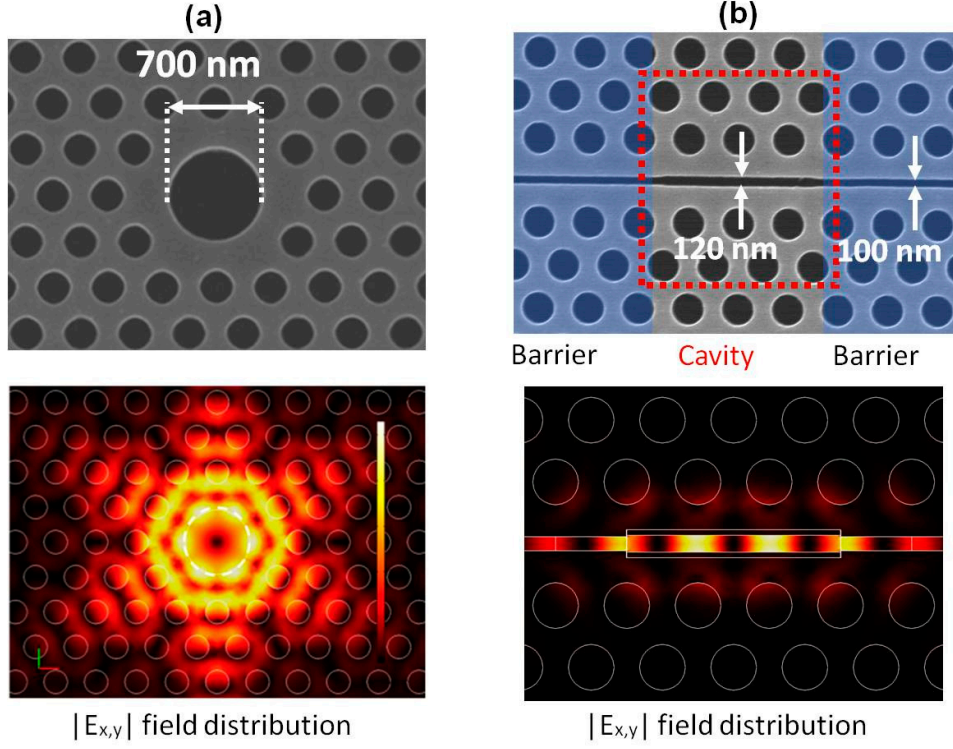


Figure 5.4 Hollow PhC cavities. (a), SEM image and field distribution of the big hole cavity (diameter is 700 nm and estimated resonance mode overlap with low index medium is 15%, Q -factor is 6000 in air and sensitivity is 150 nm/RIU). (a), SEM image and field distribution of the slot cavity (dimension is 100×1000 nm and estimated resonance mode overlap with low index medium is 80%, Q -factor is 30000 in air and sensitivity is 500 nm/RIU).

Waveguides and resonator based optical trapping platforms are discussed in the previous section. In the case of slot waveguides showed in Fig. 5.2, when a particle comes in contact with the optically excited waveguide it might be captured in the evanescent field and begin to move in the direction of optical propagation. As the trapping occurs along a propagating wave, rather than in standing wave as with traditional traps, the potential applications are limited. In case of 1D photonic resonator showed in Fig. 5.3, the inherent nature of light to concentrate in the high refractive index medium results in the fact that the trapped particle interacts only with a limited fraction of the resonance optical field. As a consequence, trapping power required for demonstrating trapping is relatively larger than expected. As shown in Fig. 5.4, it is possible to design dielectric micro-cavities with a significant field overlap on the low index medium, which we will refer to as hollow optical cavities. It was expected that the enhanced field overlap can simultaneously allow to more

stable trapping with less trapping power and further demonstrate the particle perturbation on the cavity mode.

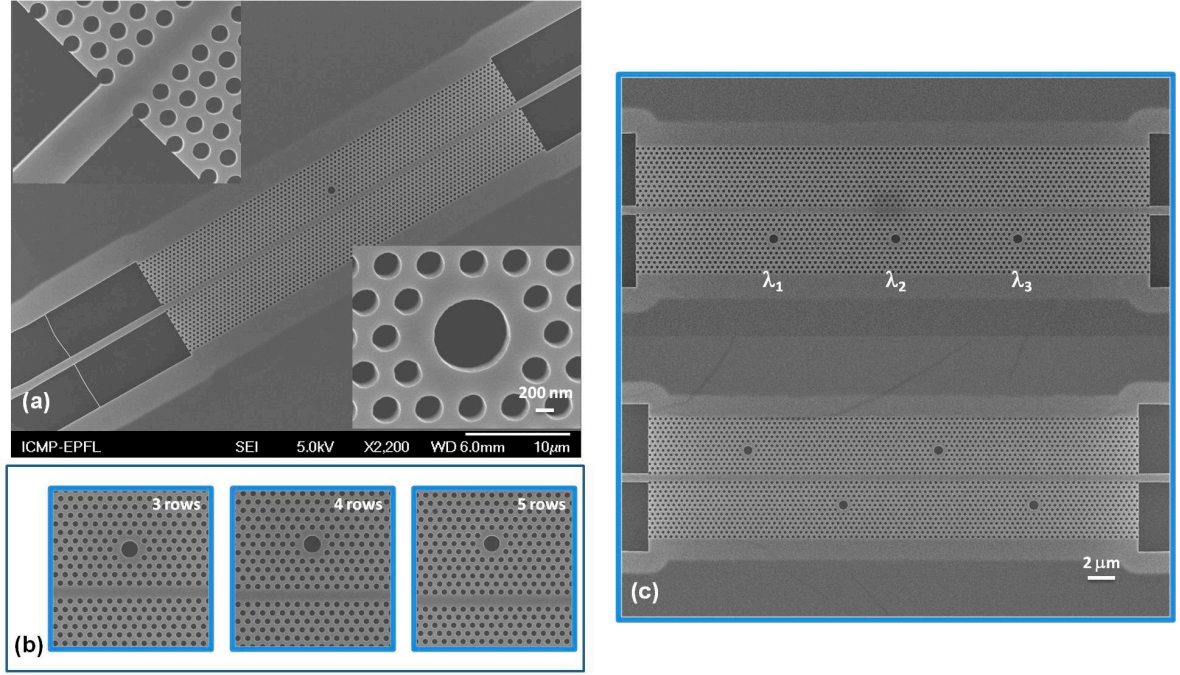


Figure 5.5 Hollow PhC cavities (a) SEM images of a hollow PhC cavity device. Lattice constant a is 440 nm and the diameter of the defect hole is 700 nm. Insets are highlight images of the ridge waveguide input and the circular defect (sample was tilted for 12 degree in vertical direction to achieve better view of the side wall of the PhC membrane). (b) SEM images of hollow cavities with different coupling barriers (3, 4 and 5 rows) from the W1 waveguide. (c) SEM images of device with arrays of hollow PhC cavities. The diameters of defect holes are d_1 , d_2 and d_3 . The cavity resonance wavelengths are at λ_1 , λ_2 and λ_3 respectively. Each cavity can be excited with corresponding resonance wavelength.

In this experiment, the hollow structure consists of a circular defect (700 nm in diameter) in a triangular PhC lattice on a silicon membrane (as shown in Fig. 5.5a). This cavity allows for a hexapole field distribution as shown in Fig. 5.4a displaying experimental quality factors of up to 2000 in water ($Q_{\text{FEM}} \sim 3300$), an estimated mode volume of $0.36 \mu\text{m}^3$ and field overlap of 15% with the volume enclosed by the circular defect. The measured quality factors of the resonance mode are 7500 in air and 1500 in water respectively. The hollow cavity resonance frequency can be tuned by changing the diameter of the defect hole. The coupling strength between the W1 waveguide and hollow cavity depends on the numbers of the barriers (as shown in Fig. 5.5b: 3, 4 and 5 rows of air holes). The resonance mode quality factor increases and the optical power coupled into the hollow cavity decreases when the number of barrier is increased. It is also possible to integrate several hollow cavities with different resonance frequencies (as shown in Fig. 5.5c). These hollow cavities can be independently excited by corresponding wavelength,

which is important to achieve arrays of optical traps in a single device for further complicated applications.

5.4 Experimental set-up

The schematic of the experimental setup is shown in Fig. 5.6. The assembled optofluidic chip is connected to an excitation laser. This laser, a fibre-coupled tuneable laser diode, emits a narrow linewidth radiation around $1.5\ \mu\text{m}$. The laser light is guided to the hollow PhC cavity through tapered fibres, impedance matched ridge waveguides and PhC W1 waveguides successively. The light transmitted through the PhC structures is guided out of the chip and directed towards an InGaAs detector where the signal is recorded. In the meantime, fluorescent imaging of the nanoparticles near the cavities is performed. An Argon laser (Lex: 488 nm) is used to excite the fluorescence of the particles. The fluorescence emission centred on 570 nm is collected through an oil immersion objective (Leica, 100x, NA 1.4) and imaged onto an EMCCD camera (ImagEM 512, Hamamatsu).

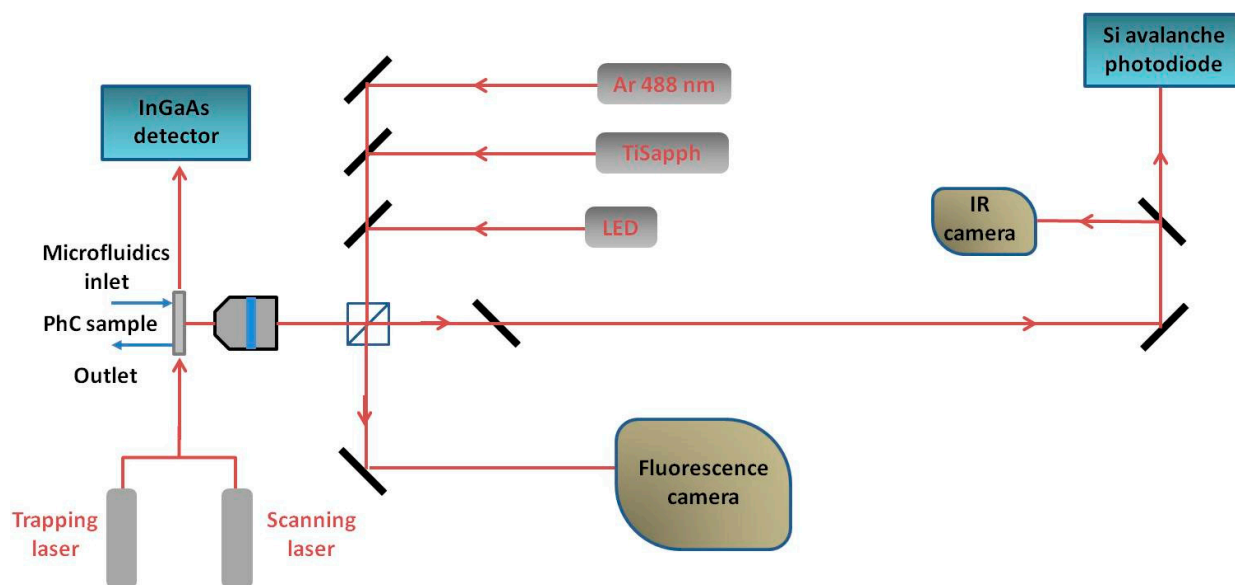


Figure 5.6 Schematic illustration of the experimental setup (some optical elements, like lens, are omitted).

5.5 Microfluidic cell

The PDMS membrane shown in Fig. 5.7 serves two major functionalities. Firstly, it allows for the accurate injection and transport of the nanoparticles towards the optical cavities and secondly, it maintains high quality optical imaging from the top of the sample. It is fabricated following standard soft lithography²³ processes as shown in Fig. 5.8. A first layer which is $30\ \mu\text{m}$ thick, is spin coated on a positive photoresist (AZ9260) mould. In the meantime, a second PDMS membrane that is $140\ \mu\text{m}$ thick is spin coated on a negative

photoresist (SU8) mould on silicon. The thicker layer, including the control channels, is then deposited on the thinner layer, which carries the infiltration channel (120 nL). The assembled PDMS structure is finally placed on the PhC chip and a 3 mm PDMS interconnect is permanently added to ensure stable injection and pressure control.

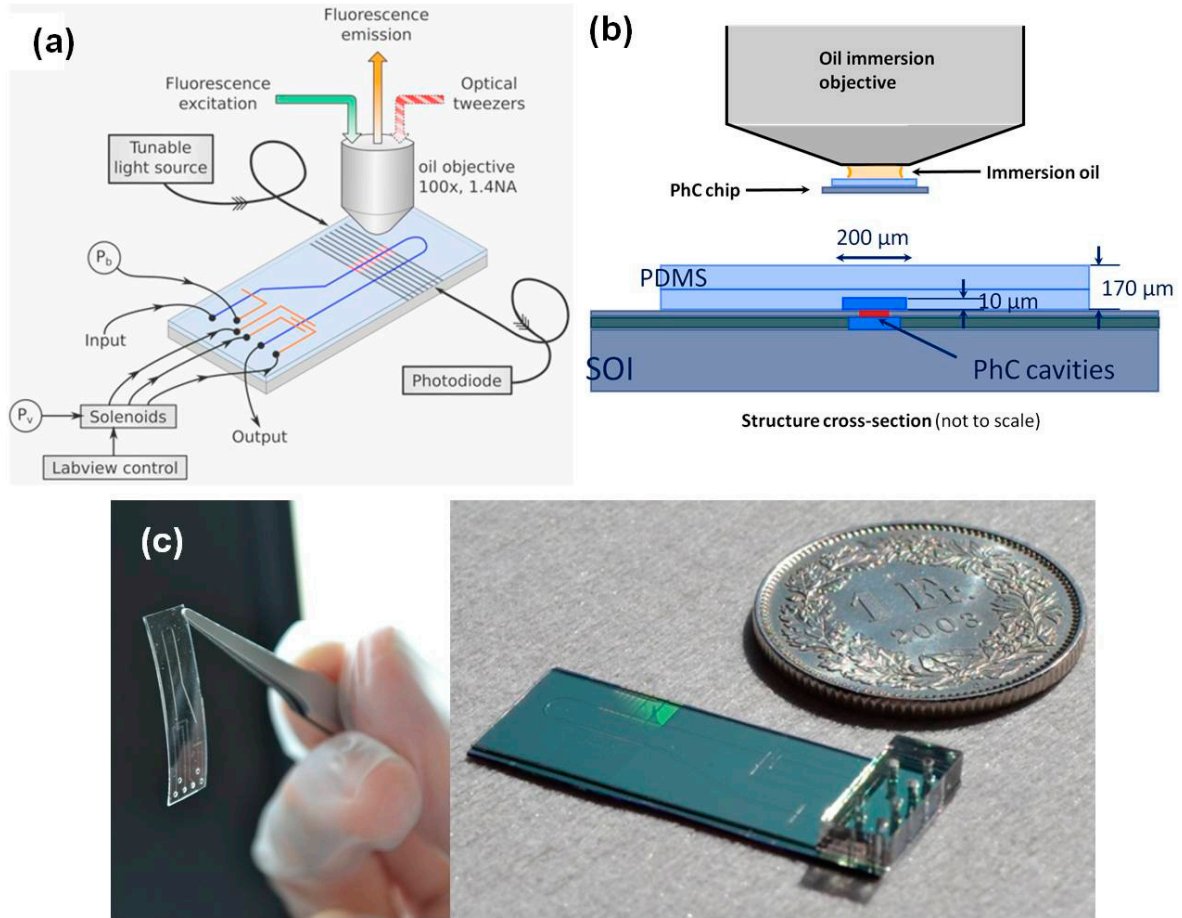


Figure 5.7 Optofluidic chip (a) Schematic of the optofluidic chip when operated. (b) Schematic cross-section view of the optofluidic chip (c) Photographs of the thin PDMS membrane after fabrication and the optofluidic chip when fully assembled.

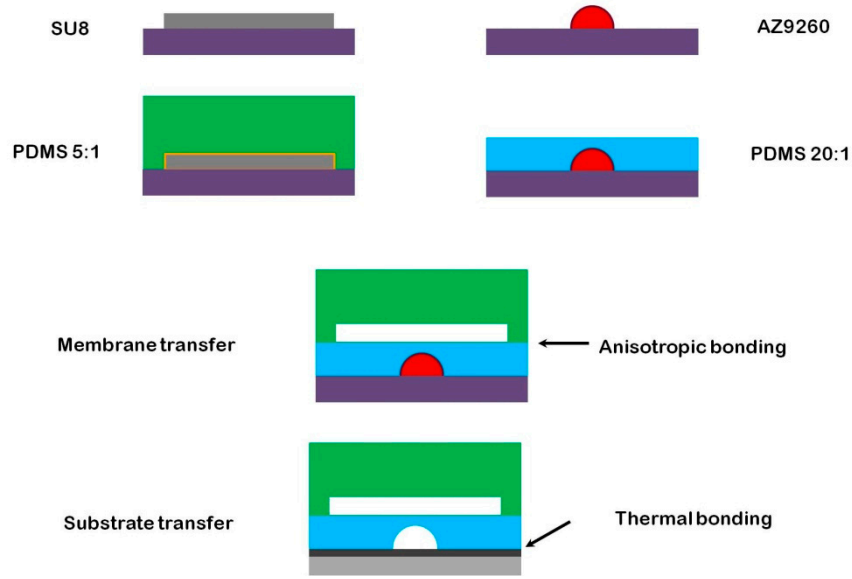


Figure 5.8 Schematic fabrication of the PDMS membrane. A 30 μm thick layer of PDMS membrane (including the infiltration channel) is spin coated on a positive photoresist (AZ9260) mould. In the meantime, another 140 μm thick layer of PDMS membrane (including the control channels) is spin coated on a negative photoresist (SU8) mould on silicon. The thicker layer is then deposited on the thinner layer by anisotropic bonding. The assembled PDMS structure is finally placed on the PhC chip by thermal bonding.

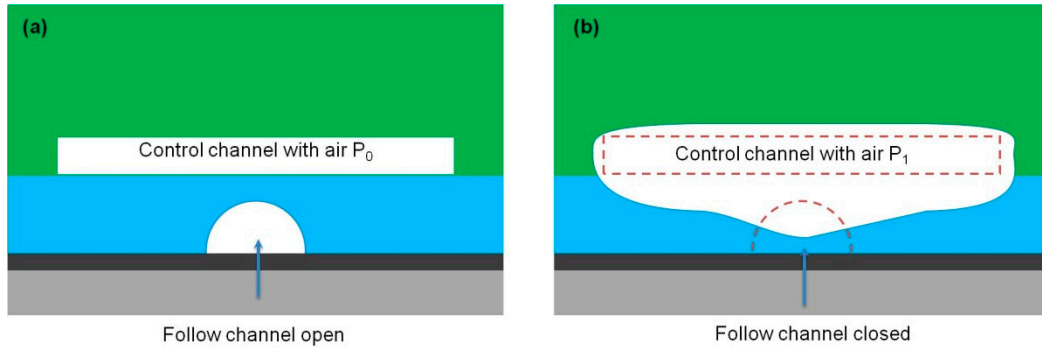


Figure 5.9 Microfluidic control and flow channels. (a) The upper control channel (air pressure P_0) is off and the lower flow channel is open. (b) The upper control channel (air pressure P_1) is on and the lower flow channel is closed.

As shown in Fig. 5.7a, the experiment is performed as follows: a diluted solution of carboxylate-modified particles (refractive index 1.59) is injected inside the microfluidic channel using a slight overpressure of 4 psi (275 mbar). The velocity of the particles at this stage, without extra flow control can reach several millimetres per second. It is therefore crucial to be able to slow down and eventually stop the particles in the vicinity of the hollow PhC devices. A set of pneumatically controlled valves¹⁰² positioned above the entrance and exit of the channel has been integrated for this purpose (as shown in Fig. 5.9). Typical working pressures of 7 psi are usually more than enough to arrest the particles,

leaving them in their natural Brownian motion. Peristaltic actuation of these valves also allows for controlled injection of the particles in volumes of the order of 500 pL per cycle.

5.6 Single particle trapping and back action

* The main results in this section are originally published in “Observation of back-action and self-induced trapping in a planar hollow PhC cavity” *Phy. Rev. Lett.*, **110**, 123601, (2013).

In this section, the hollow PhC cavity detailed in section 5.3 is used to perform optical trapping on small particles of the size of a virus with very low powers ($\sim 100 \mu\text{W}$). The particle is permanently held in suspension within a small volume with strongly confined light as shown in Fig 10a. In such a resonant optical trap, the spectral properties of the optical micro-cavity are influenced by the presence of the object under study. One effect is the shift of the resonance frequency due to the local refractive index perturbation caused by the particle. Particle size and polarisability are the two main parameters dictating the maximum resonance frequency shift associated with one object. When the system is excited appropriately off-resonance, a particle that is in the proximity initiates an energy build-up inside the cavity, which consequently attracts the particle towards a stable trap region located in the central plane of the hollow volume as shown in Fig 10b,c, and d. This back action effect is the key to low power integrated optical traps, which is experimentally demonstrated for the first time.

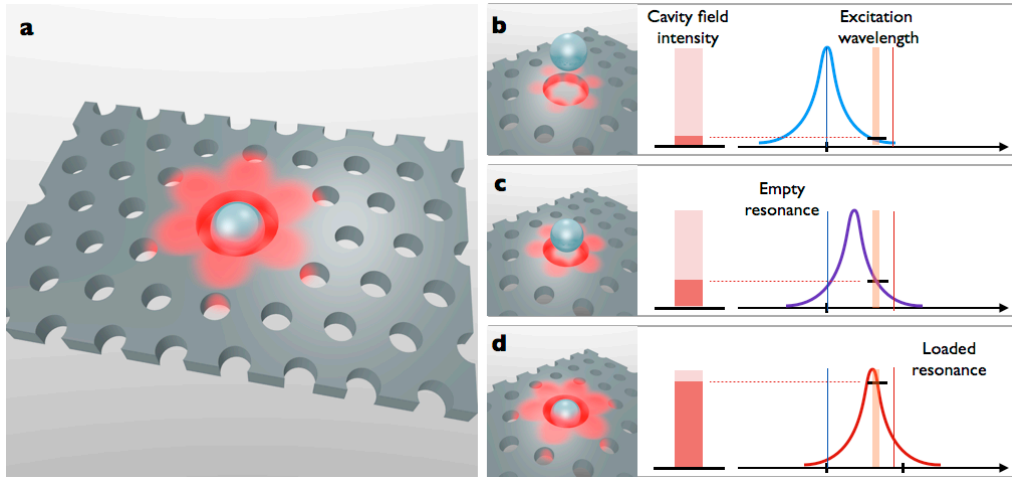


Figure 5.10 Electric field distribution of a hollow cavity with the presence of a particle. (a) The in-plane electric field distribution when a particle is held in the resonant optical trap. (b),(c) and (d) illustrate the back-action mechanism. The field build-up inside the cavity is shown as the particle is being pulled towards the trap centre along with the illustration of the resonant frequency shift that modulates the amount of energy inside the cavity.

The hollow PhC cavities are implemented in a $30 \times 12 \text{ mm}$ integrated optofluidic chip^{103, 104}. The experimental setup and characterization procedures were detailed in Section 5.4. The microfluidic circuitry was detailed in Section 5.5 that enable us to control the flow

precisely in the channel. The flow in the channel is arrested, letting the particles in non-constrained Brownian motion near the cavity region.

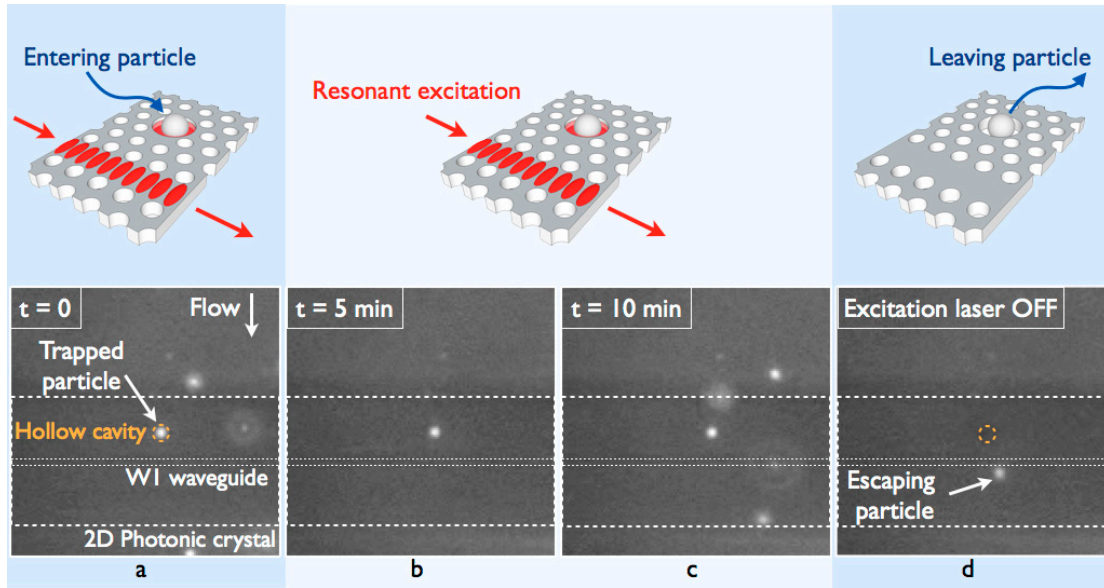


Figure 5.11 Resonant optical trapping inside the hollow PhC cavity. (a) A single 500 nm fluorescent particle is resonantly trapped inside the PhC cavity region with a waveguide power lower than $120 \mu\text{W}$. (b) and (c) The particle remains strongly trapped for 10 minutes while other fluorescent particles are seen in the flow near the trapped particle. (d) The particle immediately leaves the cavity when the excitation laser is turned off after 10 minutes of continuous trapping.

A particle in the vicinity of the cavity can be captured by the resonant field, which extends a few hundred nanometres above the surface of the slab. The field gradient along the vertical direction gives rise to a restoring force pulling the particle towards the central plane of the slab. The particle can be permanently trapped²⁶ (Fig. 5.11a-c) and released on-demand (Fig. 5.11d) by turning off the excitation laser. Records of trapping times over 20 minutes have been achieved without apparent photodamage or photobleaching of the particle. Estimated power in the waveguide near the cavity is lower than $120 \mu\text{W}$ for the case of the permanent trap²⁷. Shorter trapping times (few tens of seconds) have been observed for guided powers as low as $37 \mu\text{W}$. These unique trapping characteristics are the direct consequence of accessing the internal cavity field in contrast to schemes^{105, 106} involving only the evanescent tail of a resonant mode.

As introduced before, the presence of the particle generates a local perturbation of the intracavity refractive index that results in a shift (δ) of the cavity resonance wavelength. Such a shift can be measured while a particle is trapped. Two laser sources are used to characterize the dynamic wavelength shift of the cavity mode. The first laser excites the cavity eigenmode at a fixed wavelength, which traps the particle as explained before. The second laser, of weaker intensity, is coupled through the same end-fire setup using a 90/10

fibre coupler. In this manner, the cavity spectrum can be acquired without altering the characteristics of the resonant trap. The probe laser signal is extracted from the more intense trapping laser signal with lock-in detection techniques. The evolution of the spectrum in time with a repetition rate of 1 Hz is displayed in Fig. 5.12a, which shows the optical response in the presence or absence of a particle within the cavity. The fluctuations of the cavity spectrum in the presence of the particle demonstrate the truly suspended feature of the trap and the constricted residual Brownian motion within the stable trap region. A snapshot (as shown in Fig. 5.12b) shows an average resonance shift of 1.8 nm from the unloaded cavity resonance (λ_0). This shift is as large as twice the linewidth ($\Delta\lambda$) of the unperturbed cavity mode. The apparent linewidth broadening in the presence of a particle is attributed to an averaging effect with the slow acquisition time of the measurement set-up. Theoretical computations were performed with a 3D FEM solver (COMSOL).

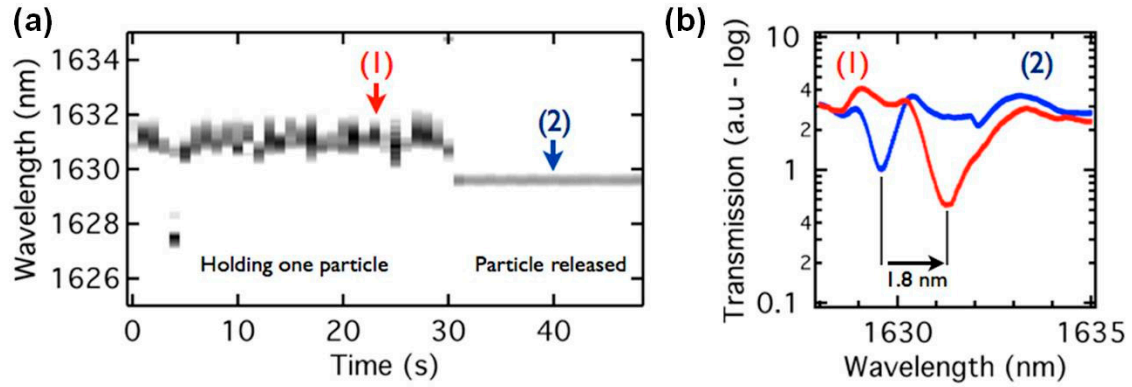


Figure 5.12 Experimental measurements of a single particle in a resonant trap. (a) Two laser sources are used to characterize the dynamic shift of the particle resonance. The first laser traps the particle resonantly while the second laser is used to scan the spectrum of the cavity resonance with standard lock-in detection. Dynamic particle induced resonance shifts can be observed as the particle is trapped inside the cavity while displaying Brownian motion around the stable trapping region. (b) A single snapshot from a displaying a maximum resonance shift of 1.8 nm from the unloaded cavity resonance.

The particle position dependent resonance wavelength shifts were computed by observing the change in the eigenfrequency of the system as the particle is moved inside the cavity volume. The resonance wavelength shifts induced by particles of different diameters are computed and summarized in Fig. 5.13. The magnitude of the shifts primarily depends on the overlap integral of the cavity field on the volume of the particle. A maximum shift of 2.6 nm is obtained in the case of a 500 nm polystyrene particle and is in reasonable agreement with the measurements shown before. As the size of the particle is progressively decreased, the maximum computed shift scales down rapidly. In the case of polystyrene particles smaller than 100 nm, the extremely weak particle-cavity interaction will make the back-action effects vanish. Moreover, a deviation of the particle's position

from the cavity centre along the vertical axis strongly reduces the magnitude of the wavelength shift.

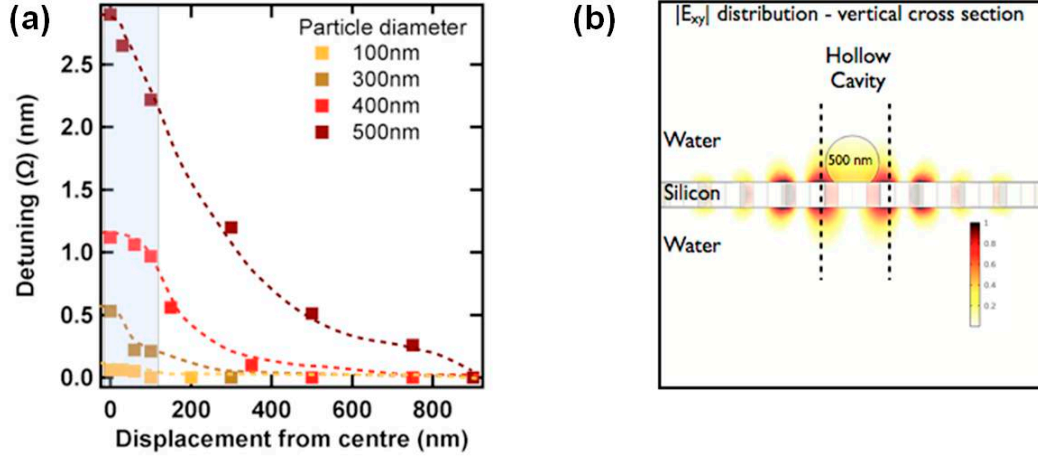


Figure 5.13 3D Numerical computations for resonance shifts and trapping potentials. (a) Resonance wavelength shift as a function of particle size as it is moved along the vertical direction. The shaded area shows the extent of the silicon slab. A maximum shift of 2.8 nm is found for a 500 nm particle. (b) Field overlap over the 500 nm particle seen from the vertical cross section of the silicon slab as the particle is positioned slightly above the centre of the cavity

When the particle is in Brownian motion within the hollow volume of the cavity, both the trapping and shift phenomena described before occur in a coupled manner. This coupling is at the core of the particle-cavity back-action, as the trapping characteristics will strongly depend on the relative position of the excitation wavelength with respect to the unloaded (λ_U) and loaded (λ_L) cavity wavelengths. The Brownian motion induces resonance wavelength shifts, which, for a monochromatic excitation, renormalizes the amount of energy coupled to the cavity and consequently the trapping forces. Concurrently, the energy required by the particle to escape the resonant trap depends on the excitation wavelength in a non-trivial manner. In other words, the wavelength-dependent escape energy profile does not reproduce the loaded cavity optical response as would be expected from a non-coupled system. On the contrary, a more complex profile extending over several cavity linewidths is observed. As a direct signature of the back-action effect, the largest escape energy required for the particle to leave the trap is expected to occur neither at λ_U nor at λ_L but in a region in-between. This is demonstrated by monitoring the trapping threshold power for a range of wavelengths centred on λ_U . While a particle is held in the resonant trap for a given wavelength, the excitation power is progressively decreased until the particle escapes. Fig. 5.14 reports the evolution of the escape threshold power for a range of wavelengths detuned from λ_U . As expected, the resonant nature of the trap not only results in a restricted range of wavelengths only for which it is possible to observe trapping but also two distinct minima associated to two trapping regimes can be observed.

The first regime (a) has a large trapping bandwidth and the lowest threshold power of $37 \mu\text{W}$. The second regime (b) covers a narrower bandwidth centred near λ_L and has a larger threshold power of $99 \mu\text{W}$.

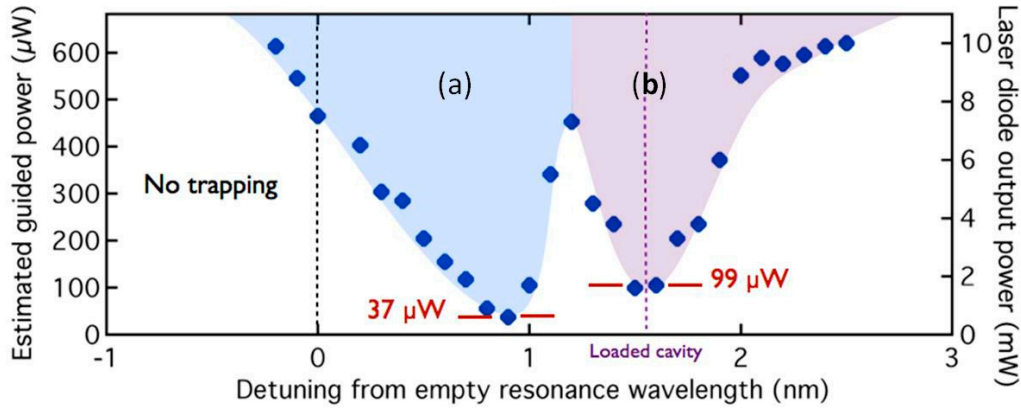


Figure 5.14 Demonstration of particle-cavity coupling. Record of trapping threshold powers as a function of the estimated guided power in the access waveguide (left axis) and the laser diode output power (right axis). Experimental points correspond to escape trapping times of the order of ten seconds.

Based on some preliminary modeling results, the existence of the two experimentally observed regimes is due to the out-of-plane and in-plane components get sequentially predominant with detuning. The first regime can be conceptualized as a quasi-1D trap, where the particle is held within the hollow volume wherein it experiences weak trapping forces. In these detuning values, the in-plane forces are considerably weaker compared to their out-of-plane counterparts. The second regime appears at the farther detuning values, closer to the loaded cavity wavelength. For these detuning values, the in-plane force component is larger than the out-of-plane one. Further work need to be done to fully understand the physics behind this measurement, which will be continued in our research group.

Conclusion

In summary, we have demonstrated the first experimental resonant optical trap in a 2D PhC cavity (700 nm diameter) that allows for simultaneous isolation, manipulation and analysis of dielectric particles (500 nm) similar in size with viruses and small bacteria with sub-100 μW trapping power. The cavity resonance shifts depends on the particle size, refractive index and shape (due to different overlap with the cavity mode, not demonstrated yet). This capability can be used to separate particles of different sizes or to separate particles of identical sizes but different refractive indices and might be even capable of separate identical particles with different form factors. Conversely, the hollow PhC cavity trap approach enables the possibility to capture an unknown particle using a well chosen detuned wavelength while simultaneously perform optical measurements of

the induced perturbation. This mechanism opens the door to new kinds of all-optical schemes where single biological entities like cell organelles and viruses can be isolated, analyzed and sorted depending on their size, shape and optical properties. The novel trapping mechanism can be extended for a variety of sizes owing to the scalability of PhCs. The sizes and wavelengths can be scaled down to other platforms like Gallium Nitride ¹⁰⁷ in the visible wavelength region where the smaller size of the cavity could facilitate the trapping of particles of the order of 50 to 100 nm. An additional remarkable fact from this scheme is that, it addresses both the lack of exclusivity and specificity of standard optical tweezers ¹⁰⁸. The long trapping times along with very small residual Brownian motion is of major interest for studies that use spatially resolved spectroscopy. The addressability of multiple traps and the compatibility to standard CMOS process brings immediate access to various exciting on-chip biological analysis applications for the near future. These results open the way to the exploration of such coupled systems where dynamical effects are expected to play a dramatic role ⁸⁷.

Chapter 6

Applications in THz photonic crystal lasers

The Terahertz (THz) frequency range is typically defined as light in the range of 0.1 - 10 THz in wavelength. It has been long time hindered by the lack of compact laser sources until the first demonstration of THz quantum cascade lasers ¹⁰⁹ (QCL) in 2002 ¹¹⁰. QC lasers have become the most widely used solid-state light source in THz frequency range ^{111, 112}. THz QCLs have a significant importance in many promising applications, such as astrophysics, biomedical spectroscopy, imaging, pollutant and environmental monitoring, and security screening. Thanks to the engineering of inter-sub-band optical transitions, many improvements of THz QCLs have been done on almost all aspects of their optical performance including power consumption, wavelength tuning range, output power, operation temperature, lasing mode and emission directionality control.

Photonic band engineering was proved to be a highly efficient way to control the emission properties of semiconductor lasers. Thanks to the scaling law between wavelength (λ) and lattice constant (a) of PhC, concepts of PhC semiconductor lasers can be exploited at any frequency ¹¹³⁻¹¹⁹. On one hand, for short wavelengths, *e.g.*, UV range, visible range, and near-Infrared, PhC structures usually suffer from the sub-nanometer fabrication imperfections even with state-of-the-art processing technique, challenging passive devices and active devices for practical applications. On the other hand, when the wavelength goes to longer wavelengths, *e.g.* far infra-red, or THz in frequency, the corresponding critical dimensions required for the PhC devices are in the range of micrometers. Such critical dimensions can be easily controlled through standard photolithography.

PhC lasers can be summarized in two groups, one is the PhC defect mode laser ¹²⁰ based on a resonant cavity mode, the other is the band-edge DFB laser (either one (1D) or two-dimensional (2D) ¹²¹⁻¹²³). In the THz frequency range, THz cascade structures are extremely well suited for their use in PhC structures. The double Plasmon (DP) waveguide ¹²⁴ enables the fabrication of different types of PhC structures with either complete or partial PBG, for pillar type PhC or hole type PhC lasers, respectively. The DP metallic layers can also operate as electrical contacts. Slow light THz PhC QCL lasers can be achieved either with a high index modulation scheme or with a low index scheme, leading to strong or weak PhC enhancement effects, respectively. Laser action based on weak PhC effect has

been demonstrated with low index modulation structures that are obtained by patterning the top metallic layer of the laser ^{114, 125} whilst leaving the active region un-etched. The strong PhC effect, which requires high index modulation, can be achieved with deeply etched structures ^{113, 115, 126} which are sandwiched within the two metallic layers.

One of the major objectives of this thesis is to apply slow light concepts to develop PhC THz light sources for applications. Consistent efforts have been concentrated on the generation of laser emission at low THz frequencies (1-3 THz range) on quantum-cascade epilayers, especially in continuous-wave operation which is required in many real world applications. The high index modulation scheme has been used in my work. Various designs of pillar type PhC slow light lasers at THz frequencies were designed, investigated, fabricated and characterized. This work was performed under close collaboration with the group of Prof. Jérôme Faist at Eidgenössische Technische Hochschule Zürich (ETHZ). Any single research project under this collaboration scheme contains 5 phases: design, simulation, epilayer growth, laser fabrication and characterization. The QCL epilayer growth and device characterization were performed at ETHZ. The PhC QCL laser design, simulation and fabrication were performed at EPFL.

This chapter is organized in the following way: In Section 6.1, the brief background review of the THz quantum cascade laser is given. Some examples of THz applications will be given as well. As the most important candidate light source in the THz range, the basic and development of quantum cascade laser will be discussed. In order to understand our PhC lasers and compare them with other lasers, Section 6.3 presents a brief introduction of distributed feedback (DFB) lasers. Section 6.4 will show several important results on the investigation of PhC THz QCL lasers. Key improvements will be discussed, both for high index modulation scheme and low index modulation schemes. In Section 6.5, the design, fabrication and characterization of continuous-wave vertically emitting PhC THz laser will be discussed. The fabrication technique has been detailed in Chapter 3, therefore, a brief introduction of the characterization technique used in ETHZ will be given in Section 6.5. Here, we report on a robust surface emitting continuous-wave terahertz QC laser realized by a second order Bragg grating extractor and an optimized two dimension PhC structure. By extracting light from the boundary of the laser device which is emitting at 3.2 THz and achieving efficient heat dissipation inside the PhC structure, CW operation with 3 mW output power and maximum operating temperature (T_{\max}) of 100 K is demonstrated. It is important to note that highly directional far-field pattern paves the way towards real world applications.

6.1 Introduction to the THz frequency range

THz lies between photonics and electronics as illustrated in the electromagnetic spectrum shown in the bar graph of Fig. 6.1. The visible part of the electromagnetic

spectrum is familiar to us, and contains the colors of light with which most of us are familiar. Within this visible spectrum, red has a longer wavelength than blue, and red also corresponds to a lower frequency of oscillation. Towards higher frequencies are ultraviolet, x-rays, then gamma rays, while in the other direction, at lower frequencies come infrared, far-infrared, microwaves, radar and radio waves. The study of visible light is sometimes called photonics, the sources being light bulbs, LED and lasers. Electromagnetic waves at much lower frequencies are usually generated in a different way, using electronics and oscillators. In between these two regions lies a part of the spectrum which is more difficult both to generate and detect. We are speaking of light in the far-infrared, whose frequencies lie in the region from 0.1–10 THz, and whose wavelengths are from 3 mm to 30 μm ¹¹¹.

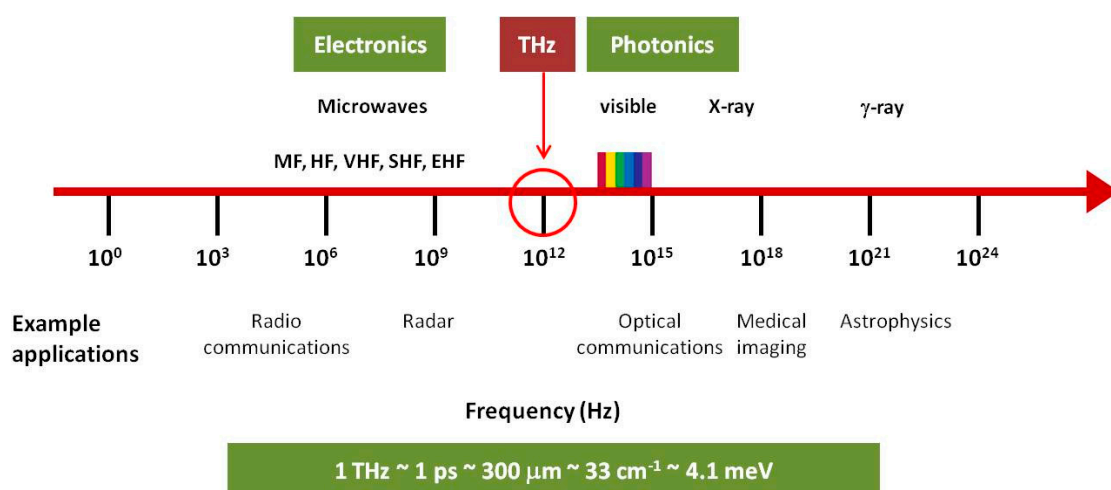


Figure 6.1 Schematic of the electromagnetic spectrum showing how THz light lies between electronics and photonics.

The presence of high atmospheric absorption constrained early interest and funding for THz science. Historically, the major use of THz spectroscopy has been by chemists and astronomers in the spectral characterization of the rotational and vibrational resonances and thermal-emission lines of simple molecules. The past 20 years have seen a revolution in THz systems, as advanced materials research provided new and higher-power sources, and the potential of THz for advanced physics research and commercial applications was demonstrated. Terahertz technology is an extremely attractive research field, with interest from sectors as diverse as the semiconductor, medical, manufacturing, space and defense industries. Several recent major technical advances have greatly extended the potential and profile of THz systems. The two most important applications of THz technology: Terahertz spectroscopy and Terahertz Imaging will be briefly introduced here.

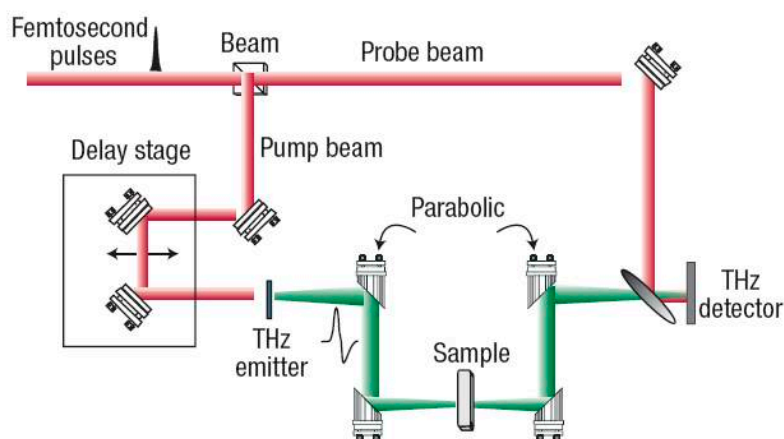


Figure 6.2 Illustration of a THz-TDS pump probe system. The ultrafast laser beam is split into pump and probe beams. The pump beam is incident on the THz emitter to generate THz pulses, and the THz pulses are collimated and focused on the target using parabolic mirrors. After transmission through the target, the THz pulse is collimated and re-focused on the THz detector. The optical probe beam is used to gate the detector and measure the instantaneous THz electric field. A delay stage is used to offset the pump and probe beams and allow the THz temporal profile to be iteratively sampled ¹²⁷(reprinted from ref. 127).

One of the primary motivations for the development of THz technology is the potential to extract material characteristics that are unavailable when using other frequency bands. Astronomy and space research has been one of the strongest drivers for THz research because of the vast amount of information that can potentially be collected on the presence of abundant molecules such as oxygen, water and carbon monoxide in stellar dust clouds, comets and planets ¹²⁸.

Many different methods exist to perform THz spectroscopy, such as Fourier transform spectroscopy (FTS), narrowband spectroscopy, and THz time-domain spectroscopy (THz-TDS ^{129, 130}, or called Terahertz Pulse Spectroscopy (TPS) ¹³¹). As the most common technique used for studying molecular resonances, the FTS has the advantage of an extremely wide bandwidth, enabling material characterization from THz frequencies to the infrared. The narrowband spectroscopy system can perform spectral measurements with a much higher resolution. Both FTS and narrowband spectroscopy are also widely used in passive systems for monitoring thermal-emission lines of molecules, particularly in astronomy applications. THz time-domain spectroscopy (THz-TDS) uses short pulses of broadband THz radiation, which are typically generated using ultrafast laser pulses. It has a number of advantages that have given rise to some important recent applications. The transmitted THz electric field is measured coherently, which provides both high sensitivity and time-resolved phase information. A THz-TDS system is described in Fig. 6.2. This THz-TDS can probe the THz spectral features of the two polymorphic forms of drug ranitidine hydrochloride (HCL). Signature peaks for each form can be identified easily using THz spectroscopy ¹³¹.

Early experiments by Hu and Nuss¹³² demonstrated that THz imaging could have biomedical applications—their THz images of porcine tissue showed a contrast between muscle and fat. Since its inception it has been used for imaging a wide variety of targets including semiconductors, cancerous tissue and flames. The attraction of THz imaging is largely due to the availability of phase-sensitive spectroscopic images, which holds the potential for material identification or ‘functional imaging’. Moreover, the non-ionizing properties of THz radiation are inherently safe for screening application.

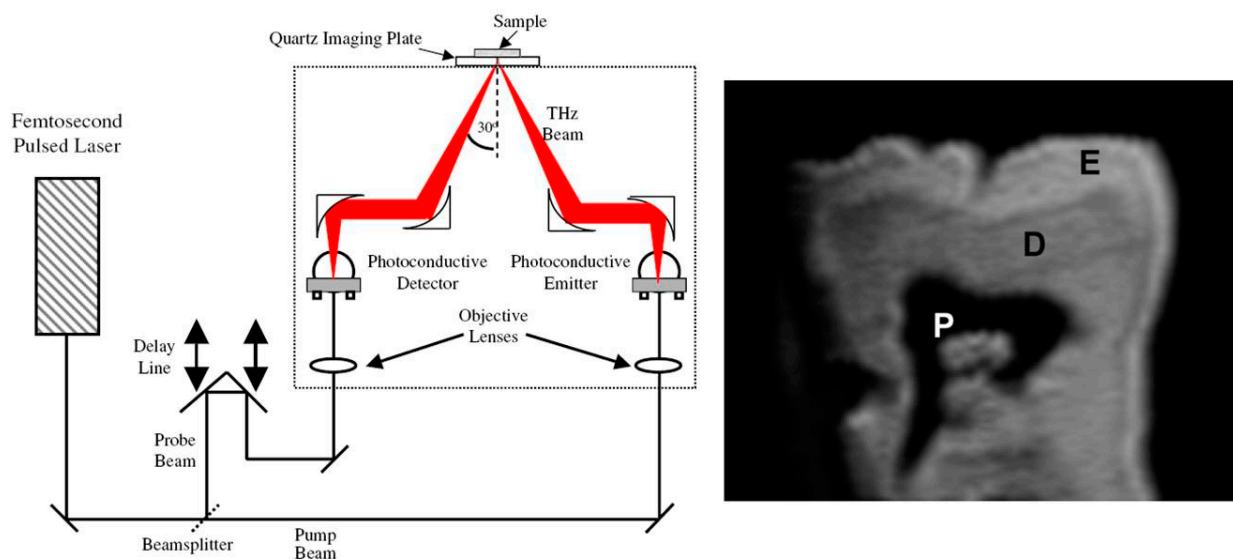


Figure 6.3 Left: Schematic diagram of the photoconductive reflection system. Right: A two-dimensional image of a human tooth. Labels E, D and P represent the enamel, dentine and pulp respectively¹³³ (reprinted from ref. 133).

An imaging system is illustrated schematically in Fig. 6.3. Generation of the THz pulses was achieved by the optical excitation of a gallium arsenide photoconductive emitter with a Ti: Sapphire ultrafast laser, emitting 100 fs pulses centred at a wavelength of 800 nm, with a 80MHz repetition rate and an average power of 250mW. A beam splitter separates the laser light into two beams, an excitation beam and a detection beam. The THz pulses are collimated and focused onto the top surface of a z-cut quartz window by a pair of off-axis parabolic mirrors. The sample under investigation is placed onto the quartz window, as indicated in Fig. 6.3¹³³.

One of the early applications of this imaging system was the detection of dental caries. Early caries is a result of mineral loss from enamel, and this causes a change in the refractive index within the enamel. This change in the refractive index means that small or subsurface lesions not visible to the naked eye can be identified. The benefit of early detection is that the initial stages of demineralization are reversible, and so the need for and discomfort of drilling could be removed. Fig. 6.3 is a two-dimensional THz image of a

transverse slice of a human tooth. The differences in the refractive index of the enamel, dentine and pulp, enable the three regions to be identified.

6.2 Quantum cascade laser

One of the major advances in THz sources is the use of coupled quantum wells, as introduced by Capasso's group in 2-D structures. The QCL laser was demonstrated first in the middle-infrared region (~ 70 THz) in 1994 by Faist and his co-workers¹⁰⁹. More recently the QCL in the THz range (4.4 THz) was introduced in 2002¹¹⁰. This laser emits high-power (tens of milliwatts) THz radiation at discrete frequencies from electronic inter-subband transitions in semiconductor hetero-structures. The active semiconductor structure is realized based on a multiple quantum-well (QW) hetero-structure in a GaAs/AlGaAs sandwich. The laser consists of coupled QWs constructed by nanometer-thick layers of GaAs sandwiched between potential barriers of AlGaAs. The quantum cascade consists of a periodic unit made up of an injector and an active region. In the active region, a population inversion exists and electron transitions to a lower energy level occur, emitting photons at a specific wavelength. The electrons then tunnel between the quantum wells and the injector region couples them to the higher energy level in the active region of the subsequent unit. The main issue in the development of THz QCLs is caused by the long wavelength of the THz radiation, buildup of electrons in lower levels, and a phonon bottleneck. The former effect results in a spectral broad optical mode, which results in poor overlap between the optical field and the gain medium, and high optical losses owing to free electron absorption in the medium. The optical losses scale as the square of the wavelength. Initial breakthrough developments have taken place in both the QW gain medium and in the waveguide structure. The resonant phonon scheme takes advantage of sub-picosecond electron longitudinal-optical (LO) photon scattering to selectively depopulate the lower energy level, together with the use of a metal-metal ridge waveguide, similar in form to a microstrip transmission line.

6.2.1 Quantum cascade laser

The band diagram of the first QCL¹⁰⁹ is reported in Fig. 6.4. The active layer of the laser structure consists of 25 periods of undoped $\text{In}_{0.48}\text{Ga}_{0.52}\text{As}$ QWs and $\text{In}_{0.47}\text{Al}_{0.53}\text{As}$ barriers with lattice matched to InP. It was grown by molecular-beam epitaxy (MBE)¹³⁴. One period consists in an active region and a relaxation-injection region (graded region in Fig. 6.4). An external electric field is applied as depicted by the linear slope of the electronic potential. The optical transition occurs in the active region, while the carriers relax after the optical transition and are reinjected in the next period in the relaxation-injection region. The carriers are injected by resonant tunnelling in the state '3', where they can relax to state '2' by means of photon-assisted tunneling or by scattering, mainly from LO phonon if the condition $E_{32} \geq \hbar\omega_{\text{LO}}$ is satisfied. Population inversion is achieved when the lifetimes (τ)

of the electrons in the quantum states satisfies the relation $\tau_{32} > \tau_2$. The lifetime τ_{32} is increased by employing a transition with a reduced spatial overlap of the wavefunctions, and the lifetime τ_2 is reduced by making the energy E_{21} resonant with an optical phonon energy that is the most efficient energy relaxation mechanism¹³⁵. The injector region is doped, acting as an electron reservoir and preventing the formation of space-charge domains. The cascaded geometry obtained by repeating N times the period allows electron recycling that can be re-injected in the subsequent period after performing the optical transition, thus giving rise to internal quantum efficiency in principle greater than one and equal to the number of periods: the same electron can emit N photons¹³⁶.

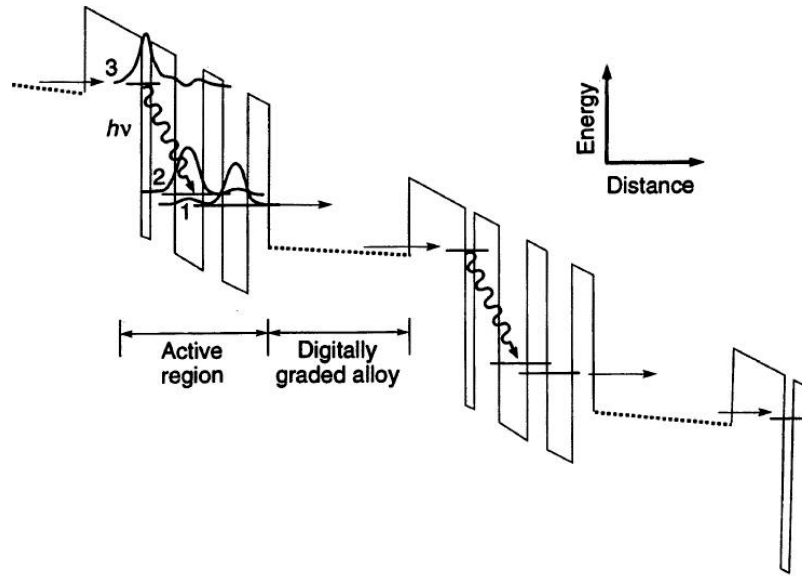


Figure 6.4 Band diagram of the first quantum cascade laser reprinted from Ref. 1. The structure is aligned for an applied electric field of about 95 kV/cm. Note the diagonal nature of the radiative transition in real space and the energy distance of one LO phonon between states 1 and 2. The digitally graded alloy is where the doping resides¹⁰⁹ (reprinted from ref. 109).

The photon energy can be tuned simply by varying the energy spacing between the levels of the QW, *i.e.*, by changing its thickness. Therefore the QCL can generate light with an extremely large frequency range: NIR, MIR, FIR and THz. In the MIR range, QCLs operating between 3.5 μm and 14 μm with high performance have been commercialized. For example, peak power levels are in the Watt range and the operation temperatures for all of these wavelengths can be above room-temperature (RT) for both pulsed and CW conditions.

6.2.2 The THz QCL active region design

In 2002 the first THz QC laser was reported at 4.4 THz (67 μm) by Köhler *et al.*¹¹⁰. The first demonstrated THz QCL generated only in pulsed condition with peak powers of a few milliwatts and ceased lasing above temperatures of several tens of Kelvin. At present,

the THz QCLs have been demonstrated in the spectral range of 0.84–5.0 THz^{137,138}. The maximum temperatures under the pulsed/CW operation have been achieved up to 220 K/117 K, respectively¹³⁹. The maximum output powers under the pulsed/CW operation have been achieved up to 250 mW/130 mW, respectively¹⁴⁰. Fig. 6.5 illustrates a survey reprinted from Ref. 111 of the temperature power performance for various types of active regions reported in the literature. The highest operating temperatures are achieved by designs based on resonant-phonon (RP) design. The design of each active region will be briefly introduced in the following text.

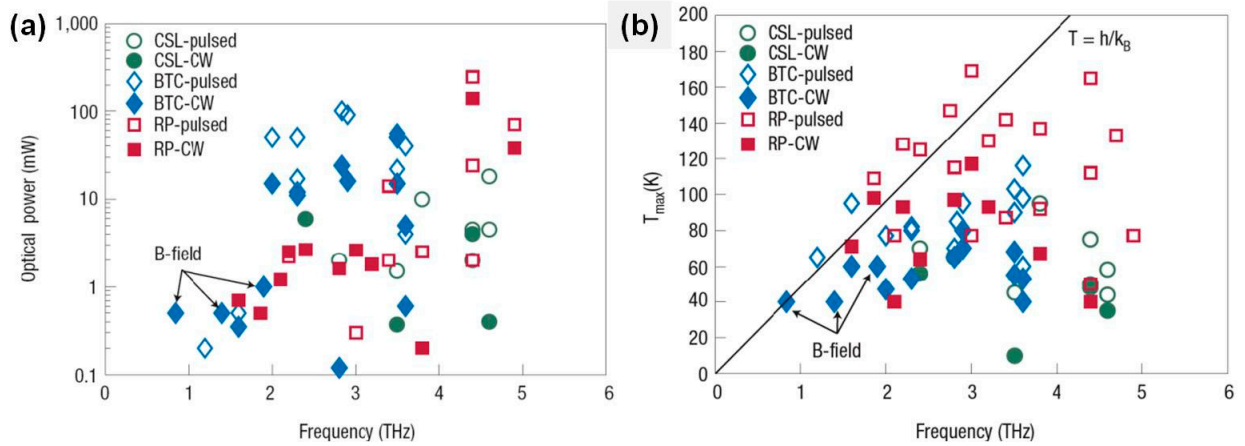


Figure 6.5 Survey of the reported peak performance of THz QC lasers. (a), Peak optical power and, (b), peak operating temperatures are shown as a function of lasing frequency. Data are sorted by pulsed or CW performance and active-region design: resonant-phonon (RP), bound-to-continuum (BTC) or chirped superlattice (CSL). Several of the low-frequency designs operate with the assistance of a magnetic field (B-field)¹¹¹ (reprinted from ref. 111).

The design and full examination of the THz QCL active regions are far beyond the scope of this thesis. Nevertheless, we can cite the major THz QCL active region designs as examples to understand the basic working principles behind. The active regions of the QC lasers are commonly grown by MBE in the GaAs/Al_xGa_{1-x}As multiple-QW material system. Three major THz active region designs are shown in Fig. 6.6 and will be briefly introduced here: chirped superlattice (CSL) design, bound-to-continuum (BTC) design and resonant-phonon (RP) design. Their correspondent conduction-band diagrams are plotted in Fig. 6.6. The chirped superlattice demonstrated by Tredicucci *et al.* in 1998¹⁴¹ and the bound-to-continuum demonstrated by Faist *et al.* in 2001¹⁴² both show very good performances originally at low photon energies in the Mid-IR. They can be also used in the realization of THz QCL.

The CSL design, shown in Fig. 6.6(a), is based on the inter-miniband transitions¹⁴³, where the applied electric field is compensated by the quasi-electric field resulting from a gradually varying (chirped) superlattice (SL)¹⁴⁴ period length and average composition. In this way “flat” minibands can be obtained without the need for dopants, which would

broaden the optical transition and spoil population inversion at high temperatures¹⁴⁵. The optical transition (black arrow in Fig. 6.6 (a)) takes place from the lowest state of the upper miniband '2' to the top state of the lower miniband '1'. The population inversion is sustained also at high temperatures because of the scattering of electrons between the tightly coupled states within the miniband (intra-miniband scattering) and is favored over inter-miniband scattering. Thus electrons tend to relax to the bottom of the minibands, leaving the lower radiative state relatively empty. This avoids the backfilling problem that can affect structures based on resonant tunneling for extraction of the carriers.

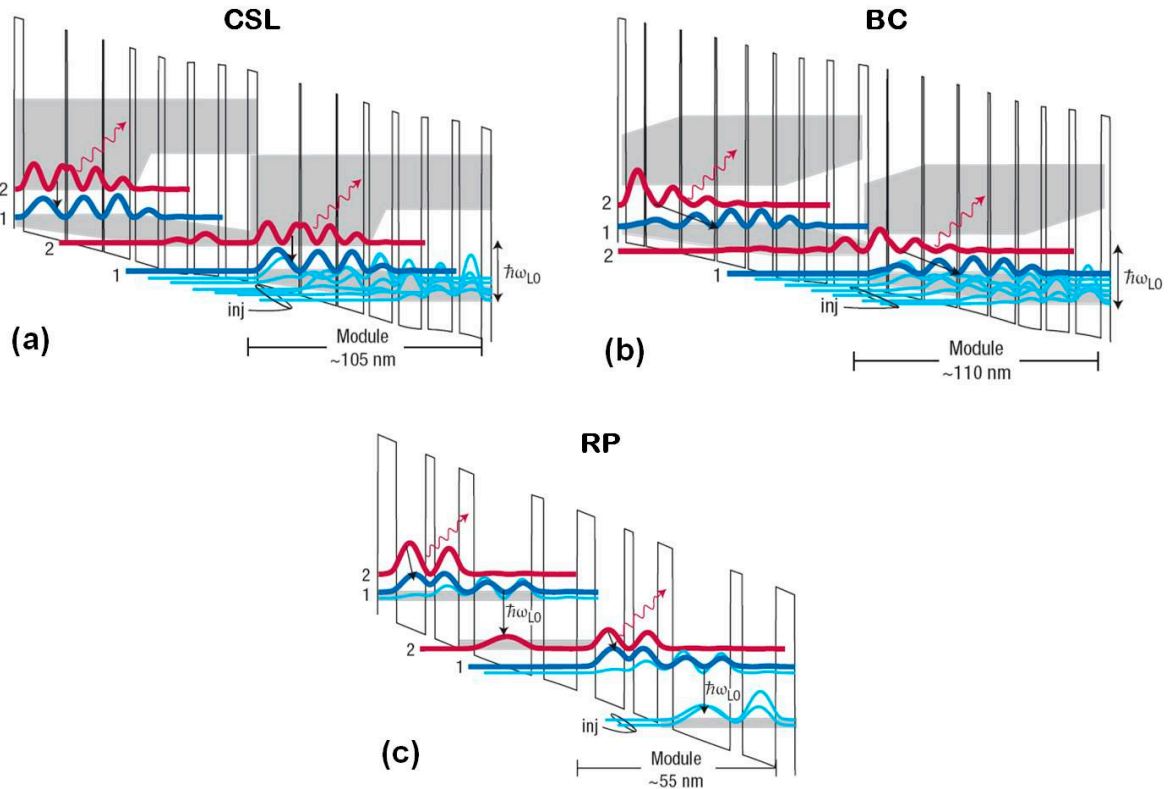


Figure 6.6 Conduction-band diagrams for major THz QC design schemes. Examples are shown for: a, CSL, b, BTC, c, RP and d, hybrid/interlaced designs. Two identical modules of each are shown here, although typically 100–200 cascaded modules are grown to form active regions 10–15- μm thick. The squared magnitude of the wave functions for the various subband states are plotted with the upper- and lower-radiative states shown in red and blue respectively and the injector states specifically labeled. The grey shaded regions correspond to minibands of states¹¹¹ (reprinted from ref. 111).

The bound-to-continuum (BTC) transition, whose band diagram is shown in Fig. 6.6(b), is a high performance design based on a superlattice design. The lower radiative state and miniband-based depopulation remains the same as in CLS design, but the upper radiative state is an isolated state ('defect' state) in the minigap^{142, 146}. Inserting a thin well can create such a state adjacent to the injection barrier, while electron extraction occurs through a lower miniband. The laser transition is diagonal in real space, which maximizes

both the injection efficiency and lifetime ratio (upper to lower state). The miniband transport is employed as an efficient extraction mechanism to minimize the lower state population. As a result, these designs displayed improved temperature and power performance compared with the CSL designs (see Fig. 6.5).

The Resonant-phonon-assisted (RP) scheme, shown in Fig. 6.6(c) is a robust depopulation mechanism even at high temperatures. Mid-infrared QCLs also use LO-phonon scattering for depopulation, while for THz lasers, the development of THz QCLs turned out to be much more difficult than initially expected. It was difficult to use LO-phonon scattering to depopulate the lower radiative state without also depopulating the upper state, because of the narrow subband energy spacing (~ 10 meV). The selectivity of the depopulation scattering on the desired radiative state is achieved through a combination of resonant tunneling and LO-phonon scattering, hence the term **resonant phonon**. Collector and injector states are designed to be below the lower radiative state '1' by approximately $E_{LO} = 36$ meV, so that electrons in the lower state scatters immediately into the injector states by emitting an LO-phonon. The RP scheme allows a highly selective depopulation of the lower radiative level with a sub-picosecond lifetime, while maintaining a relatively long upper level lifetime (>5 ps) that is due to upper-to-ground-state scattering. The RP scheme is widely used to achieve high operating temperatures and high output powers.

6.2.3 THz waveguides

A good waveguide for THz light source should possess the following two features: low loss and high overlap between of the optical field and the active material. Standard dielectric waveguides cannot be used for THz QCL due to the poor confinement factor. Moreover, as losses due to the absorption of radiation by free carriers increase proportionally to the square of the wavelength, waveguides that minimize the modal overlap with any doped semiconductor cladding layers are preferred. At present, there are two types of waveguides used for THz QC lasers: the semi-insulating surface-plasmon (SP) waveguide and the double-plasmon (DP) waveguide (also called metal-metal (MM) waveguide). Their schematic illustrations are shown in Fig. 6.7(a) and 6.7(c), respectively.

The first demonstrated THz QCL made use of a semi-insulating SP waveguide to confine the optical mode. It suffers heavily from the high optical losses and poor overlap ($\Gamma \sim 0.1$ – 0.5 , shown in Figs. 6.7(a) and 6.7(d) of the mode with the active region, especially long wavelength. Alternatively, DP waveguide can provides mode confinement factor close to unity ($\Gamma \sim 1$, shown in Fig. 6.7(c) and 6.7(e)), with reduced optical losses and improved temperature performance, especially at long wavelengths. However, there are two drawbacks of DP waveguide comparing with SP due to the large mode mismatch: one is

lower output power (more loss in metal layers), another one is a poor beam emission diagram in the far field (strong confinement caused high divergence).

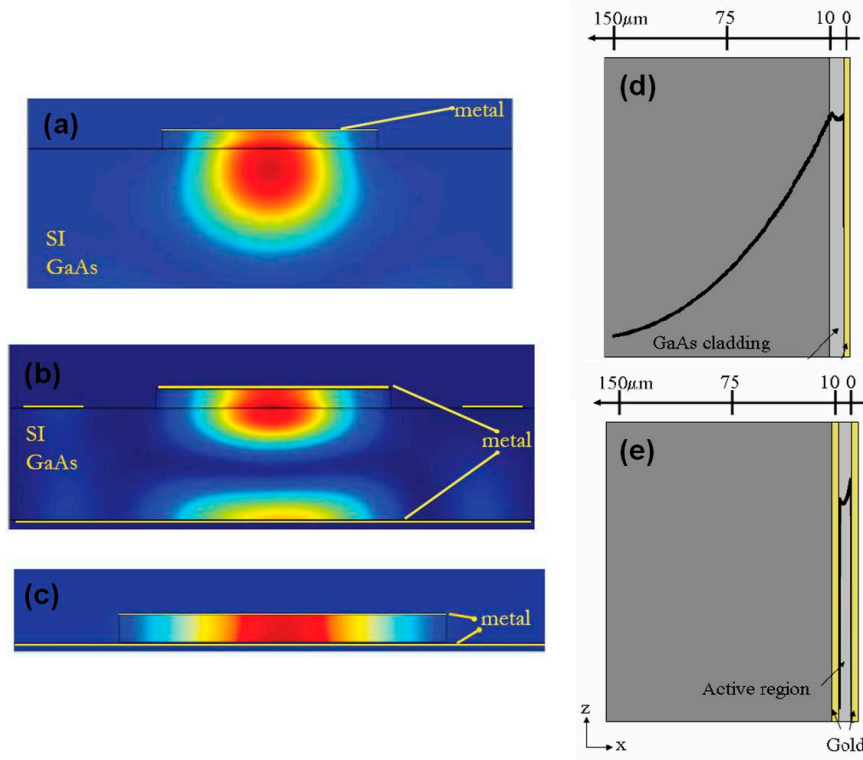


Figure 6.7 Overview of the THz QCL waveguides. (a) Computed mode intensity for a single plasmon waveguide at 3 THz (200 μm wide, 17 μm thick). (b) Computed mode intensity for a 200 μm wide, single plasmon waveguide at 1.9 THz with a 600 nm thick buried layer. (c) Computed mode intensity for a double-metal waveguide 200 μm wide and 17 μm thick at 950 GHz¹¹². Schematic representation of (d) single - and (e) double -metal THz QCL waveguides. The component of the magnetic field of the mode parallel to the layers of the active region (H_y) is plotted¹⁴⁷ (reprinted from ref. 112 and 147).

6.3 Fabry-Perot (FP) laser and Distributed feedback (DFB) laser

The earliest diode lasers were all Fabry-Perot (FP) lasers, which remains an important class of general-purpose lasers. A simple optical resonator is formed when two partially reflecting mirrors are placed facing each other. Let L be the separation between the two mirrors. If the spacing between the two mirrors is filled with a medium that has gain, an FP laser is formed (as shown in Fig. 6.8 (a)). The wave is amplified as it passes through the laser medium as an electric wave propagates back and forth between the partially reflecting mirrors. If the amplification exceeds other cavity losses owing to imperfect reflections from the mirrors or scattering in the laser medium, the field energy inside the cavity will continue to build up. When the gain balances the loss, a self sustained oscillator or a laser cavity is formed. The spectrum of the FP laser in general shows multiple modes with frequencies determined from the phase condition giving a mode

spacing, which depends on the group index for the optical fields in the waveguide. Fig. 6.8 (b) gives a typical spectrum for a FP laser operating at a central wavelength of around 1.55 μm showing these features.

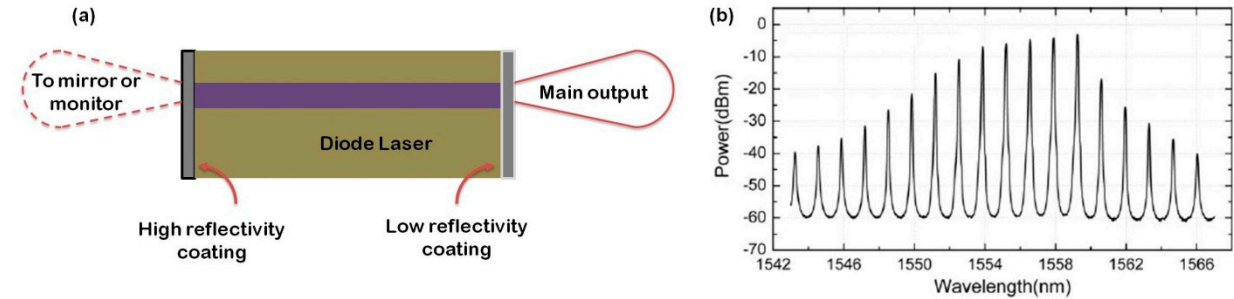


Figure 6.8 Overview of the Fabry-Perot laser. (a) Schematic of a FP diode laser (b) Power spectrum for a FP laser operating at a central wavelength of around 1.55 μm ¹⁴⁸ (reprinted from ref.148).

The FP laser has a limited performance. In an optical integrated circuit where the laser diodes are monolithically integrated within the semiconductor wafer, it is usually very difficult to form such reflecting surfaces. Etching or cleaving of the wafer can form the reflecting surfaces. However, the planar surface of the wafer is then disrupted, which leads to difficulties in fabricating electrical connections. An alternative approach, which utilizes distributed-feedback (DFB) from a Bragg-type diffraction grating, provides a number of advantages while still utilizing a planar surface geometry¹⁴⁹.

A device with a uniform grating is usually known as a distributed-feedback (DFB) laser. As indicated schematically, the concept of a uniform distributed feedback laser is shown in Fig. 6.9, with distributed reflections and gain within the laser cavity, an optical wave travelling in one direction is continuously scattered into the optical wave in the reverse direction. Both waves grow as they travel towards their respective facets because of the feedback and gain.

To understand the operational characteristics of a DFB semiconductor laser, it is necessary to consider wave propagation in periodic structures. Grating or corrugation-induced dielectric perturbation leads to coupling between the forward and backward propagating waves. Coupled-wave theory¹⁵⁰ and Bloch wave analysis¹⁵¹ have been developed. Here, coupled-wave theory is used due its ease of understanding. The coupled-wave theory is based on the vector wave equation for the electric field

$$\frac{\partial^2}{\partial z^2} \mathbf{E} + k^2 \mathbf{E} = 0 \quad (6.1)$$

Where \mathbf{E} is the complex amplitude of a field of angular frequency ω , which is assumed to be only dependent of the z coordinate (point in the direction of propagation). The constants of the laser medium also vary periodically as a function of the z coordinate. We assume a spatial modulation of the refractive index $n(z)$ and of the gain constant $\alpha(z)$

$$n(z) = n + n_1 \cos 2\beta_0 z, \quad (6.2.1)$$

$$\alpha(z) = \alpha + \alpha_1 \cos 2\beta_0 z, \quad (6.2.2)$$

where n and α are the average values of the parameters of the medium and n_1 and α_1 are the amplitudes of the spatial modulation. The propagation constant of the wave is β_0

$$\beta_0 = n\omega_0/c, \quad (6.3)$$

ω_0 is the Bragg frequency. With the assumptions discussed in ¹⁵⁰, the k vector in equation 6.1 can be written in

$$k^2 = \beta^2 + 2i\alpha\beta + 4\kappa\beta \cos 2\beta_0 z, \quad (6.4)$$

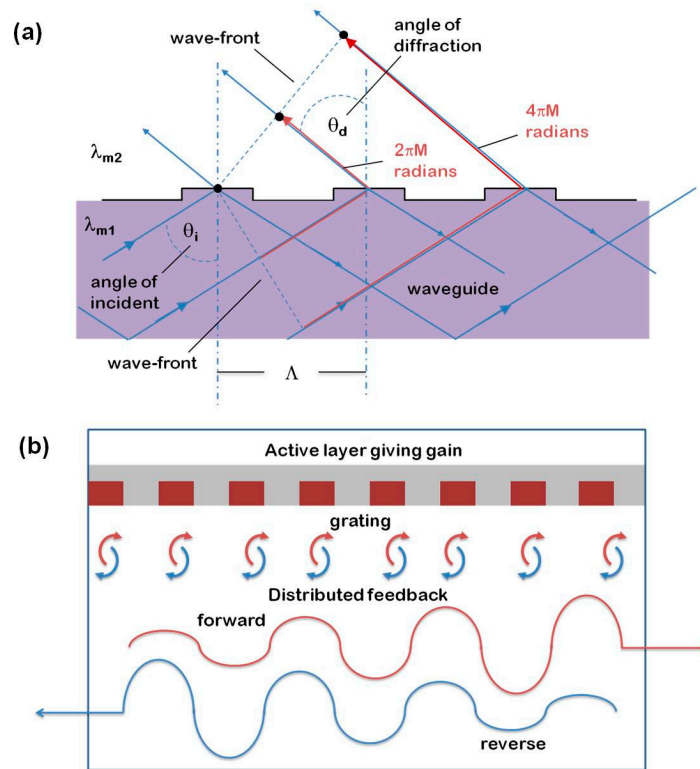


Figure 6.9 Working principles of distributed feedback laser. (a) Diffraction from a grating embedded in a laser waveguide. (b) Uniform distributed feedback laser: the concept of continuous feedback combined with gain.

And the coupling constant is defined by

$$\kappa = \frac{\pi n_1}{\lambda_0} + i \frac{\alpha_1}{2} \quad (6.5)$$

It describes the feedback provided by the structure per unit length, which is a key parameter of the coupled-wave theory. As shown in Fig. 6.9b, the two significant waves in the DFB structure are two counter-propagating waves R and S. These waves grow because of the presence of gain and they feed energy into each other due to Bragg scattering. They can be described by the complex amplitudes $R(z)$ and $S(z)$. The electric field can be expressed as

$$E(z) = R(z)e^{-i\beta_0 z} + S(z)e^{i\beta_0 z} \quad (6.6)$$

Equation 6.6 can be input in the wave equation 6.1. As these waves are varying slowly, all the terms higher than the first order derivatives can be neglected. Therefore, a pair of coupled-wave equations can be obtained

$$-R' + (\alpha - i\delta)R = i\kappa S \quad (6.7.1)$$

$$S' + (\alpha - i\delta)S = i\kappa R \quad (6.7.2)$$

Where $\delta \approx \beta - \beta_0 = n(\omega - \omega_0)/c$. If we consider a DFB laser of length L (extending from $z = -L/2$ to $z = L/2$). The boundary condition for the wave amplitudes are

$$R_{(-\frac{L}{2})} = S_{(\frac{L}{2})} = 0 \quad (6.8)$$

This boundary condition together with the coupled-wave equations 6.7 describes the electromagnetic field in the DFB laser. The general solution to the coupled-wave equations 6.7 is

$$R = r_1 e^{\gamma z} + r_2 e^{-\gamma z} \quad (6.9.1)$$

$$S = s_1 e^{\gamma z} + s_2 e^{-\gamma z} \quad (6.9.1)$$

Where γ is the complex propagation constant obeying the dispersion relation

$$\gamma^2 = \kappa^2 + (\alpha - i\delta)^2 \quad (6.10)$$

Due to the assumed symmetry of the device [symmetric $E(-z)=E(z)$ and antisymmetric $E(z)=-E(-z)$] and the boundary condition equation 6.8

$$r_1/r_2 = s_2/s_1 = -e^{\gamma L} \quad (6.11)$$

For each value of γ , we have a corresponding threshold gain constant α and a resonant frequency δ and we can obtain the relation

$$\gamma + (\alpha - i\delta) = \pm i\kappa e^{\gamma L} \quad (6.12.1)$$

$$\gamma - (\alpha - i\delta) = \mp i\kappa e^{\gamma L} \quad (6.12.2)$$

This solution of the coupled-wave equation provides the (threshold) modes of the DFB laser. For a given length and coupling, each mode has its field pattern, threshold gain and resonance frequency, which are key parameters of the laser device.

Another important issue of DFB laser is phase matching. A DBR laser operates at the Bragg frequency of the grating where there is maximum reflection. It is possible to ensure that the round-trip phase matching occurs, as in a Fabry-Perot laser, if the two reflectors are identical mirror versions of each other with a real reflection with the same sign, and that these reflectors are separated by a central section of length N times $\lambda_0/2$. The shortest possible Fabry-Perot section is $\lambda_0/2$ ($N=1$) and this requires the insertion of an additional $\lambda_0/4$ into the lower refractive-index region to form a length $\lambda_0/2$ between two mirrored sections of a DFB laser. There are also other complex phase-adjusting methods detailed in literature ^{149, 152, 153}.

A number of DFB laser experiments have been reported since the initial work of Kogelnik *et al.* ¹⁵⁰ using different laser materials in unique experimental configurations. Following this, in 1997, the first quantum cascade distributed-feedback laser (QCDFB) with a grating close to the active region was reported by Faist *et al.* at both 5.4 and 8 μm wavelengths ¹⁵⁴. Here, the grating in a refractive index-dominated coupling scheme provides the feedback.

6.4 Photonic crystal THz lasers

PhCs are recently receiving a lot of attention because of their capacity to act as ideal mirrors and to strongly confine light by means of the photonic band gap. This is due to the fact that Bloch waves have an intrinsic feedback mechanism near the band edge. From the device point of view, the feedback mechanism can be compared with that of the conventional 1D distributed feedback lasers. With 1D DFB lasers, the feedback is simply the result of the coupling of two counter-propagating modes. In contrast, 2D or 3D PhCs lasers would have a variety of feedback mechanisms due to their extended degree of freedom, and the feedback should reflect the character of each photonic band gap.

2D DFB (PhC DFB) lasers were reported theoretically and experimentally in different groups ¹⁵⁵⁻¹⁵⁷. In 2001, I. Vurgaftman and coworkers reported the far-field emission characteristics and the spectral purity of photonic-crystal distributed-feedback lasers, in which the grating is defined on a two-dimensional lattice that is tilted with respect to the facets and their results are analyzed using a self-consistent time-domain simulation. It is shown that both conventional DFB and angled-grating DFB devices are special cases of the PCDFB laser, which combines and enhances the best features of each of them. They also theoretically investigate the beam quality and spectral purity of gain-guided PhC DFB quantum cascade lasers. By searching the parameter space consisting of

tilt angle, coupling coefficients, stripe width, and cavity length, they have successfully optimized the 2D DFB gratings for QCL gain regions. They also examine the tolerances required for single-mode and high-brightness operation.

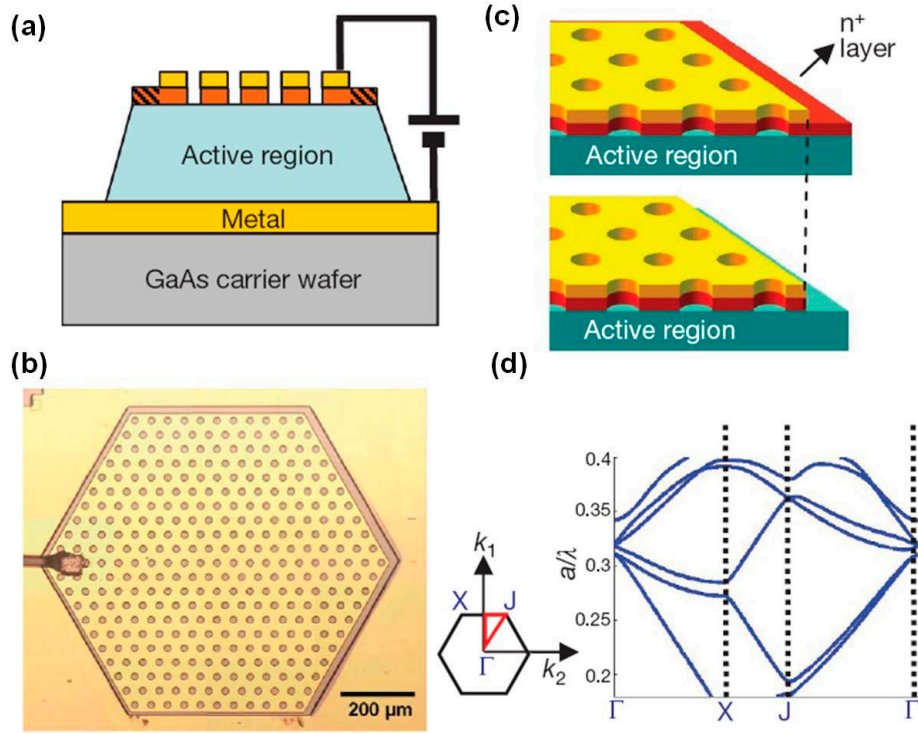


Figure 6.10 Device details and design. *a*, Schematic cross-section of the device. The laser active region (blue) is sandwiched between two metal Ti/Au contact layers. The top metal is patterned with the desired photonic-crystal design. *b*, Optical microscope image of the surface of a typical device. The wire bonding is applied directly on the top metallization. *c*, Detailed scheme of the boundary conditions implementation technique. When the top n^+ contact, represented as a red layer, is left in place between the metal edge and the mesa periphery (top panel), the absorption is high and the boundary behaves like an absorber. *d*, TM photonic band structure of the triangular lattice used for the experiment, for $r/a = 0.22$ ¹¹⁴ (reprinted from ref.114).

Photonic band engineering has been proved to be a highly efficient way for manipulating the emission properties of semiconductor lasers. Thanks to the scaling law between wavelength (λ) and lattice constant (a) of PhCs, concepts of PhC semiconductor lasers can be exploited at any frequency. In THz frequency range, THz cascade structures are extremely well suited for their use in PhC structures. PhC lasers can be summarized in two groups, one is the PhC defect mode laser based on a resonant cavity mode, the other is the band-edge DFB laser, either one (1D) or two-dimensional (2D). Most of the important works of THz PhC lasers belong to the second group. In this section, several works will be reviewed for better understanding of our own design.

THz QC laser based on weak PhC effect has been demonstrated with low index modulation structures that are obtained by patterning the top metallic layer of the laser

while leaving the active region unetched. Chassagneux and his co-workers produced evidence that whispering-gallery-like modes or true photonic-crystal states can be alternatively excited ¹¹⁴ by demonstrating a general technique to implement reflecting or absorbing boundaries. As shown in Fig. 6.10, they illustrate the power of this technique by fabricating photonic-crystal terahertz (THz) semiconductor lasers lasing at the partial photonic band edge Γ point, where the PhC is implemented via the sole patterning of the device top metallization. Single-mode laser action is obtained in the 2.55–2.88 THz range, and the emission far field exhibits a small angular divergence, thus providing a solution for the quasi-total lack of directionality typical of THz semiconductor lasers based on metal-metal waveguides. This work had shown that boundary conditions are a key parameter for the effective design and implementation of active, electrically injected photonic devices. The application of this idea to a class of semiconductor THz lasers where the photonic-crystal structure has been ‘written’ on the top metallization layer yielded lithographically tunable, single-mode operation and angularly narrow surface emission.

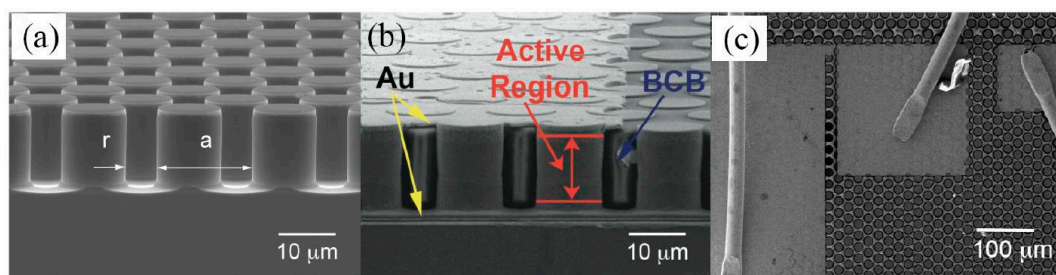


Figure 6.11 Scanning Electron Microscope (SEM) images of pillar type THz PhC lasers. a, Cross-section SEM image of PhC pillars after dry etch ($\sim 15.5 \mu\text{m}$). b, Side view SEM image of double metal configuration bounding the PhC pillars which are surrounded by BCB. c, Top view SEM image of PhC tile lasers (lengths of square top contacts are $600 \mu\text{m}$, $200 \mu\text{m}$ and $100 \mu\text{m}$) with $25 \mu\text{m}$ diameter bonded gold wire ¹¹³ (reprinted from ref. 113).

The strong PhC effect, which requires a high index modulation, can be achieved with deeply etched structures, which are sandwiched within the two metallic layers. In 2007, Hua and his co-workers (EPFL) combined PhC and quantum cascade band engineering to create an in-plane laser at terahertz frequency (Fig. 6.11) ¹¹³. They demonstrated that such PhC lasers strongly improve the performances of terahertz quantum cascade material in terms of threshold current, waveguide losses, emission mode selection, tunability and maximum operation temperature. The laser operates in a slow-light regime between the M saddle point and K band-edge in reciprocal lattice. Coarse frequency control of half of a terahertz is achieved by lithographically tuning the PhC period. The field assisted gain shift and cavity pulling allows for the single mode emission to be continuously tuned over 30 GHz.

Compared to near infra-red PhC band-edge lasers, achieving vertical emission with quantum cascade material operating in the THz range needs dedicated engineering because

the TM polarized emission of QCLs favors in-plane emitting schemes and the currently used double plasmon waveguide, prevents vertical light extraction. In 2011, Hua and his co-workers presented an approach with independent refractive index and extraction losses modulation¹⁵⁸. The extraction losses are obtained with small extracting holes located at appropriate positions (in Fig. 6.12).

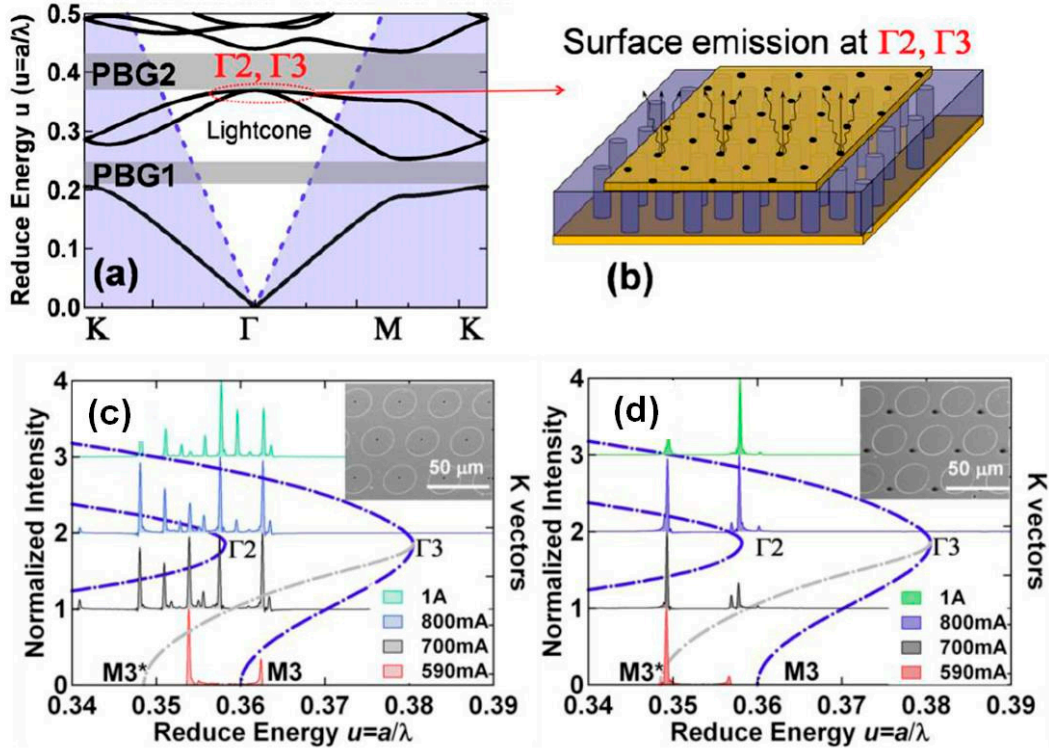


Figure 6.12 Design and spectral characterizations of pillar type vertically emitting PhC quantum cascade lasers. (a), PhC dispersion curves calculated by 2D Plane wave expansion, several complete bandgaps are observed (semi-transparent gray shadows, e.g. PBG1 and PBG2). Blue dashed lines indicate the light light. Red dashed circle locates the two slow light band-edge states of interest (Γ_2 , Γ_3). The pillar filling factor (ff) is 40%. (b), Sketch of the surface emitting lasing scheme at the band-edges (Γ_2 , Γ_3). The pillar height is about $15 \mu\text{m}$ and the lattice constant range is between 32 and $40 \mu\text{m}$. (c) and (d), Dispersion curves and lasing spectra of elliptical pillar-type photonic-crystal lasers at lattice constant $a = 32 \mu\text{m}$, with holes on pillars and holes on BCB configurations, as shown insert SEM images for (c) and (d), respectively¹⁵⁸(reprinted from ref. 158).

The laser operates in a slow-light regime at 2nd and 3rd band-edge Γ points in the reciprocal lattice. The Γ point around PBG2 of the circular pillar structure is doubly degenerate. As these two bands exhibit different slow light enhancement factors, such a configuration is a recipe for poor modal control, especially in a system like QC active material. Here, an inhomogeneously broadened gain is experienced and the mode degeneracy can be lifted in an uncontrolled manner by any residual fabrication disorder or anisotropy. This can be solved with a complex engineering of the extractor with additional losses to prevent lasing on the undesired states. Such an approach presents the drawback

of an increased lasing threshold. Alternatively, PhC engineering can be used to lift the degeneracy with a sufficiently large frequency splitting. This latter case was used in this work. As shown in Fig. 6.12 (c) and (d), an elliptical pillar type PhC device was used to provide a sufficiently large frequency splitting. The modal operation of the PhC is shown to critically depend on the external losses introduced. A very high surface emission power for an optimum loss extractor design is achieved. Such an approach can be used as a general tool for the development of both electrically and optically pumped devices at any frequency based on index modulation devices. However, results of this work showed limited optical performance in terms of far field pattern, CW operation and mode control. Further investigation has to be performed before proceeding towards real world applications.

6.5 Continuous-wave vertically emitting THz laser

As reviewed in the previous section, different strategies like PhC or metallic grating DFB patterning for in plane or vertical emission are demonstrated in THz QC lasers. Devices with monochromatic, highly directional, vertical emissions with low threshold current density (J_{th}) and high T_{max} have been achieved^{113-115, 158-160}. However, most of these progresses are demonstrated in pulsed operation mode. CW operation performance is still limited and far from optimization, despite the fact which of crucial demand in astrophysics, biology, sensing, environmental and pollutant monitoring, and security screening. In this section, key results of our work will be detailed.

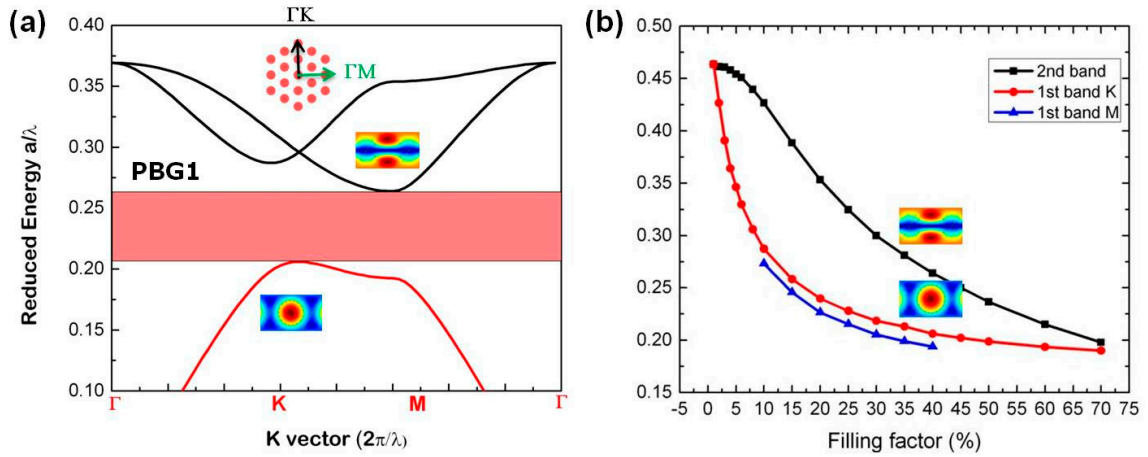


Figure 6.13 Left: Plane wave expansion (PWE) method calculated dispersion of the TM modes for triangle lattice, filling factor is 40% (circular pillars). Right: Photonic band gap as a function of filling factor. Insets are calculated E_z field distributions of 1st and 2nd band edge modes.

For most of the QC lasers in THz range, slope efficiency and wall plug efficiencies are lower than 30mW/A and 0.2%¹⁶¹, respectively. Therefore, the main part of the input power is wasted and converted into heat. CW operation of QC lasers is basically limited by the heat dissipation in the device. In order to improve the CW laser operation, one can

work on two aspects: i) optimize the heat flow inside the laser device and ii) reduce the J_{th} to minimize the total generated heat ¹⁶². None of them were successfully achieved in early works. Both the PhC QC laser and metallic grating DFB laser need an absorbing boundary condition for better operation performance. Energy dissipated at the boundaries will not contribute to the lasing emission. This effect subsequently limits the CW performance of the lasing device.

In Fig. 6.13 (a), plane wave expansion (PWE) method is used to calculate TM polarized dispersion curve and the electric field distribution of the band-edge mode for triangle lattice. In our past works, PhC 1st band edge in-plane emission and PhC 3rd band edge vertical emission QC lasers showed the advantages of PhC approaches in terms of single mode operation, reduction of losses and better pumping efficiency ^{113, 158}. However, filling factors used in the device are limited above 40%. The strong PhC confinement for in-plane radiation propagation maintains down to filling factor of 10%. This can be clearly observed in the figure of photonic band gap as a function of filling factor (Fig. 6.13 (b)). In fact, lower filling factor has important effects on the CW performance of PhC THz devices.

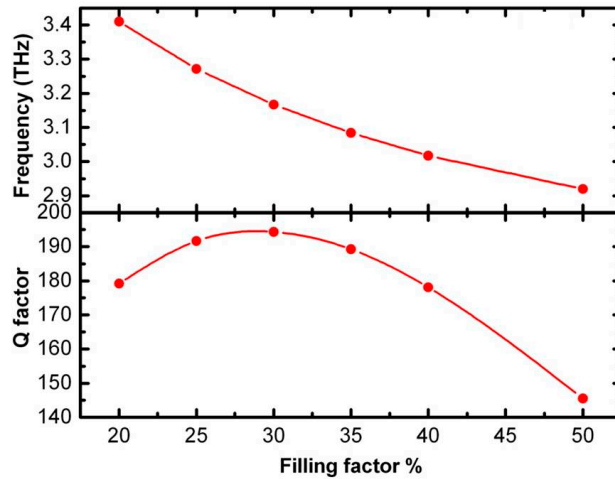


Figure 6.14 3D FEM solver (COMSOL) computation of losses and frequencies of the 1st band-edge mode change with filling factors.

In order to qualitatively estimate how the filling factor influences the photonic band edge mode, theoretical computations are performed with a 3D FEM solver (COMSOL). The losses of the first photonic band-edge modes are computed with different filling factors. Losses in the gold waveguide layer and gain in the QC layer have been taken into account in the computation. A minimum of losses is observed at filling factor 30% (as shown in Fig. 6.14). Two effects are simultaneously occurring in the device for this case. On one hand, the free carrier absorption is proportional to λ^2 . Frequencies of band edge modes are decreasing with the increasing of filling factors. Therefore, losses are increasing with the increasing of filling factors. On the other hand, the overlap between electric field

distributions of band-edge modes and active gain medium is proportional to the filling factor. The first (second) effect dominates when the filling factor is higher (lower) than 30%, respectively. Based on this estimation, three different filling factors around 30% are selected (20%, 30% and 40%). Depending on the overlap between the gain bandwidth of different lattice constant and the photonic band dispersion of different filling factor, lattice constants of different fill factors are properly selected (Fig. 6.15).

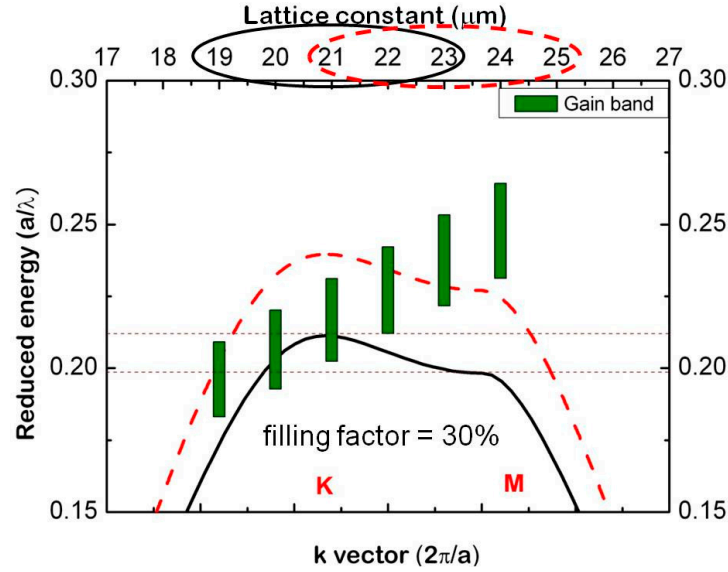


Figure 6.15 Gain band widths (in reduced energy) of different lattice constant on photonic band dispersion curve. Dispersion curves of 30% and 40% filling factor are in black (solid line) and red (dash line). Gain band widths of lattice constants from 19 to 24 μm are represented in solid green bar.

In previous reports, PhC 1st band edge in-plane emission and PhC 3rd band edge vertical emission QC lasers have demonstrated the advantages of PhC approaches in term of single mode operation, reduction of losses and better pumping efficiency^{113, 158}. Compared to other PhC QC lasers, which only have PhC structures in the top metal layer, similar methods also used in this work bring three main advantages. Firstly, the in-plane propagation of an electromagnetic wave experiences a two-dimensional (2D) PhC modulation provided by the high index mismatch (refractive index contrast 1.90: 3.45). This modulation results in an effective PhC gain enhancement of the band edge mode and improves the monochromatic operation of the device. Secondly, the mode at the first band edge K point is a dielectric band edge mode. The major fraction of the electric field is distributed inside the high dielectric constant media consisting of QC pillars. A lower area of QC active material is pumped (filling factor FF of 20% or 30%) which results in an improvement of the electrical pumping efficiency. Thirdly, by filling the empty volume between QC pillars with low loss (3 cm^{-1} at 3.1 THz and 300 K) Benzocyclobutene (BCB)¹⁰, the surface to volume ratio and heat flow inside the device are improved by diluting the active region without significantly increasing the total loss¹⁶³. In the present work, the loss

type boundary conditions, which have been used in PhC and DFB QC laser^{114, 164} is replaced by a second order Bragg grating. This grating has multiple-functions. As a second order Bragg grating, it can diffract TM polarized in-plane radiation at the required frequency into vertical emission. More importantly, instead of absorbing the radiation at the boundary, to ensure the single mode operation this Bragg grating scatters them into desired vertical emission. As a consequence, this design shows significant improvement for CW operation in terms of maximum output power and T_{\max} .

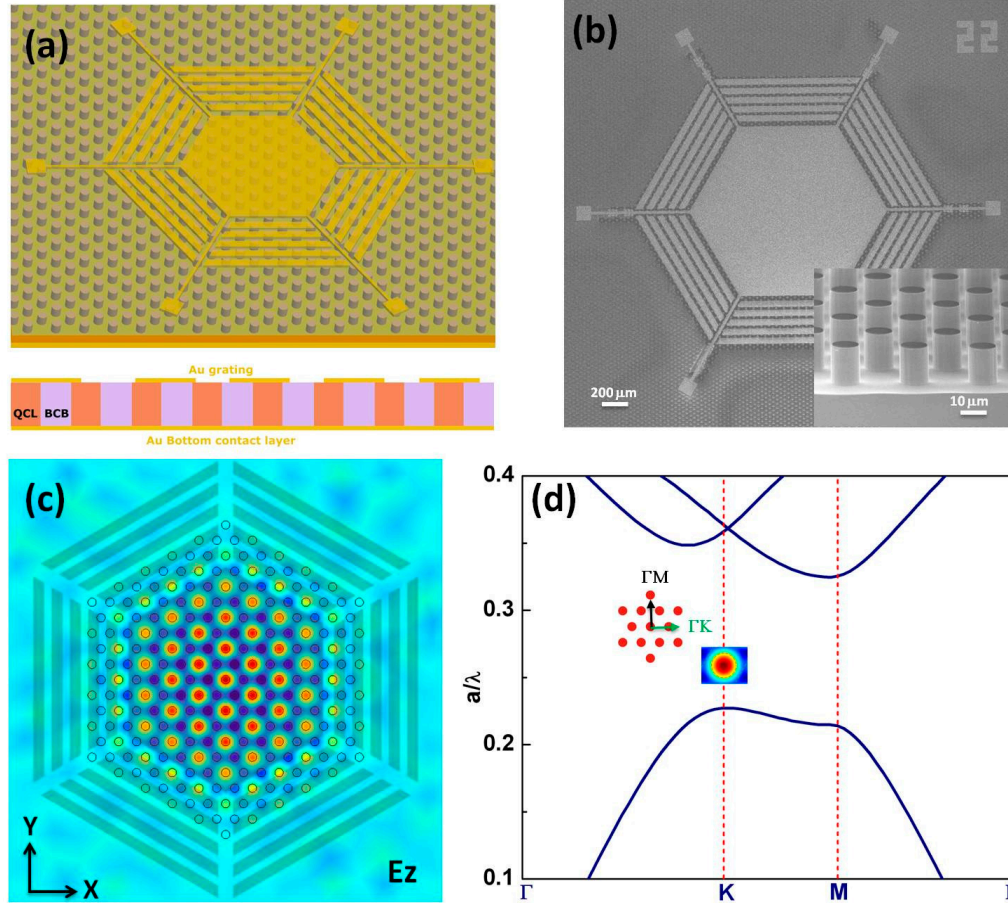


Figure 6.16 Device details and design. *a*, Schematic 3D view of the device. *b*, Scanning electron micrograph of a typical device. *c*, In plane electric field distribution of the device with 3D finite element methods (COMSOL). *d*, Transverse magnetic photonic band structure of the triangular lattice used in the design.

The QC laser used in this work has a GaAs/AlGaAs material with hybrid of resonant phonon and bound to continuum scheme. This 11 μm thick active layer operates at 3.1 THz with a gain band width of 0.6 THz. 2D triangular PhC patterns are defined in the QC active layer by inductively coupled plasma (ICP) dry etching (Fig. 6.16). The first PhC band edge K point mode frequency is chosen by appropriately selecting the lattice constant a and filling factor (Fig. 6.15). Ultra smooth surface (less than 0.3% roughness) and a nearly perfect

vertical side wall (vertical angle 89.9°) of the QC pillars can be observed in the inset scanning electron microscope (SEM) image of Fig. 1b. This is a critical factor in reducing the scattering and absorption losses due to the structural imperfections inside the device as much as possible.

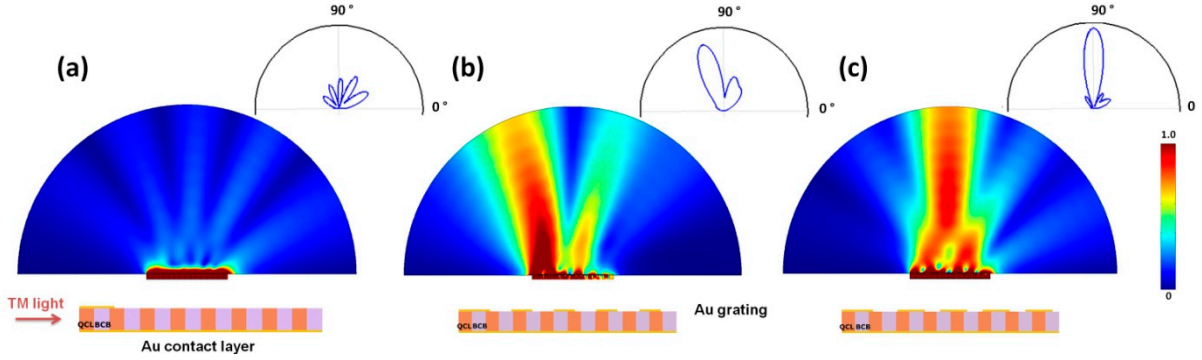


Figure 6.17 Effect of the Bragg extractor. a, Distribution of the electric field norm of the device without Bragg extractor. b, Distribution of the electric field norm of the device with standard Bragg extractor. c, Distribution of the electric field norm of the device with optimized Bragg extractor. For each figure, inset is the polar plot of the electric field norm (amplitude in inset of figure a has been multiplied by a factor of 2).

The vertical field confinement of the QC laser is achieved by a $1\ \mu\text{m}$ thick bottom Au layer by means of thermo-compressive gold-gold wafer bonding and a $1\ \mu\text{m}$ thick top contact Au layer by means of electron beam evaporation and lift-off. The hexagonal central pad corresponds to the hexagonal symmetry of the triangular lattice. The simulated electric field of the lasing mode has a centro-symmetric distribution at the edge of the central pumping pad with respect to the central pillar (Fig. 6.16c). Such in-phase radiation results in a constructive beam pattern in the far field. The device is electrically pumped via six centro-symmetric bonding pads ($70 \times 70\ \mu\text{m}^2$) which are $300\ \mu\text{m}$ away from the central pumping pad. A series of metallic absorbers (maximum absorbing frequency at $3.1\ \text{THz}$) are inserted in between the central pumping pad and the bonding pads to prevent feedback and uncontrolled THz emission from the six bonding pads. A new type of vertical emission extractor is designed so as to decrease the extra losses due to the absorbing boundary condition used in PhC QC lasers or DFB QC lasers. A second order Bragg Au grating is implemented in the ΓK direction (Fig. 6.16d) to select the radiation in this direction from any other directions (mainly in the ΓM). The parameters of this Bragg grating are defined by the Bragg condition: $m\lambda_B = 2n_{\text{eff}}\Lambda$ (λ_B is the Bragg wavelength, n_{eff} is the effective refractive index of the QC active layer, Λ is the period of the grating, $m = 1, 2, \dots$). Design of the 2nd order Bragg extractor was performed with the finite elements method (FEM). The 2D far field pattern of the devices with different configurations are compared (Fig. 6.17a, b and c: without extractor, with the standard Bragg extractor of 50% duty cycle and the optimized Bragg extractor of 62% duty cycle respectively) ¹⁴⁷. It can be seen that without the extractor, the limited part of the in-plane radiation which comes from the central pad is

scattered out-of-plane with a divergent beam pattern. Improvements can be observed with the standard 2nd order Bragg extractor, the scattered radiation has two parts which are 10 degrees away from the vertical direction. After optimization of Λ , duty cycle and distance from the central pumping pad to the extractor, a considerable part of the in-plane radiation is scattered into vertical emission. A high intensity central beam pattern with a divergence angle less than 10 degrees is achieved with the optimized Bragg extractor.

Characterization technology of THz photonic crystal QC lasers

All the fabricated PhC QC lasers were characterized within the collaboration of Prof. J. Faist's group in ETHZ. The characterization tools will be briefly introduced here, like light-current-voltage (LIV) and Fourier transform far-infrared spectral emission (FTIR) measurement. After the bottom contact deposition, the sample was then cleaved and mounted on a copper holder with conductive glue and bonded with 25 μm (diameter) gold wires. A helium cooled cryostat inside a nitrogen bath which allows the lowest temperature of 4 K is used to cool the QCL sample.

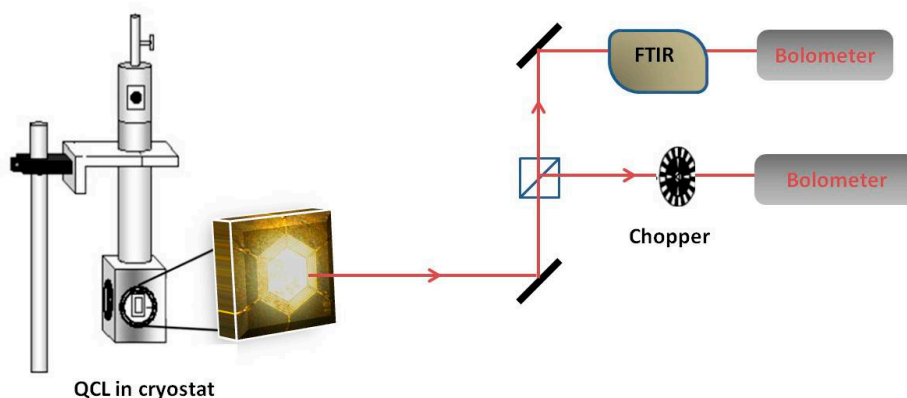


Figure 6.18 Illustration of THz spectra emission measurement setup with an example of surface emitting PhC laser. Radiation path is marked with dashed lines and wavy arrows.

For laser emission and power measurement (also called light-current-voltage measurement, abbreviated as LIV), a lightpipe is used to collect the THz emission from the laser facet/surface directly. The light is guided through a polyethylene window, and then a calibrated thermopile (Ophir, SH5) is used to perform the power measurement. For THz spectral emission measurements, a Fourier transforms infrared (FTIR) ^{165, 166} spectrometer has been used. The FTIR consists of a Michelson-Morley interferometer where the resolution is given by the optical path length difference between the two interfering light beams. For electroluminescence (EL) characterization, an under-vacuum home-made FTIR developed at ETHZ has been used. Under vacuum measurement are required because the

THz frequencies are strongly absorbed by water vapor¹³⁶ and the power emitted from the THz devices may be relatively low, which is difficult to be evaluated.

A step-scan technique, rather than continuous scan is used to increase the setup sensitivity²⁸. The electrical power is provided by a HP-8114A pulse generator, with typical 1 Hz to 15 MHz frequency range and 10 ns to 150 ms pulse width range. The injected current is measured using a calibrated current probe (Model 711 calibrated by American Laser Society). The probe is an electrical transformer placed around the injection current line. The current and the bias on the device are measured by a digital oscilloscope. A phase-sensitive detection scheme is employed, where a lock-in amplifier is synchronized with the pulse generator. Pyroelectric infrared detectors are used and the Noise Equivalent Power is in the $\mu\text{W}/\text{Hz}^{1/2}$ range.

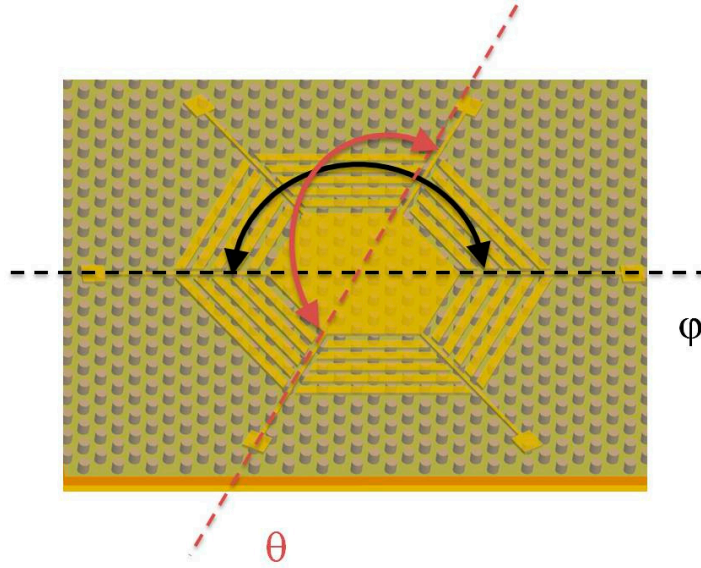


Figure 6.19 Illustration of THz spectra emission measurement setup with an example of surface emitting PhC laser. Radiation path is marked with dashed lines and wavy arrows.

For very low emitting powers, a bolometer, with NEP in the $\text{pW}/\text{Hz}^{1/2}$ range, is used to measure spontaneous emission. Liquid He-cooled Si bolometer is used. The bolometer is intrinsically a slow detector (slow response time) based on a thermal effect over large areas, therefore the injected current is modulated with low frequency long pulses at a repetition rate that matches the bolometer maximum recovery time ($1/\tau_{\text{Sibm}} = 416 \text{ Hz}$ for this Si bolometer). In order to prevent as much as possible device heating, trains of N micro-pulses with a repetition rate of $1/T$ with $NT = \tau_{\text{Sibm}}/2$ are produced. The maximum possible overall duty factor is 50%²⁸. The 50% duty cycle goes for pulses of 16.6ms which are long enough to be considered CW or sometimes called QCW, which is used for the CW measurements. Fig. 6.18 illustrates the THz spectra emission measurement setup with an example of surface emitting PhC laser.

Some of the PhC QCL can emit very high peak power in the range of tens of milliwatts, which is large enough to allow a far field characterization. The far-field pattern of the laser devices is a key element necessary for the understanding of the lasing mechanism and light extraction, it is also an important feature that characterizes the device performance. A pyroelectric detector mounted on a double rotational stage that allows an angular scan close to 120° on θ and ϕ axes correspond to an angular scan in the planes of ΓK and ΓM , respectively^{125, 159}. The point $(\pm 90, 0)$ therefore indicates a longitudinal edge emission and point $(0, 0)$ an emission normal to the surface (Fig. 6.19).

Characterization results and discussions

Fabricated devices are characterized under pulsed condition (pulse = 200 ns, duty cycle = 1%). Measured pulsed light-current-voltage (L-I-V) curves at different temperature of one laser (the diameter of the top contact pad is 600 μm , ff is 30%, lattice constant is 21 μm) are plotted in Fig. 6.20. This device operates from 10 K up to 115 K with the maximum output power of 2.5 mW at 10 K. The L-I-V curve at 10 K shows a slope efficiency of 22 mW/A. Fig. 6.20a plots pulsed spectrum with photonic dispersion curve. The perfect agreement between the measurement result and the design can be observed. The device maintains single mode operation under 475 mA, 589 mA and 700 mA electrical pumping currents (Fig. 6.20c). The pulsed operation of this laser shows a J_{th} of 390 Acm^{-2} at 10 K. By comparing lasing frequency of different lattice constant in Fig. 6.20d, stable operating mode control of these devices has been demonstrated under pulsed conditions. The 40% filling factor operates up to 129 K (the diameter of the top contact pad is 600 μm , lattice constant is 23 μm). This is very close to the maximum operation temperature (130 K) of FP type device fabricated on the same QC layer.

Measured CW light-current-voltage (L-I-V) curves at different temperature of lasers are plotted in Fig. 6.21a (the diameter of the top contact pad is 600 μm , ff is 20%, the lattice constant is 19 μm) and b (the diameter of the top contact pad is 600 μm , ff is 30%, the lattice constant is 21 μm). The 20% (30%) filling factor device operates from 10 K up to 90 K (10 K to 100 K) with the maximum output power of 6 mW (3 mW) at 10 K, respectively. For 20% filling factor device, the L-I-V curve at 10 K shows a slope efficiency of 99 mW/A, meanwhile, the device has 1.4 mW output powers at 77 K (liquid nitrogen temperature). For 30% filling factor device, the L-I-V curve at 10 K shows a slope efficiency of 30 mW/A, meanwhile, the device has 1.2 mW output powers at 80 K. In Fig. 6.21 c and d, CW spectrum of 20% (30%) filling factor device measured at 10 K (72 K) shows a single mode operation at 3.2 THz with a at least 25 dB side mode suppression ratio. The 30% device maintains monochromatic operation until 80K. These features are the best reported CW operation in this frequency range. Compact and portable surface emission THz light source with mW level output power can be achieved under the help of a Stirling cryocooler (can cool device

down to 50 K at 5 W or 40 K at 1.5 W power dissipation). The pulsed operation of the 30% laser shows a T_{\max} of 115 K (Fig. 6.20c). Such highly comparable performance between the pulsed and CW operation proves the high pumping efficiency and effective heat flow transfer scheme of our design.

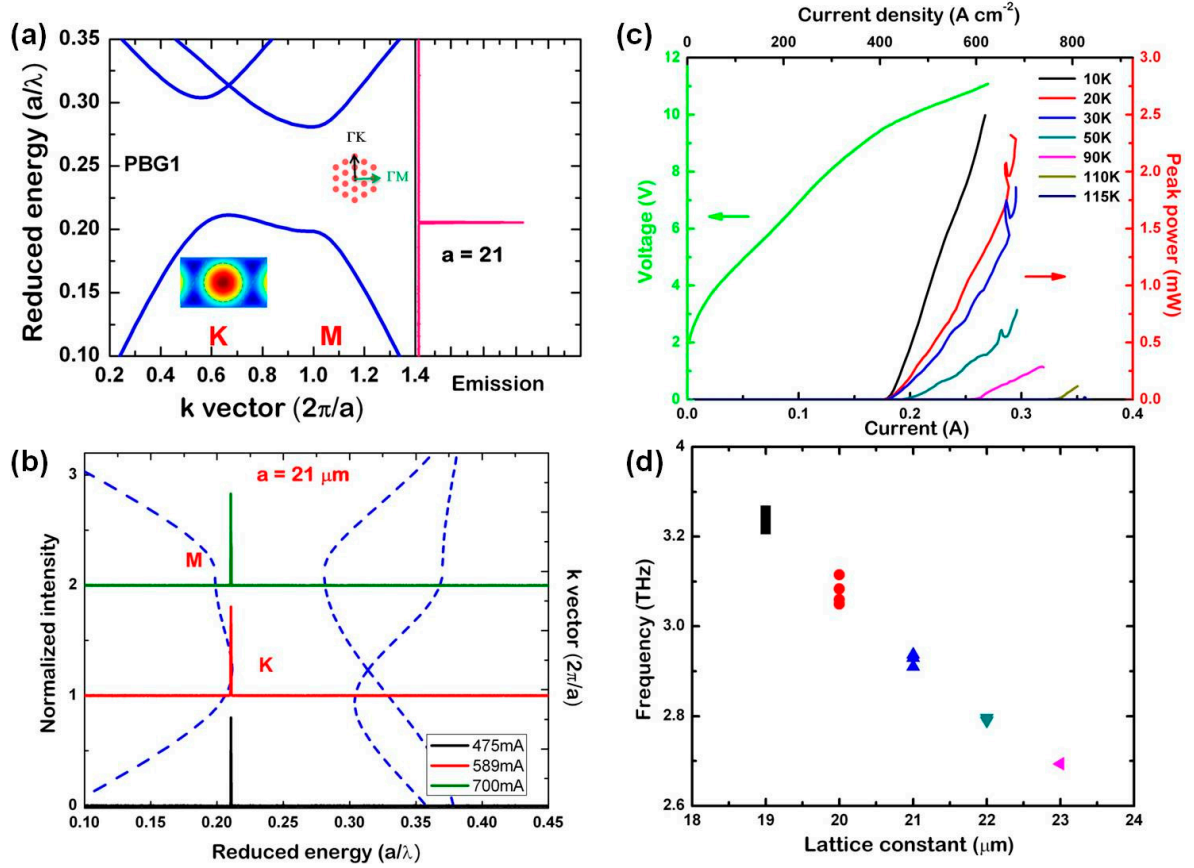


Figure 6.20 Operations under pulsed condition (pulse = 200 ns, duty cycle = 1%). a: Lasing spectrum at 10 K in the pulsed mode compared with PhC dispersion curve. b: Lasing spectrum measured with pumping current 475 mA (in black), 589 mA (in red) and 700 mA (in green) c: Light-current-voltage (LIV) of the device ($a = 21 \mu\text{m}$, fill factor 30%, top contact pad diameter $850 \mu\text{m}$) measured from 10 K to 115K. d: Lasing frequencies of different lattice constants (from 19 to 23 μm).

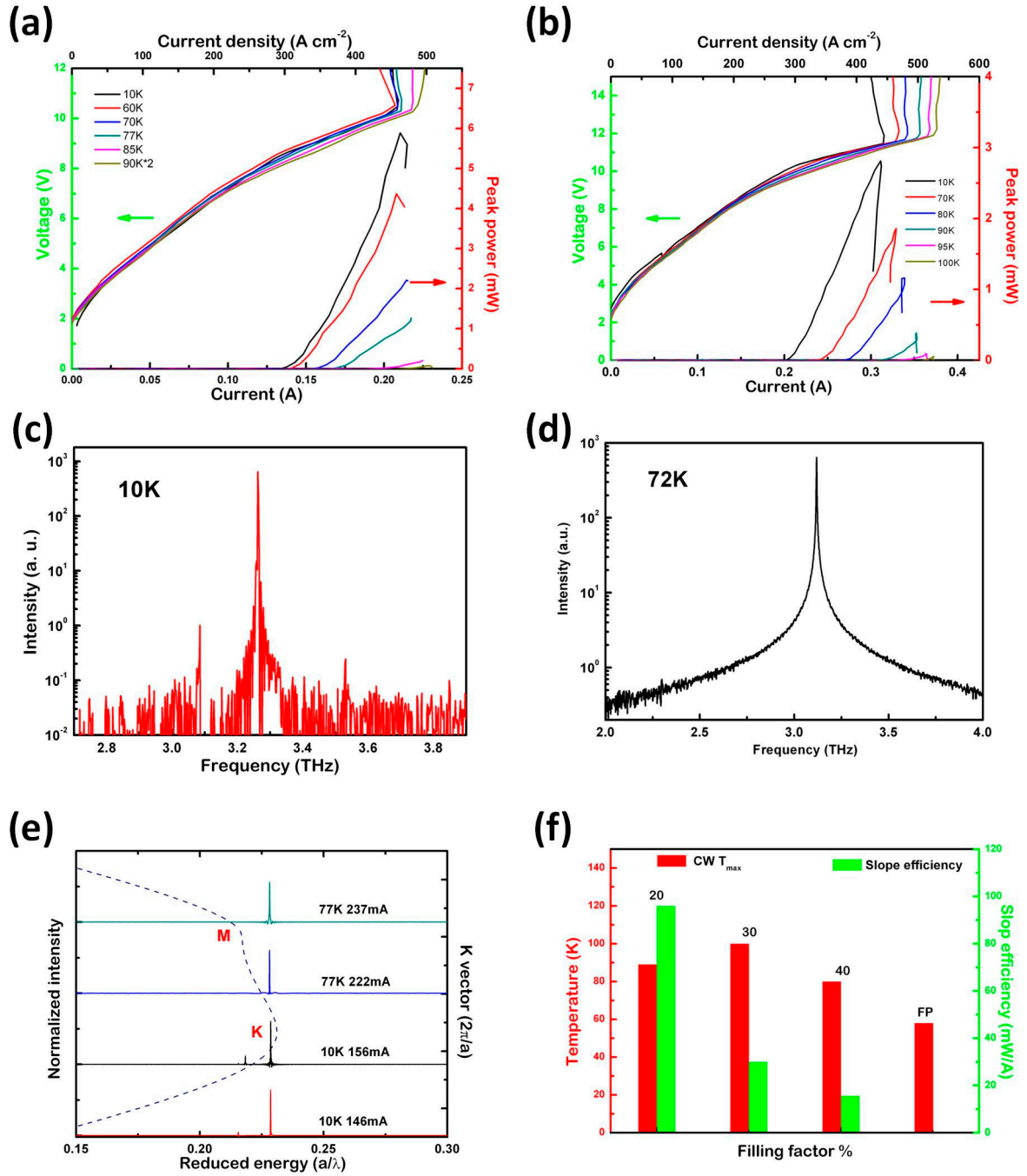


Figure 6.21 CW light-current-voltage and T_{max} characterizations. *a, b* : CW light-current-voltage of the devices (the diameter of the top contact pad is $600\mu\text{m}$, ff is 20% and 30%) for different heat sink temperatures (10 K to 90 K and 10K to 100K). *c, d* : The lasing spectrum of the device measured in *a* and *b* at heat sink temperature 10 K and 72 K. *e* : Lasing spectra of the device measured in *a* at different pumping current (146 mA and 156 mA at 10 K, 222 mA and 237 mA at 77 K) and heat sink temperatures compare with photonic band structure. *f* : Experimental maximum CW operation temperature (in red bar) and slop efficiency (in green bar) of different filling factor (20%, 30% and 40%) and FP laser (all have the same size and use the same QC layer).

The output power and T_{\max} also show dependence on the size of the device shows. As expected, the maximum output power is proportional to the dimension of the device. A larger device (the diameter of the top contact pad is $1000\mu\text{m}$, ff is 30%) has higher output power (9 mW at 10 K) and lower T_{\max} (89 K). We consider this as the result of the less efficient heat flow in larger device than that of a small one. The advantage of this design in term of overcoming the CW operation limits is shown in Fig. 6.21e. The experimental result of the same size (the diameter of the top contact pad is $600\mu\text{m}$) devices with different filling factor (20%, 30% and 40%) are compared with that of the in-plane emission FP device. All of them are processed with the same QC layer. By decreasing the filling factor from 40% to 20%, the slop efficiency is increasing as a result of the higher electrically pumping efficiency. T_{\max} is increasing as a result of the better heat flow and improved surface to volume ratio in the device. T_{\max} of 30% device (100 K) is 10 K higher than that of FP laser (90 K). The total loss increase induced by decrease of overlapping between the photonic band edge mode and QC pillar can explain that the T_{\max} drops from 30% device's 100 K to 20% device's 89 K. This indicates the existence of the optimal value of filling factor for CW operation as predicted in Fig. 6.14, which in our case is around 30%.

A well-controlled far-field beam pattern is another critical feature of an efficient laser device. Fig. 6.22b and 6.22c (the same device measured in Fig. 6.21a) show the measured vertically emitted far field patterns of two devices (the diameter of the central pumping pad is $600\mu\text{m}$, FF is 30%) without and with the optimized Bragg extractor respectively. The device without Bragg extractor has a highly divergent beam pattern as shown in previous simulations (Fig. 6.17). The far field patterns of the device with the optimized Bragg extractor show a highly collimated beam pattern with a single central lobe range of 10 degrees in both directions.

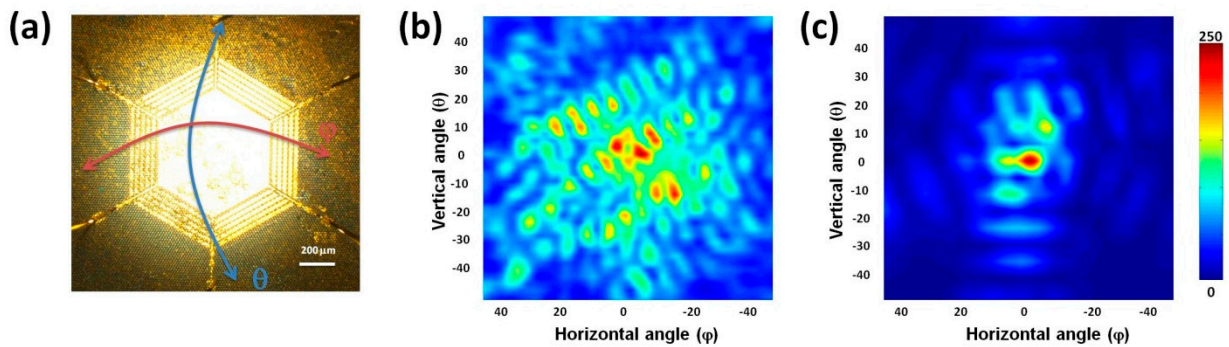


Figure 6.22 Far field characterizations. a, Device is scanned both in vertical (θ) and horizontal (ϕ) directions for far field measurements. b, Far field pattern of a device ($600\mu\text{m}$ diameter, ff is 30%, a is $21\mu\text{m}$) without Bragg extractor. c, Far field pattern of a device ($600\mu\text{m}$ diameter, ff is 30%, a is $21\mu\text{m}$) with Bragg extractor.

In this design, by utilizing a Bragg extractor to realize vertical emission and by introducing a PhC structure to achieve large pumping efficiency with better heat flow

dissipation, this work brings the CW operation of THz semiconductor lasers to a new level. Single mode surface emission with several milliwatts output power is observed at 3.12 THz. Thanks to the scalability of PhCs, this design can be applied throughout the entire THz wavelength range, especially for longer wavelengths. Further fine optimization can still be performed depending on the final applications or the required figures of merit. Larger devices can contribute for higher output power. A further optimized extractor design can help for a collimated far field pattern and larger extraction efficiency. A variety of real applications of the CW operation THz light sources can be achieved in the future with optimized slope efficiencies and remarkable output powers above the liquid nitrogen temperature.

Conclusions and perspectives

The goal of my thesis is investigate the optical properties of two dimensional PhCs. Defect modes introduced within the photonic band gap and light wave propagating close to the band edge or with slow group velocity are two important aspects of my PhD work. On one hand, I tried to apply slow light concepts to develop PhC THz light sources for applications, especially for CW operation. On the other hand, I concentrated to apply hollow PhC cavities on optical trapping and refractive sensing applications.

Different approaches are experimentally investigated to improve the coupling efficiency into PhC devices, especially for the slow light enhancement applications. At the facet of the device, anti-reflection coating layer (Si_3N_4 or TiO_2) and SU-8 coupler are discussed. A thin layer of TiO_2 coated by e-beam evaporation on facets can successfully decrease the reflectivity down to 3%. Furthermore, SU-8 coupler can achieve both lower than 1% reflectivity and higher than 5 times transmission power. PhC tapers with gradually changed air hole diameters are used to overcome the mismatch in group velocity between the fast light in the strip waveguide and the slow light in the guided mode of PhC waveguide. These SU-8 couplers and PhC group index tapers is useful in applications of PhC structure in refractive index sensing and optical trapping.

In chapter 5, we have demonstrated the first experimental resonant optical trap in a 2D PhC cavity (700 nm diameter) that allows for simultaneous isolation, manipulation and analysis of dielectric particles (500 nm) similar in size with viruses and small bacteria with sub-100 μW trapping power. The cavity resonance shifts depends on the particle size, refractive index and shape (due to different overlap with the cavity mode, not demonstrated yet). This capability can be used to separate particles of different sizes or to separate particles of identical sizes but different refractive indices and might be even capable of separate identical particles with different form factors. The suspended feature of the trap allows the specimen to be unaffected by surface chemistry influences. The long trapping times along with very small residual Brownian motion should be of significant interest for studies that use spatially resolved spectroscopy.

In chapter 6, a robust surface emitting continuous-wave terahertz QC laser is realized in a two-dimensional PhC structure by a second order Bragg grating extractor that simultaneously provides the boundary condition necessary for mode selection. This results in a 3.12 THz single mode CW operation with a 3 mW output power and a maximum operation temperature (T_{max}) of 100 K. Also, a highly collimated far-field pattern is

demonstrated, which paves the way towards real world applications. Our work brings the CW operation of THz semiconductor laser to a new level.

A significant advantage of using hollow PhC devices to trap particles lies in the inherent scalability of the PhC properties. The sizes and wavelengths can be scaled down to other platforms like Gallium Nitride ¹⁰⁷ in the visible wavelength region where the smaller size of the cavity could facilitate the trapping of particles of the order of 50 to 100 nm. The design for better coupling efficiency will be useful when the target is sub-100 nm particle or other highly power sensitive bio-objects. The addressability of multiple traps and the compatibility to standard CMOS process brings immediate access to various exciting on-chip biological analysis applications for the near future.

A further optimized extractor design can help for a collimated far field pattern and larger extraction efficiency. Thanks to the scalability of PhCs, this design can be applied in the rest of the THz wavelength range, especially for longer wavelength. A variety of real applications of the CW operation THz light sources can be achieved in the future with optimized slope efficiencies and remarkable output powers beyond liquid nitrogen temperature.

Bibliography

1. J. D. Joannopoulos, R. D. Meade and J. N. Winn, *Photonic Crystals: Molding the Flow of Light*. (Princeton: Princeton University Press, 1995).
2. europactice-ic. http://www.europactice-ic.com/SiPhotonics_technology_passives.php.
3. P. J. Bock, P. Cheben, J. H. Schmid, J. Lapointe, A. Delage, D. X. Xu, S. Janz, A. Densmore and T. J. Hall, *Optics Express* **18** (15), 16146-16155 (2010).
4. P. Dumon, G. Priem, L. R. Nunes, W. Bogaerts, D. Van Thourhout, P. Bienstman, T. K. Liang, M. Tsuchiya, P. Jaenen, S. Beckx, J. Wouters and R. Baets, *Jpn J Appl Phys* **45** (8B), 6589-6602 (2006).
5. N. V. Triviño, G. Rossbach, U. Dharanipathy, J. Levrat, A. Castiglia, J. F. Carlin, K. A. Atlasov, R. Butte, R. Houdré and N. Grandjean, *Appl Phys Lett* **100** (7) (2012).
6. U. Dharanipathy, N. V. Triviño, C. Yan, Z. Diao, J. F. Carlin, N. Grandjean and R. Houdré, *Opt Lett* **37** (22), 4588-4590 (2012).
7. Opal33. <http://www.opal33.com/black-opal.html>.
8. S. i. c. o. M. Chi. SEM Image of the opal. Compare near-gem quality opal and gem-quality fire opal (100,000 x magnification) from (dry) Lake Tecopa, Inyo County, California, USA.
9. wikipedia. http://en.wikipedia.org/wiki/File:Blue_morpho_butterfly.jpg.
10. L. Bingham, I. Bingham, S. Geary, J. Tanner, C. Driscoll, B. Cluff and J. S. Gardner, *Microsc Res Techniq* **31** (1), 93-94 (1995).
11. S. John, *Phys Rev Lett* **58** (23), 2486-2489 (1987).
12. E. Yablonovitch, *Phys Rev Lett* **58** (20), 2059-2062 (1987).
13. K. M. Ho, C. T. Chan and C. M. Soukoulis, *Phys Rev Lett* **65** (25), 3152-3155 (1990).
14. E. Yablonovitch, T. J. Gmitter and K. M. Leung, *Phys Rev Lett* **67** (17), 2295-2298 (1991).
15. U. Gruning, V. Lehmann and C. M. Engelhardt, *Appl Phys Lett* **66** (24), 3254-3256 (1995).

16. X. D. Fan, I. M. White, S. I. Shopova, H. Y. Zhu, J. D. Suter and Y. Z. Sun, *Anal Chim Acta* **620** (1-2), 8-26 (2008).
17. M. Loncar, A. Scherer and Y. M. Qiu, *Appl Phys Lett* **82** (26), 4648-4650 (2003).
18. J. Jágerská, H. Zhang, Z. L. Diao, N. Le Thomas and R. Houdré, *Opt Lett* **35** (15), 2523-2525 (2010).
19. L. O'Faolain, X. Yuan, D. McIntyre, S. Thoms, H. Chong, R. M. De la Rue and T. F. Krauss, *Electron Lett* **42** (25), 1454-1455 (2006).
20. J. T. Li, L. O'Faolain, S. A. Schulz and T. F. Krauss, *Photonics Nanostruct.* **10** (4), 589-593 (2012).
21. H. Benisty, S. Olivier, C. Weisbuch, M. Agio, M. Kafesaki, C. M. Soukoulis, M. Qiu, M. Swillo, A. Karlsson, B. Jaskorzynska, A. Talneau, J. Moosburger, M. Kamp, A. Forchel, R. Ferrini, R. Houdré and U. Oesterle, *Ieee J Quantum Elect* **38** (7), 770-785 (2002).
22. S. H. Tao, M. B. Yu, J. F. Song, Q. Fang, R. Yang, G. Q. Lo and D. L. Kwong, *Appl Phys Lett* **92** (3) (2008).
23. T. Baba, *Nat Photonics* **2** (8), 465-473 (2008).
24. V. R. Almeida, Q. F. Xu, C. A. Barrios and M. Lipson, *Opt Lett* **29** (11), 1209-1211 (2004).
25. Q. F. Xu, V. R. Almeida, R. R. Panepucci and M. Lipson, *Opt Lett* **29** (14), 1626-1628 (2004).
26. C. C. Cheng, V. ArbetEngels, A. Scherer and E. Yablonovitch, *Phys Scripta* **T68**, 17-20 (1996).
27. V. Mizeikisa, S. Juodkazisa, A. Marcinkevičiusa, S. Matsuob and H. Misawab, *Journal of Photochemistry and Photobiology C: Photochemistry Reviews* **2** (1), 35-69 (2001).
28. S. Y. Lin, J. G. Fleming, D. L. Hetherington, B. K. Smith, R. Biswas, K. M. Ho, M. M. Sigalas, W. Zubrzycki, S. R. Kurtz and J. Bur, *Nature* **394** (6690), 251-253 (1998).
29. J. K. Gansel, M. Thiel, M. S. Rill, M. Decker, K. Bade, V. Saile, G. von Freymann, S. Linden and M. Wegener, *Science* **325** (5947), 1513-1515 (2009).
30. D. Leuenberger, PhD thesis, Ecole Polytechnique Federale de Lausanne (EPFL), 2004.
31. V. Zabelin, PhD thesis, Ecole Polytechnique Federale de Lausanne (EPFL), 2009.

32. CMi. http://cmi.epfl.ch/photo/Laser_DWL200/DWL200_introduction.php.
33. M. Ahn, R. K. Heilmann and M. L. Schattenburg, *J Vac Sci Technol B* **25** (6), 2593-2597 (2007).
34. S. Deladi, S. V, G. J. M. Krijnen and M. C. Elwenspoek, *J Micromech Microeng* **14** (12), 1659-1664 (2004).
35. CMi. http://cmi.epfl.ch/ebeam/VistecEBPG5000_introduction.php.
36. M. Hill, M. Cryan, N. Lim, R. Varrazza, P. Heard, S. Yu and J. Rorison, *Icton 2004: 6th International Conference on Transparent Optical Networks, Proceedings, Vol 2*, 135-138 (2004).
37. J. Tian, W. Yan, Y. Z. Liu, J. Luo, D. Z. Zhang, Z. Y. Li and M. Qiu, *J Lightwave Technol* **27** (19), 4306-4310 (2009).
38. J. Schrauwen, F. Van Laere, D. Van Thourhout and R. Baets, *Ieee Photonic Tech L* **19** (9-12), 816-818 (2007).
39. CMi. <http://cmi.epfl.ch/etch/AMS200.php>.
40. J. Jágorská, N. Le Thomas, R. Houdré, J. Bolten, C. Moormann, T. Wahlbrink, J. Crtyroky, M. Waldow and M. Forst, *Opt Lett* **32** (18), 2723-2725 (2007).
41. J. Canning, N. Skivesen, M. Kristensen, L. H. Frandsen, A. Lavrinenko, C. Martelli and A. Tetu, *Optics Express* **15** (23), 15603-15614 (2007).
42. E. Roduner, *Nanoscopic materials*. (RSC publishing, 2006).
43. P. N. Prasad, *Nanophotonics*. (Wiley, 2004).
44. A. Benz, C. Deutsch, G. Fasching, K. Unterrainer, A. M. Andrews, P. Klang, W. Schrenk and G. Strasser, *Optics Express* **17** (2), 941-946 (2009).
45. CMi. <http://cmi.epfl.ch/threefive/plasmalab100PECVD.php>
46. CMi. <http://cmi.epfl.ch/thinfilms/Lab600H.php>.
47. M. Notomi, A. Shinya, S. Mitsugi, E. Kuramochi and H. Y. Ryu, *Optics Express* **12** (8), 1551-1561 (2004).
48. S. Scheerlinck, J. Schrauwen, F. Van Laere, D. Taillaert, D. Van Thourhout and R. Baets, *Optics Express* **15** (15), 9625-9630 (2007).

49. J. H. Schmid, P. Cheben, S. Janz, J. Lapointe, E. Post and D. X. Xu, *Opt Lett* **32** (13), 1794-1796 (2007).
50. W. Bogaerts, D. Taillaert, P. Dumon, D. Van Thourhout and R. Baets, *Optics Express* **15** (4), 1567-1578 (2007).
51. P. Cheben, P. J. Bock, J. H. Schmid, J. Lapointe, S. Janz, D. X. Xu, A. Densmore, A. Delage, B. Lamontagne and T. J. Hall, *Opt Lett* **35** (15), 2526-2528 (2010).
52. D. Taillaert, W. Bogaerts, P. Bienstman, T. F. Krauss, P. Van Daele, I. Moerman, S. Verstuyft, K. De Mesel and R. Baets, *Ieee J Quantum Elect* **38** (7), 949-955 (2002).
53. S. J. McNab, N. Moll and Y. A. Vlasov, *Optics Express* **11** (22), 2927-2939 (2003).
54. J. P. Hugonin, P. Lalanne, T. P. White and T. E. Krauss, *Opt Lett* **32** (18), 2638-2640 (2007).
55. C. Y. Lin, A. X. Wang, W. C. Lai, J. L. Covey, S. Chakravarty and R. T. Chen, *Opt Lett* **37** (2), 232-234 (2012).
56. C. Y. Lin, X. L. Wang, S. Chakravarty, B. S. Lee, W. C. Lai and R. T. Chen, *Appl Phys Lett* **97** (18) (2010).
57. Z. C. Wang, N. Zhu, Y. B. Tang, L. Wosinski, D. X. Dai and S. L. He, *Opt Lett* **34** (10), 1498-1500 (2009).
58. A. Hosseini, X. C. Xu, D. N. Kwong, H. Subbaraman, W. Jiang and R. T. Chen, *Appl Phys Lett* **98** (3) (2011).
59. S. Rahimi, A. Hosseini, X. C. Xu, H. Subbaraman and R. T. Chen, *Optics Express* **19** (22), 21832-21841 (2011).
60. N. Ozaki, Y. Kitagawa, Y. Takata, N. Ikeda, Y. Watanabe, A. Mizutani, Y. Sugimoto and K. Asakawa, *Optics Express* **15** (13), 7974-7983 (2007).
61. K. Ustun and H. Kurt, *J Appl Phys* **110** (11) (2011).
62. K. Mnaymneh, S. Frederick, D. Dalacu, J. Lapointe, P. J. Poole and R. L. Williams, *Opt Lett* **37** (2), 280-282 (2012).
63. J. Jágerská, H. Zhang, N. Le Thomas and R. Houdré, *Appl Phys Lett* **95** (11) (2009).
64. N. Le Thomas, R. Houdré, M. V. Kotlyar, D. O'Brien and T. E. Krauss, *J Opt Soc Am B* **24** (12), 2964-2971 (2007).

65. R. De la Rue, H. Chong, M. Gnan, N. Johnson, I. Ntakis, P. Pottier, M. Sorel, A. M. Zain, H. Zhang, E. Camargo, C. J. Jin, M. Armenise and C. Ciminelli, *New J Phys* **8** (2006).
66. S. Zlatanovic, L. W. Mirkarimi, M. M. Sigalas, M. A. Bynum, E. Chow, K. M. Robotti, G. W. Burr, S. Esener and A. Grot, *Sensor Actuat B-Chem* **141** (1), 13-19 (2009).
67. D. Dorfner, T. Zabel, T. Hurlimann, N. Hauke, L. Frandsen, U. Rant, G. Abstreiter and J. Finley, *Biosens Bioelectron* **24** (12), 3688-3692 (2009).
68. L. Rindorf, J. B. Jensen, M. Dufva, L. H. Pedersen, P. E. Hoiby and O. Bang, *Optics Express* **14** (18), 8224-8231 (2006).
69. M. R. Lee and P. M. Fauchet, *Opt Lett* **32** (22), 3284-3286 (2007).
70. N. Skivesen, A. Tetu, M. Kristensen, J. Kjems, L. H. Frandsen and P. I. Borel, *Optics Express* **15** (6), 3169-3176 (2007).
71. S. Mandal and D. Erickson, *Optics Express* **16** (3), 1623-1631 (2008).
72. E. Chow, A. Grot, L. W. Mirkarimi, M. Sigalas and G. Girolami, *Opt Lett* **29** (10), 1093-1095 (2004).
73. M. Lee and P. M. Fauchet, *Optics Express* **15** (8), 4530-4535 (2007).
74. J. Jágorská, PhD thesis, Ecole Polytechnique Federale de Lausanne (EPFL), 2011.
75. J. T. Robinson, C. Manolatu, L. Chen and M. Lipson, *Phys Rev Lett* **95** (14) (2005).
76. A. Di Falco, L. O'Faolain and T. F. Krauss, *Applied Physics Letters* **94** (6) (2009).
77. T. Yamamoto, M. Notomi, H. Taniyama, E. Kuramochi, Y. Yoshikawa, Y. Torii and T. Kuga, *Optics Express* **16** (18), 13809-13817 (2008).
78. J. Gao, J. F. McMillan, M. C. Wu, J. J. Zheng, S. Assefa and C. W. Wong, *Appl Phys Lett* **96** (5) (2010).
79. N. A. Mortensen, S. S. Xiao and J. Pedersen, *Microfluid Nanofluid* **4** (1-2), 117-127 (2008).
80. T. Asano, B. S. Song, Y. Akahane and S. Noda, *Ieee J Sel Top Quant* **12** (6), 1123-1134 (2006).
81. A. Ashkin, J. M. Dziedzic, J. E. Bjorkholm and S. Chu, *Opt. Lett.* **11** (5), 288-290 (1986).
82. A. Ashkin and J. Dziedzic, *Science* **235** (4795), 1517-1520 (1987).

83. T. Aoki, B. Dayan, E. Wilcut, W. P. Bowen, A. S. Parkins, T. J. Kippenberg, K. J. Vahala and H. J. Kimble, *Nature* **443** (7112), 671-674 (2006).
84. J. McKeever, J. R. Buck, A. D. Boozer, A. Kuzmich, H. C. Nägerl, D. M. Stamper-Kurn and H. J. Kimble, *Physical Review Letters* **90** (13), 133602 (2003).
85. T. J. Kippenberg and K. J. Vahala, *Science* **321** (5893), 1172-1176 (2008).
86. A. Naik, O. Buu, M. D. LaHaye, A. D. Armour, A. A. Clerk, M. P. Blencowe and K. C. Schwab, *Nature* **443** (7108), 193-196 (2006).
87. P. F. Barker and M. N. Shneider, *Physical Review A* **81** (2), 023826 (2010).
88. J. Hu, S. Lin, L. C. Kimerling and K. Crozier, *Physical Review A* **82** (5), 053819 (2010).
89. D. E. Chang, C. A. Regal, S. B. Papp, D. J. Wilson, J. Ye, O. Painter, H. J. Kimble and P. Zoller, *Proceedings of the National Academy of Sciences* **107** (3), 1005-1010 (2010).
90. O. Romero-Isart, A. C. Pflanzner, M. L. Juan, R. Quidant, N. Kiesel, M. Aspelmeyer and J. I. Cirac, *Physical Review A* **83** (1), 013803 (2011).
91. M. Barth and O. Benson, *Applied Physics Letters* **89** (25) (2006).
92. A. Rahmani and P. C. Chaumet, *Opt. Express* **14** (13), 6353-6358 (2006).
93. M. R. Lee and P. M. Fauchet, *Opt. Lett.* **32** (22), 3284-3286 (2007).
94. J. Jágerská, H. Zhang, Z. Diao, N. Le Thomas and R. Houdré, *Opt. Lett.* **35** (15), 2523-2525 (2010).
95. M. L. Juan, R. Gordon, Y. Pang, F. Eftekhari and R. Quidant, *Nat Phys* **5** (12), 915-919 (2009).
96. K. C. Neuman and S. M. Block, *Rev Sci Instrum* **75** (9), 2787-2809 (2004).
97. A. Ashkin, *P Natl Acad Sci USA* **94** (10), 4853-4860 (1997).
98. W. H. Wright, G. J. Sonek and M. W. Berns, *Appl Phys Lett* **63** (6), 715-717 (1993).
99. Y. Harada and T. Asakura, *Opt Commun* **124** (5-6), 529-541 (1996).
100. A. H. J. Yang, S. D. Moore, B. S. Schmidt, M. Klug, M. Lipson and D. Erickson, *Nature* **457** (7225), 71-75 (2009).
101. S. Mandal, X. Serey and D. Erickson, *Nano Lett* **10** (1), 99-104 (2010).

102. M. A. Unger, H.-P. Chou, T. Thorsen, A. Scherer and S. R. Quake, *Science* **288** (5463), 113-116 (2000).
103. D. Psaltis, S. R. Quake and C. Yang, *Nature* **442** (7101), 381-386 (2006).
104. C. Monat, P. Domachuk and B. J. Eggleton, *Nat Photon* **1** (2), 106-114 (2007).
105. S. Mandal, X. Serey and D. Erickson, *Nano Letters* **10** (1), 99-104 (2009).
106. S. Lin, E. Schonbrun and K. Crozier, *Nano Letters* **10** (7), 2408-2411 (2010).
107. N. V. Triviño, G. Rossbach, U. Dharanipathy, J. Levrat, A. Castiglia, J. F. Carlin, K. A. Atlasov, R. Butte, R. Houdré and N. Grandjean, *Applied Physics Letters* **100** (7), 071103-071103 (2012).
108. K. C. Neuman and A. Nagy, *Nat Meth* **5** (6), 491-505 (2008).
109. J. Faist, F. Capasso, D. L. Sivco, C. Sirtori, A. L. Hutchinson and A. Y. Cho, *Science* **264** (5158), 553-556 (1994).
110. R. Kohler, A. Tredicucci, F. Beltram, H. E. Beere, E. H. Linfield, A. G. Davies, D. A. Ritchie, R. C. Iotti and F. Rossi, *Nature* **417** (6885), 156-159 (2002).
111. B. S. Williams, *Nat Photonics* **1** (9), 517-525 (2007).
112. G. Scalari, C. Walther, M. Fischer, R. Terazzi, H. Beere, D. Ritchie and J. Faist, *Laser Photonics Rev* **3** (1-2), 45-66 (2009).
113. H. Zhang, L. A. Dunbar, G. Scalari, R. Houdré and J. Faist, *Optics Express* **15** (25), 16818-16827 (2007).
114. Y. Chassagneux, R. Colombelli, W. Maineult, S. Barbieri, H. E. Beere, D. A. Ritchie, S. P. Khanna, E. H. Linfield and A. G. Davies, *Nature* **457** (7226), 174-178 (2009).
115. R. Colombelli, K. Srinivasan, M. Troccoli, O. Painter, C. F. Gmachl, D. M. Tennant, A. M. Sergent, D. L. Sivco, A. Y. Cho and F. Capasso, *Science* **302** (5649), 1374-1377 (2003).
116. S. Riechel, C. Kallinger, U. Lemmer, J. Feldmann, A. Gombert, V. Wittwer and U. Scherf, *Appl Phys Lett* **77** (15), 2310-2312 (2000).
117. M. Scharrer, A. Yamilov, X. H. Wu, H. Cao and R. P. H. Chang, *Appl Phys Lett* **88** (20) (2006).

118. M. Imada, S. Noda, A. Chutinan, T. Tokuda, M. Murata and G. Sasaki, *Appl Phys Lett* **75** (3), 316-318 (1999).
119. A. Chen, S. J. Chua, G. C. Xing, W. Ji, X. H. Zhang, J. R. Dong, L. K. Jian and E. A. Fitzgerald, *Appl Phys Lett* **90** (1) (2007).
120. O. Painter, J. Vuckovic and A. Scherer, *J Opt Soc Am B* **16** (2), 275-285 (1999).
121. J. P. Dowling, M. Scalora, M. J. Bloemer and C. M. Bowden, *J Appl Phys* **75** (4), 1896-1899 (1994).
122. M. Meier, A. Mekis, A. Dodabalapur, A. Timko, R. E. Slusher, J. D. Joannopoulos and O. Nalamasu, *Appl Phys Lett* **74** (1), 7-9 (1999).
123. H. Y. Ryu, S. H. Kwon, Y. J. Lee, Y. H. Lee and J. S. Kim, *Appl Phys Lett* **80** (19), 3476-3478 (2002).
124. B. S. Williams, S. Kumar, H. Callebaut, Q. Hu and J. L. Reno, *Appl Phys Lett* **83** (11), 2124-2126 (2003).
125. L. Sirigu, R. Terazzi, M. I. Amanti, M. Giovannini, J. Faist, L. A. Dunbar and R. Houdré, *Optics Express* **16** (8), 5206-5217 (2008).
126. O. P. Marshall, V. Apostolopoulos, J. R. Freeman, R. Rungsawang, H. E. Beere and D. A. Ritchie, *Appl Phys Lett* **93** (17) (2008).
127. B. Ferguson and X. C. Zhang, *Nat Mater* **1** (1), 26-33 (2002).
128. W. S. Holland, J. S. Greaves, B. Zuckerman, R. A. Webb, C. McCarthy, I. M. Coulson, D. M. Walther, W. R. F. Dent, W. K. Gear and I. Robson, *Nature* **392** (6678), 788-791 (1998).
129. P. Y. Han, M. Tani, M. Usami, S. Kono, R. Kersting and X. C. Zhang, *J Appl Phys* **89** (4), 2357-2359 (2001).
130. D. H. Auston, K. P. Cheung, J. A. Valdmanis and D. A. Kleinman, *Phys Rev Lett* **53** (16), 1555-1558 (1984).
131. P. F. Taday, I. V. Bradley, D. D. Arnone and M. Pepper, *J Pharm Sci* **92** (4), 831-838 (2003).
132. B. B. Hu and M. C. Nuss, *Opt Lett* **20** (16), 1716-& (1995).
133. E. Pickwell and V. P. Wallace, *J Phys D Appl Phys* **39** (17), R301-R310 (2006).

134. A. Y. Cho, J Cryst Growth **111** (1-4), 1-13 (1991).
135. C. A. Felippa, Int J Numer Meth Eng **37** (13), 2159-& (1994).
136. G. Scalari, PhD Thesis, Université de Neuchâtel, 2005.
137. A. W. M. Lee, Q. Qin, S. Kumar, B. S. Williams and Q. Hu, Appl Phys Lett **89** (14) (2006).
138. G. Scalari, C. Walther, J. Faist, H. Beere and D. Ritchie, Appl Phys Lett **88** (14) (2006).
139. B. S. Williams, S. Kumar, Q. Hu and J. L. Reno, Optics Express **13** (9), 3331-3339 (2005).
140. B. S. Williams, S. Kumar, Q. Hu and J. L. Reno, Electron Lett **42** (2), 89-91 (2006).
141. A. Tredicucci, F. Capasso, C. Gmachl, D. L. Sivco, A. L. Hutchinson and A. Y. Cho, Appl Phys Lett **73** (15), 2101-2103 (1998).
142. J. Faist, M. Beck, T. Aellen and E. Gini, Appl Phys Lett **78** (2), 147-149 (2001).
143. G. Scamarcio, F. Capasso, C. Sirtori, J. Faist, A. L. Hutchinson, D. L. Sivco and A. Y. Cho, Science **276** (5313), 773-776 (1997).
144. L. Esaki and R. Tsu, Ibm J Res Dev **14** (1), 61-& (1970).
145. J. Faist, F. Capasso, C. Sirtori, D. L. Sivco, A. L. Hutchinson, S. N. G. Chu and A. Y. Cho, Appl Phys Lett **65** (1), 94-96 (1994).
146. G. Scalari, L. Ajili, J. Faist, H. Beere, E. Linfield, D. Ritchie and G. Davies, Appl Phys Lett **82** (19), 3165-3167 (2003).
147. J. A. Fan, M. A. Belkin, F. Capasso, S. Khanna, M. Lachab, A. G. Davies and E. H. Linfield, Optics Express **14** (24), 11672-11680 (2006).
148. M. Zhu, S. L. Xiao, Z. Zhou, W. Guo, L. L. Yi, M. H. Bi, W. S. Hu and B. Geller, Optics Express **19** (9), 8000-8010 (2011).
149. J. E. Carroll, J. Whiteaway and D. Plumb, *Distributed feedback semiconductor lasers*. (The Institution of Electrical Engineers : SPIE Optical Engineering Press, London, UK, 1998).
150. H. Kogelnik and C. V. Shank, J Appl Phys **43** (5), 2327-& (1972).
151. S. Wang, Ieee J Quantum Elect **Qe10** (4), 413-427 (1974).

152. F. K. Kneubuhl, *Theories on distributed feedback lasers*. (Harwood academic publishers, 1993).
153. B. S. K. L. H. Ghafouri - Shiraz, *Distributed feedback laser diodes*. (Wiley, 1996).
154. J. Faist, C. Gmachl, F. Capasso, C. Sirtori, D. L. Sivco, J. N. Baillargeon and A. Y. Cho, *Appl Phys Lett* **70** (20), 2670-2672 (1997).
155. I. Vurgaftman and J. R. Meyer, *Appl Phys Lett* **78** (11), 1475-1477 (2001).
156. I. Vurgaftman and J. R. Meyer, *Ieee J Quantum Elect* **38** (6), 592-602 (2002).
157. W. W. Bewley, C. L. Felix, I. Vurgaftman, R. E. Bartolo, J. R. Lindle, J. R. Meyer, H. Lee and R. U. Martinelli, *Appl Phys Lett* **79** (20), 3221-3223 (2001).
158. H. Zhang, G. Scalari, M. Beck, J. Faist and R. Houdré, *Optics Express* **19** (11), 10707-10713 (2011).
159. M. I. Amanti, M. Fischer, G. Scalari, M. Beck and J. Faist, *Nat Photonics* **3** (10), 586-590 (2009).
160. G. Y. Xu, R. Colombelli, S. P. Khanna, A. Belarouci, X. Letartre, L. H. Li, E. H. Linfield, A. G. Davies, H. E. Beere and D. A. Ritchie, *Nature Communications* **3** (2012).
161. M. S. Vitiello, G. Scamarcio, V. Spagnolo, S. S. Dhillon and C. Sirtori, *Appl Phys Lett* **90** (19) (2007).
162. G. Sevin, D. Fowler, G. Xu, F. H. Julien, R. Colombelli, H. Beere and D. Ritchie, *Electron Lett* **46** (22), 1513-U1559 (2010).
163. H. Zhang, G. Scalari, J. Faist, L. A. Dunbar and R. Houdré, *J Appl Phys* **108** (9) (2010).
164. S. Kumar, B. S. Williams, Q. Qin, A. W. M. Lee, Q. Hu and J. L. Reno, *Optics Express* **15** (1), 113-128 (2007).
165. M. B. Mitchell, *Adv Chem Ser* (236), 351-375 (1993).
166. B. Stuart, *Infrared spectroscopy : fundamentals and applications*. (John Wiley & Sons, Chichester, West Sussex, England, 2004).

Publications

Peer-reviewed publications

1. Z. Diao, C. Bonzon, G. Scalari, M. Beck, J. Faist, and R. Houdré, “Continuous-wave vertically emitting photonic crystal terahertz laser,” submitted, (2013).
2. N. Descharmes, U. P. Dharanipathy, Z. Diao, and R. Houdré “Observation of back-action and self-induced trapping in a planar hollow photonic crystal cavity”, *Phy. Rev. Lett.*, **110**, 123601 (2013).
3. N. Vico Triviño, U. Dharanipathy, J.-F. Carlin, Z. Diao, R. Houdré, and N. Grandjean , “Integrated photonics on silicon with wide bandgap GaN semiconductor”, *Appl. Phys. Lett.* **102**, 081120 (2013).
4. U. Dharanipathy, N. Vico Triviño, C. Yan, Z. Diao, J. Carlin, N. Grandjean, and R. Houdré, “Near-infrared characterization of gallium nitride photonic-crystal waveguides and cavities”, *Opt Lett.* **37**, 4588-90 (2012).
5. N. Le Thomas, Z. Diao, H. Zhang, and R. Houdré, "Statistical analysis of subnanometer residual disorder in photonic crystal waveguides: Correlation between slow light properties and structural properties", *Journal Vacuum Science & Technology B*, **29**, 051601 (2011).
6. J. Jágerská, H. Zhang, Z. Diao, N. Le Thomas and R. Houdré, “Refractive index sensing with an air-slot photonic crystal nanocavity”, *Opt. Lett.* **35**, 2523-2525 (2010).
7. N. Descharmes, U. P. Dharanipathy, Z. Diao, and R. Houdré “Self-trapping and back-action effects in hollow photonic crystal cavity optical trap”, *Proceedings of SPIE 2013*, in press, (2013).

Conference presentations and posters

1. Z. Diao, C. Bonzon, G. Scalari, J. Faist, and R. Houdré, “Surface emitting Terahertz Photonic Crystal QCLs realized by Bragg boundary condition,” oral presentation, *CLEO: Applications and Technology 2012*, San Jose, CA, USA (2012)
2. Z. Diao, C. Bonzon, G. Scalari, J. Faist, and R. Houdré, “Surface emitting Terahertz Photonic Crystal QCLs realized by Bragg boundary condition,” oral presentation, *10th International Symposium on Photonic and Electromagnetic Crystal Structures (PECS-X)*, Santa Fe, NM, USA (2012).

3. Z. Diao, Christopher Bonzon, Giacomo Scalari, Jérôme Faist, and R. Houdré, "Surface emitting Terahertz Photonic Crystal QCLs realized by Bragg boundary condition," oral presentation, EOS Topical Meeting on Lasers (ETML'11), Capri, Italy, (2011).
4. Z. Diao, Christopher Bonzon, Giacomo Scalari, Jérôme Faist, and R. Houdré, "Surface emitting Terahertz Photonic Crystal QCLs realized by Bragg boundary condition," oral presentation, European Semiconductor Laser Workshop (ESLW2011), Lausanne, Switzerland, (2011).
5. N. Descharmes, U. P. Dharanipathy, Z. Diao, and R. Houdré "Self-trapping and back-action effects in hollow photonic crystal cavity optical trap," oral presentation, SPIE 2013, San Francisco, CA, USA (2013)
6. N. Descharmes, U. P. Dharanipathy, Z. Diao, and R. Houdré "Microfluidic integrated hollow photonic crystal cavities for single particle and resonant field interaction," oral presentation, 10th International Symposium on Photonic and Electromagnetic Crystal Structures (PECS-X), Santa Fe, NM, USA (2012).
7. N. V. Triviño, G. Rossbach, U. Dharanipathy, J. Levrat, A. Castiglia, J. F. Carlin, K. A. Atlasov, R. Butte, R. Houdré, and N. Grandjean "High Quality Factor 2D GaN Photonic Crystal Cavity Membranes grown on Silicon," oral presentation, 10th International Symposium on Photonic and Electromagnetic Crystal Structures (PECS-X), Santa Fe, NM, USA (2012).
8. N. Descharmes, U. P. Dharanipathy, Z. Diao, and R. Houdré "Resonant optical trap in a photonic crystal cavity," oral presentation, ICTON 2012, Coventry, England (2012)
9. N. V. Triviño, G. Rossbach, U. Dharanipathy, J. Levrat, A. Castiglia, J. F. Carlin, K. A. Atlasov, R. Butte, R. Houdré, and N. Grandjean "High Quality Factor 2D GaN Photonic Crystal Cavity Membranes grown on Silicon," oral presentation, ICPS 2012, Zürich, Switzerland (2012).
10. N. Descharmes, U. P. Dharanipathy, Z. Diao, and R. Houdré "Microfluidic integrated hollow photonic crystal cavities for single particle and resonant field interaction," poster, CLEO: Applications and Technology 2012, San Jose, CA, USA (2012)
11. U. Dharanipathy, N. Vico Triviño, C. Yan, Z. Diao, J. Carlin, N. Grandjean, and R. Houdré "Fabrication and Near-IR Measurement of GaN Photonic Crystal Membranes: Wires, Waveguides and Cavities," poster, 10th International Symposium on Photonic and Electromagnetic Crystal Structures (PECS-X), Santa Fe, NM, USA (2012).
12. U. Dharanipathy, N. Vico Triviño, C. Yan, Z. Diao, J. Carlin, N. Grandjean, and R. Houdré "Dispersion and propagation properties of Photonic Crystal waveguide modes in Gallium Nitride membranes and suspended nano wires," poster, ICPS 2012, Zürich, Switzerland (2012).

13. N. Descharmes, U. Dharanipathy, Z. Diao, M. Tonin and R. Houdré “Back-action and self-trapping in a hollow 2D photonic crystal cavity,” poster, ICPS 2012, Zürich, Switzerland (2012).

Acknowledgements

So many people helped me in different way since I arrived Lausanne in May 2009. I want to thank them for providing me a nice life during my four years PhD study at EPFL. First of all, I want thank Prof. Romuald Houdré for accepting me as a PhD student in his group. He led me on the way towards my PhD thesis. I learned a lot from him, not only in scientific research but also in many other aspects of life. He constantly encouraged me to try different ideas. Whenever there is a need, he is always ready to give constructive suggestions to solve arising issues. He shared his positive attitude and amazing experience of life with me, which changed many of my opinions of this world.

I want to thank my friends and colleagues in our group. Dr. Hua Zhang transferred his outstanding processing techniques to me. Dr. Jana Jágorská explained some important basics of photonics to me in the first year of my work. Nicolas Descharmes and Ulagalandha Perumal Dharanipathy joined the group shortly after me. We made the challenging experiment possible by our unbeatable corporations. All the nice time I spent with them after work make our life not alone and help each other to overcome all kinds of tough time. I will remember the moment when I reached the top of Pic Chaussy with Nicolas for my first and only time Ski rando. I will also remember the interesting discussions with Peru about China and India. As the only native speaker, Peru also spent a lot of time with me to polish English of this thesis. I also want to thank our new group member Mario Tonin. He is a very good scientist and able to learn knowledge in different research field. I want to thank our former group member Prof. Nicolas Le Thomas for his help on my research project and PhD thesis.

I want to thank our colloberator on THz lasers project in Prof. Jérôme Faist's group at ETHZ. Many of nice ideas of THz lasers were inspired by Prof. Jérôme Faist. Dr. Giacomo Scalari shared his solid knowledge on QC lasers with me. Christopher Bonzon did all the characterizations of the lasers with outstanding performances, which speed up our project progress and upgrade our final results.

I want to thank all the technique support from Nicolas Leiser, Damien Trolliet and Yoan Trolliet in our LOEQ cleanroom. They are all very nice and helpful persons. I also want thank all the staff in CMi cleanroom.

I feel really happy to meet many Chinese friends in Lausanne. I want to thank Dr. Han Wu, Dr. Hongyan Bi, Dr. Chaobo Huang, Dr. Li Jin, Dr. Rui Du, Dr. Changru Ma, Liang Qiao, Hui yang, Yan Yan, Peiyu Ge, Linling Wu, Hui Chen, Chen Yu, Yu Lu, Zhen Huang, Chen Yan, Jianpin Cheng, Qiang Lan and many others I did not put their name here, for all the happy time we spent together in the last four years.

The last but not least, I want to thank my wife Na Liu, my parents, my brother's family, especially my two adorable nieces. I can always feel their love despite the few thousand kilometers distance between us. Their love makes me feel warm and strong to face everything between me and my goal in my life.

Zhaolu DIAO

24 Rue de la Maladiere 1022 Chavannes Renens, Switzerland

Tel : +41 78 676 4561, Email : zhaolu.diao@epfl.ch, zhaoludiao@hotmail.com

Male, born on 1979.09.19, married, Chinese

Strength:

Semiconductor (GaAs, GaN) and Si photonic device design and processing specialist
Experience of photonic device applications on sensing, trapping and Terahertz laser
Good communication skills and fluent English

Education:

2009-present	EPFL, Switzerland	Ph.D. in Photonics
2006-2009	University of Stuttgart, Germany	Master of Science in Physics
1997-2001	Jilin University, China	B. S. in Physics

Working experience:

2001-2006	Huatai Building & Decorative Materials, Urumchi, China
-----------	--

Research experience:

Ph.D. thesis **ICPS, EPFL 2009 - present**

Topic: Investigation of 2D photonic crystals and their applications on terahertz quantum cascade lasers, optical trapping and sensing

Master thesis in 4th Physics institute, Uni. Stuttgart 10.2007-12.2008

Topic: Design, fabrication, and characterization of metamaterial structures and their applications on bio-sensing

Technical abilities:

- Modeling with CST Microwave Studio, Matlab, Comsol
- E-gun evaporator, E-beam lithography, Photolithography, RIE and ICP dry etching, PECVD, PDMS microfluidic devices
- Characterization with AFM, SEM, FTIR spectrometer
- More than 4 years working experience in clean room

Awards:

- **EOS 2011 Best student oral presentation Springer Award (2011)**
- **Outstanding Self-Financed Students Scholarship in Xinjiang (2012)**

Languages:

Chinese	Native language
English	Fluent
German	A2
French	A2